Solar Multi-Conjugate Adaptive Optics

Thesis submitted for the degree of

Doctor of Philosophy (Technology)

Submitted by
Saraswathi Kalyani. S

Department of Applied Optics and Photonics
University of Calcutta

2024

Dedicated to the ones who stuck with me until the very end.

கற்றதுகைம் மண்ணளவு கல்லா துலகளவென்(று)
உற்ற கலைமடந்தை ஓதுகிறாள் – மெத்த
வெறும்பந்த யங்கூற வேண்டாம் புலவீர்
எறும்புந்தன் கையாலெண் சாண்.

ஔவையார் (சங்ககாலப் புலவர்)

Translation from Tamil:
What is known equals a handful of dirt, what is unknown equals the width of the world.
The goddess of learning herself keeps learning.
So, poets, don’t bet and talk big,
for the body of an ant, too, is eight spans.

Avvaiyar (Poet from the Sangam period)

(Translation adapted from GIVE, EAT, AND LIFE: POEMS OF AVVAIYAR by Thomas Hitoshi Pruiksma)

Abstract

Ground-based telescopes are severely limited in their performance by the turbulence of the Earth's atmosphere. The wavefronts emitted by the celestial bodies are perturbed and we lose high spatial frequency information. One solution to overcome the deleterious effects is to use adaptive optics (AO) systems to compensate for the distortions in the wavefront in real-time. They use a wavefront sensor to measure the perturbations of the wavefront and an adaptive optical element like a deformable mirror (DM) to compensate for the perturbations. The simplest AO systems are Single Conjugate AO (SCAO) systems; they offer an AO-corrected field of view of about 10 - 15 arc-seconds. This is due to the lack of correlation of the turbulence experienced by wavefronts arriving from different angles on the sky. The angular region over which the wavefronts arriving from different directions have a significant correlation is called the isoplanatic angle. When studying extended objects like the Sun, it would be beneficial if the AO-corrected field of view is larger than that offered by SCAO systems. This can be done by implementing a Multi-Conjugate AO (MCAO) system. MCAO systems use two or more DMs that are conjugated to distinct layers of the Earth's atmosphere and they can offer AO correction over 1 arc-minute fields. With plans for larger ground-based telescopes like the 2 m National Large Solar Telescope (NLST), it is essential that we develop the expertise in solar AO and related technology by developing and testing them on existing smaller telescopes.

One of the crucial parameters in the design of an MCAO system is the height of the strong layer of turbulence above the site to which the second DM will be conjugated. We need to study the vertical distribution of turbulence strength ($C_N^2(h)$) at the site to identify this layer. The first part of this thesis deals with $C_N^2(h)$ measurements in the daytime. We have used an optical method called S-DIMM+ (Solar-Differential Image Motion Monitor+) that uses the motion of images obtained with a 2-D array of lenslets to estimate the C_N^2 profile. We have performed extensive simulations to study the performance of this technique with our system parameters. Following this, we also carried out the experiment at the Kodaikanal Observatory to estimate the $C_N^2(h)$ up to $\sim$6 km. We identified the presence of a strong turbulence layer at about 3 km above the site. Near-simultaneously, we have used balloon-borne temperature sensors to measure the near-Earth turbulence up to a maximum of 350 m. The results agreed with earlier seeing-measurements at the observatory. These two experiments are the first daytime profiling campaigns at the Kodaiakanal Observatory's 125 year history.

The second part of this thesis deals with the measurement of the isoplanatic angle during the daytime. We used an iterative deconvolution method to estimate the isoplanatic angle from the long-exposure seeing-limited images taken with the 20 cm H-α telescope at Merak to be about $15'' - 20''$. The next part of the thesis details the first designs of SCAO and MCAO systems for KTT. Some preliminary work on the code for wavefront sensor has been completed and this is also

discussed.

Finally, in the last part of this thesis, we have developed simulations to quantify the performance of solar telescopes and associated AO systems. Traditional image quality metrics like Strehl ratio and encircled energy require knowledge of the point spread function (PSF). During the daytime, due to the extended nature of the Sun, we do not have access to the PSF. Therefore, we have performed extensive simulations in Python to quantify the performance of solar AO systems using rms granulation contrast as the metric. We obtain semi-logarithmic plots indicating the correspondence between the Strehl ratio and the rms granulation contrast for most practical values of the telescope diameters (D) and the atmospheric coherence diameters (r_0), for various levels of adaptive optics compensation. We estimate the efficiency of a few working solar adaptive optics systems by comparing the results of our simulations with the Strehl ratio and rms granulation contrast published by these systems. Our results can be used in conjunction with a plausible 50% system efficiency to predict the lower bound on the rms granulation contrast expected from ground-based solar telescopes.

List of Publications

Refereed journal articles

1. *Image Quality Specification for Solar Telescopes*
Saraswathi Kalyani Subramanian, Sridharan Rengaswamy, 2023, *Solar Physics* 298, 15. 10.1007/s11207-022-02105-2

2. *Daytime turbulence strength profile measurement at Kodaikanal Observatory*
Saraswathi Kalyani Subramanian, Sridharan Rengaswamy, Prasanna Gajanan Deshmukh, Binukumar G. Nair, S. Mahesh Babu, 2024, *Journal of Astronomical Telescopes and Instrumentation Systems*, 10 (3), 039004. 10.1117/1.JATIS.10.3.039004

Conference proceedings

1. *Forward modelling of turbulence strength profile estimation using S-DIMM+*
Saraswathi Kalyani Subramanian, Sridharan Rengaswamy, 2023, *Society of Photo-Optical Instrumentation Engineers (SPIE) Conference Series*, 12638. 10.1117/12.2671735
2. *Measurement of isoplanatic angle and turbulence strength profile from H-alpha images of the Sun*
Saraswathi Kalyani Subramanian, Sridharan Rengaswamy, 2023, *Adaptive Optics for Extremely Large Telescopes 7 (AO4ELT7)*, 22. 10.13009/AO4ELT7-2023-023
3. *Design of AO and MCAO system for the Kodaikanal Tower telescope*
Saraswathi Kalyani Subramanian, Sridharan Rengaswamy, 2024, *Proceedings Volume 13097, Adaptive Optics Systems IX*. 10.1117/12.3019679

List of presentations

Talks

1. *Measurement of day-time turbulence strength profile at Kodaikanal Solar Observatory* at Groupe recherche et development of the Laboratoire d'Astrophysique de Marseille, Marseille, France (June, 2023).

2. *Measurement of isoplanatic patch size using H-alpha images of the Sun* at Adaptive Optics for Extremely Large Telescopes 7 (AO4ELT7), Avignon, France (June, 2023).
3. *Measurement of turbulence strength profile at the Kodaikanal observatory* at Modern Engineering Trends in Astronomy, Raman Research Institute, Bangalore, India (November, 2023).
4. *Measurement of turbulence strength profile at the Kodaikanal observatory* at In-house meeting, Indian Institute of Astrophysics, Bangalore, India (March, 2024).

Posters

1. *Solar Multi Conjugate Adaptive Optics* at the 39th Meeting of the Astronomical Society of India (online, February, 2021).
2. *Forward modelling of turbulence strength profile estimation using S-DIMM+* at the Women in Optics and Photonics in India (WOPI), Raman Research Institute, Bangalore, India (December, 2022). Second prize, Best Poster Award
3. *Correlation of Zernike polynomial coefficients as a function of angle on the sky* at the 41st Meeting of the Astronomical Society of India, Indian Institute of Technology, Indore, India (March, 2023).
4. *Image Quality Specification for Solar Telescopes* at In-house meeting, Indian Institute of Astrophysics, Bangalore, India (April, 2023).
5. *Design of AO and MCAO systems for the Kodaiakanal Tower Telescope* at the SPIE Astronomical Telescopes + Instrumentation Systems 2024 conference, Yokohama, Japan (June 2024). Best Poster Award

Contents

List of Figures

List of Tables

Chapter 1

Introduction

> *"Some think that solar work is pretty well played out. In reality, it is only beginning."*
>
> *George Ellory Hale (from Explorer of the Universe: A Biography of George Ellory Hale)*

1.1 The Sun

Astronomy is often considered one of the oldest sciences. Our ancestors tracked the motions of stars and planets long before we turned our telescopes towards them. They made up stories of brave heroes immortalized in the heavens or of angry gods that punished the humans. In doing so, they started noticing patterns in the motions of these celestial bodies, giving birth to some of the earliest scientific theories. Perhaps, looking back, some of these theories are outrageous now. And some discoveries serendipitous. Nevertheless, as time progressed, our theories and technology both improved - bringing us closer to understanding the fundamentals of the universe.

The Sun, being our closest star and responsible for all life on Earth slowly became central in our theories. It was one of the first objects to be studied with a telescope, but was also studied with the naked eye for many centuries before that. In the following section we will see how it changed our understanding of the basic physical laws time and time again. We have summarized some of the most of the crucial discoveries related to solar science and a brief description of the evolution of our understanding of the Sun. This is by no means a comprehensive review of the history of our study of the Sun. Therefore, wherever possible, there are references to review articles or books which are better sources for a more extensive overview of the field.

1.1.1 History of solar studies

Considering the relative ease of observing them, it is perhaps not surprising that some of the earliest astronomical records related to eclipses. Needham (1959), mentions reports of an eclipse sometime between 2165 and 1948 BC. However, as noted in the book, there is confusion regarding the exact year and the authenticity of this eclipse. Therefore, the eclipse of 1223 BC at Ugarit (in modern day Syria) is often considered as the oldest one recorded (on a clay tablet) (de Jong and van Soldt, 1989). While it is interesting to study these historical records, one must keep in mind that these might not be very accurate. It appears that some observations were shifted in time to coincide with another event, or were purely made up to correspond to the dates of battles or to be used as literary devices (Newton, 1974). Therefore one must first ascertain the veracity of these records and express caution in using them for scientific study. An interesting history of eclipse records and their study can be found in Zirker (1995). There have also been reports of observations of sunspots as early as 800 BC[1]. They were described as dark features on the Sun. The earliest known drawing of sunspot is from 1128 AD (Stephenson and Willis, 1999).

The first attempt at measuring the distance between the the Sun and the Earth was carried out by Aristarchus (around 200 BC). He calculated the angular diameter of the Sun to be around 2° (Heath, 1913). We now know that this an over-estimate. Nevertheless it marks one of the earliest known instances of the scientific temper overtaking the creative mind. He was also the first to put forth a version of the heliocentric theory and proposed that the Earth orbits a fixed Sun. However, the theory gained more traction when Copernicus described the heliocentric model of the solar system in the 1543. The work was then extended by Kepler (in 1609) to give the planets elliptical orbits and paved the way for what we now know as Kepler's laws of planetary motion. A year later, almost five centuries after the first drawing of a sunspot, there were multiple near simultaneous observations of sunspots using telescopes for the first time by Thomas Harriot, Johannes Fabricius, Christoph Scheiner, and Galileo Galilei (Vaquero and Vázquez, 2009). There was a famous disagreement at the time between Scheiner and Galilei regarding the nature of these sunspots. Scheiner explained them as small planetary bodies orbiting the Sun whereas Galilei was of the notion that sunspots were on the solar surface. The pamphlet he wrote defending his stance was the beginning of a series of events that led to his arrest by the Roman Inquisition. Sunspots became important yet again when Hale (1908) observed them and showed the existence of magnetic fields outside of the Earth for the first time.

Perhaps Issac Newton's experiment (in 1665) in splitting sunlight into different colors can be considered the next significant breakthrough in solar physics after Galilei. The followup of this a century and half later by Herschel (1800) led to the first detection of infrared light. Humanity had discovered that the electromagnetic spectrum extended beyond the visible. Then, in 1801, Ritter discovered ultraviolet (UV) radiation at the opposite end of the visible spectrum. Wollaston (1802) also reported on his observations of the solar spectrum, independently discovering UV radiation. He also observed dark lines in the spectrum, which he attributed to the boundary of colors. Around

---

[1] Sunspot record

1814 - 1815, Fraunhofer (1817) paid closer attention to these lines and found around 600 of them! It wasn't until the 1850s when Bunsen and Kirchoff were then able to explain the origin of these lines as the absorption of light by gas. Much later, in 1925, Cecilia Payne became the first person to deduce the abundances of different elements and showed that Hydrogen was the most abundant element in the Sun and other stars (J.-L. Tassoul and M. Tassoul, 2004). This is the basis for spectroscopy; it is now applied to all astronomical objects to understand the chemical compositions of bodies that are millions of light-years away from us.

As there was better understanding of the orbit of the planets, the position of the Sun and, the composition of the Sun, two pressing questions remained. How old is the Sun and how does it produce energy? The two questions are tied intimately to one another. The solution must be able to answer the massive energy we receive from the Sun while also accounting for the large timescales over which the Sun has been producing this energy to account for the evolution of life on Earth. Both these questions baffled the scientists in the nineteenth-century. With the knowledge of thermodynamics, the Sun was assumed to be akin to a heat engine; once it ran out of fuel, it would cease to radiate energy. Some of the earliest theories in the mid-1800s suggested that falling meteors (kinetic energy) generated thermal energy (Thomson, 1854; Waterston, 1860; Mayer, 1863). However, it was found that the energy generated by this method was insufficient to explain the measured radiation from the Sun. Around 1860, the Helmholtz-Thomson theory which suggested gravitational contraction as the mechanism of energy generation gained popularity (Clerke, 1893). However, one of the drawbacks of this theory was the supposed reduction in the Sun's diameter which was not observable. Furthermore, the age estimated by this theory did not provide sufficient time for the evolution of life on Earth. There were few other theories regarding energy generation in the Sun which can be found in Kragh (2016). A major breakthrough occurred when Henri Becquerel in 1896 discovered radioactivity (Romer, 1964)[2]. Following Aston (1920), which showed that the helium nucleus was lighter than four hydrogen nuclei, Perrin (1919) and Eddington (1920) independently showed that by burning hydrogen to form helium, sufficient energy would be released to explain the rate of radiation from the Sun. Bethe and Critchfield (1938) analyzed the different processes with which hydrogen can fuse to form helium. We now know that for low mass stars (like the Sun), the *p-p chain* (proton-proton chain) is responsible for the fusion of hydrogen atoms. In more massive stars, it is the *CNO cycle* (Carbon-Nitrogen-Oxygen cycle) which was originally proposed by Weizsäcker (2014)[2].

We know that the *p-p chain* releases electron neutrinos (other types being muon and tau neutrinos). Studying the neutrinos on Earth is one way to directly study the inner layers of the Sun. One of the first detectors built to study solar neutrinos called the Homestake experiment detected fewer neutrinos than the theoretical prediction (given by solar models based on the luminosity of the Sun). This was called the "solar neutrino problem". In 1988, the Kamiokande experiment further confirmed it. In 1996, the upgraded Super-Kamiokande experiment began observations. Along with the 2001 SNO (Sudbury Neutrino Observatory) experiments, it showed that the neutrinos oscillate and change flavors (to muon and tau neutrinos) when travelling from the Sun (Nakahata,

---

[2] Please note that the citation to the translated English version is given here.

2022); it altered our fundamental understanding of neutrinos.[3]

Therefore, over the last few centuries, our knowledge of the Sun has improved tremendously. Within an astronomical context, the Sun acts as a template using which we model and attempt to understand the behavior of other stars. That is why it is often considered the Rosetta stone of astronomy. But, we have also seen that the Sun is a unique laboratory with extreme conditions that cannot be (or are very difficult to) replicate on Earth. These have helped us gain a better understanding of the fundamental laws of the universe. Furthermore, the close proximity means that it is essential we understand the impact that it can have on life on Earth. Consequently there is no doubt about the need to study and understand the Sun in even greater detail!

1.1.2 Current understanding of the Sun

We now know that the Sun is a G2-type star at about 150 million km from the Earth (also known as 1 AU - Astronomical Unit). The mass of the Sun (often denoted by $m_{\odot}$) is about 2×10^{30} kg. The photospheric diameter of the Sun is about 1.4 million km and the angular diameter when viewed from the Earth is about 0.5° (or $32''$) (Stix, 2002). It can be described as being made of layers. The layers are grouped into two categories - the solar interior and the solar atmosphere.

The Interior

The interior is made up of four regions - the core, the radiative zone, the interface layer (or tachocline) and the convection zone. The region where energy is generated is called the core. Here, a nuclear fusion reaction converts the hydrogen to helium (*p-p chain*). The temperature in the core is about 15 million°C with a density of about 150 g/cm^3. The photons generated in the core then travel through the radiative zone bouncing from one particle to another taking each photon almost a million years to reach the tachocline. The density and temperature closer to the core are about 20 g/cm^3 and $7\times10^6\,^{\circ}C$, respectively. They drop to 0.2 g/cm^3 and $2\times10^6\,^{\circ}C$ near the tachocline. It is thought that the magnetic field of the Sun is generated in the interface layer. At the convection zone, as the name suggests the energy transportation is through convection.

The Atmosphere

The solar atmosphere is comprised of the photosphere, the chromosphere, the transition region and the corona. The photosphere is the visible region of the Sun. Within the photosphere, the temperature initially decreases from around 6600 K at the bottom to about 4400 K at about 500 km.

---

[3] Some interesting articles can be found in the links:

- How the Sun shines
- Solving the mystery of the missing neutrinos

The features on this layer include sunspots, faculae and granules. Sunspots are dark regions on the surface of the Sun with strong magnetic fields (around 1000 - 4000 G) and which are cooler (around 3700 K) than the surrounding regions (see Figure 8.30 of Stix (2002)). They have life spans of the few days but large sunspots can last for weeks. Each sunspot typically has two parts - the inner region which is darker is called the umbra and the outer region which is lighter is called the penumbra. This can be seen in Figure 1.1 (c). The dark (almost black) region is the umbra and the lighter region surrounding it with tube-like features is the penumbra[4]. Sunspots often occur in pairs of opposite polarity[5]. The number of sunspots is often used as a measure of solar activity (with each cycle typically lasting about 11 years). If one plots the number of sunspots as a function of the latitude on the Sun at which they appear, one gets a butterfly diagram[6]. At the start of a cycle, the spots tend to appear at higher latitudes and with the progression of the cycle, more spots appear closer to the equator. Faculae[7] are small (around 100 km on the Sun) bright regions; they are more easily observed close to the limb than the disk center. They are also regions of magnetic flux concentrations (Berger et al., 2007). The number of faculae is also proportional to solar activity. An interesting point is that the solar irradiance was found to be higher during solar maxima (Fröhlich, 2002). This might be counter intuitive as the number of sunspots (darker regions) also increases with solar activity. Granules are cell-like structures that are present on the surface of the Sun independent of solar activity. They can be seen at the top of Figure 1.1 (c). They are the tops of convection cells where the hot plasma rises up (bright regions) and then cools and sinks downwards (darker regions). The dark interconnected regions are called intergranular lanes. Granulation are present over the entire solar disk except in the places with sunspots. The cell size of granules defined as the distances between the centers of two adjacent granules has a mean of about $1.9''$. The mean lifetime of individual granules is between 6 to 12 minutes (with the variation in mean lifetimes due to the criteria for the birth or death of granules) (Stix, 2002).

The next layer in solar atmosphere is the chromosphere[8], where the temperature increases to about 10000 k. When observed during eclipses, the chromosphere appears reddish due to the emission of light (at H-α) by hydrogen at higher temperatures. The chromospheric features include the chromospheric network, filaments, plages, prominences and spicules. Plages, best observed at H-α, are bright regions that coincide with active regions. They have weaker magnetic fields ($\leq$10 G). Filaments are dark features (appearing thread-like) which are arcs of plasma held by magnetic fields. Prominences are the same as filaments except they are observed at the limb of the Sun and appear as bright structures (against a dark interstellar background). The difference between filaments and prominences can be seen in Figure 1.1 (e))[9]. They protrude out into the

---

[4] Image source for Figure 1.1 (c)

[5] Hale's Sunspot Polarity Law

[6] The Butterfly Diagram

[7] Facula is the singular form and is the Latin word for "small torch".

[8] The word chromosphere derives from the Greek word *chroma* meaning color as the chromosphere appears red when observed during an eclipse.

[9] Image source for Figure 1.1 (e)

corona but are anchored to the solar surface and have much higher densities (Stix, 2002). They can last over few days to few months. A review of prominence studies can be found in S. Parenti (2014).

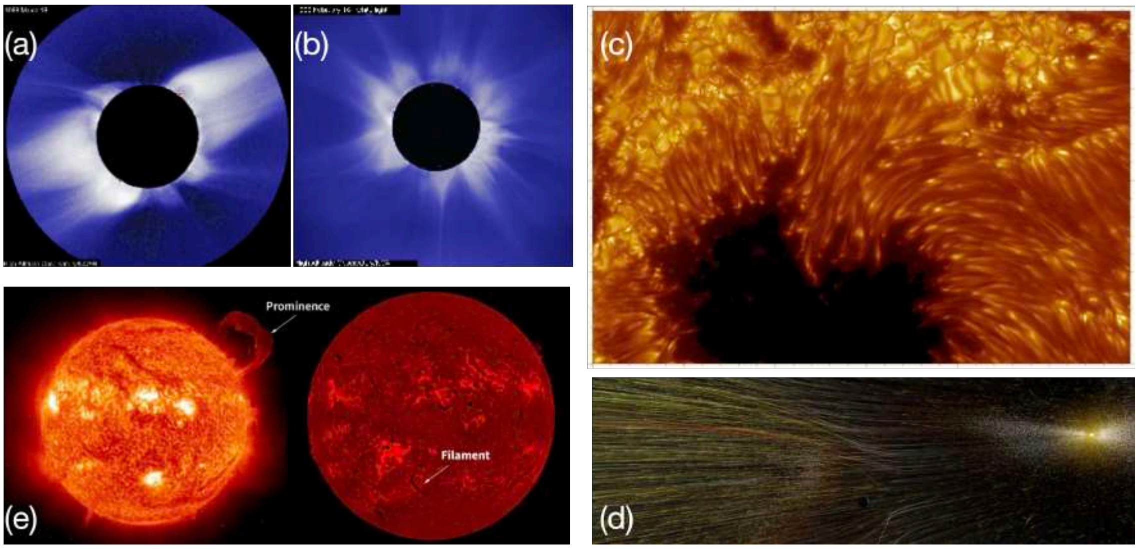

Figure 1.1: Images of different solar features or layers. (a) and (b) are images of the solar corona taken during an eclipse during solar minimum and maximum, respectively. (c) Image of a sunspot and solar granulation. (d) An artist's impression of solar wind. (e) Image showing solar prominence and filament. The sources for the different images are given within the text.

After the chromosphere, there is a sudden increase in temperature to almost a 1 million k in the corona. This region in between is called the transition region which is highly inhomogeneous in nature. The UV regime from 50 nm to about 160 nm is typically used to study this region. Instruments like SUMER (Solar Ultraviolet Measurements of Emitted Radiation) onboard SOHO (Solar and Heliospheric Observatory) or the TRACE (Transitional Region and Coronal Explorer) and IRIS (Interface Region Imaging Spectrograph) missions have been used to study the transition region. Finally, we have the corona[10], the outermost layer of the Sun. During eclipses, when the disk light is obstructed, the corona can be studied in white light. This is shown in Figure 1.1 (a) and (b)[11], taken at solar minimum and maximum, respectively. From this, one can see the effect of solar activity on the corona. Since we cannot always wait for an eclipse to study the corona, coronagraphs can be used to create artificial eclipses and observe at white light. The corona also emits radiation at radio wavelengths. At different heights from the solar surface, the electron density is different. Each electron density corresponds to a critical frequency below which radio

---

[10] Corona is Latin for "crown".

[11] Image source for Figure 1.1 (a) and (b)

waves cannot propagate. Therefore, by studying the Sun at different radio frequencies, we can probe different heights in the solar atmosphere. The flux at 10.7 cm is used as a measure of solar activity (Stix, 2002). The corona is also studied in X-rays. Coronal features include bushels, helmet streamers, polar plumes, coronal loops, coronal holes and various types of radio bursts (Krüger, 1979). Due to the high temperatures in the corona, the charged particles are excited to very high speeds (>400 km/s) that can escape the gravity of the Sun. This causes solar winds, which are responsible for the tails of comets. The Earth's magnetic field repels most of the particles in the solar wind. An artist's illustration of the solar wind is shown in Figure 1.1 (d)[12]. In extreme cases when the particles enter the Earth's atmosphere, they cause auroras.

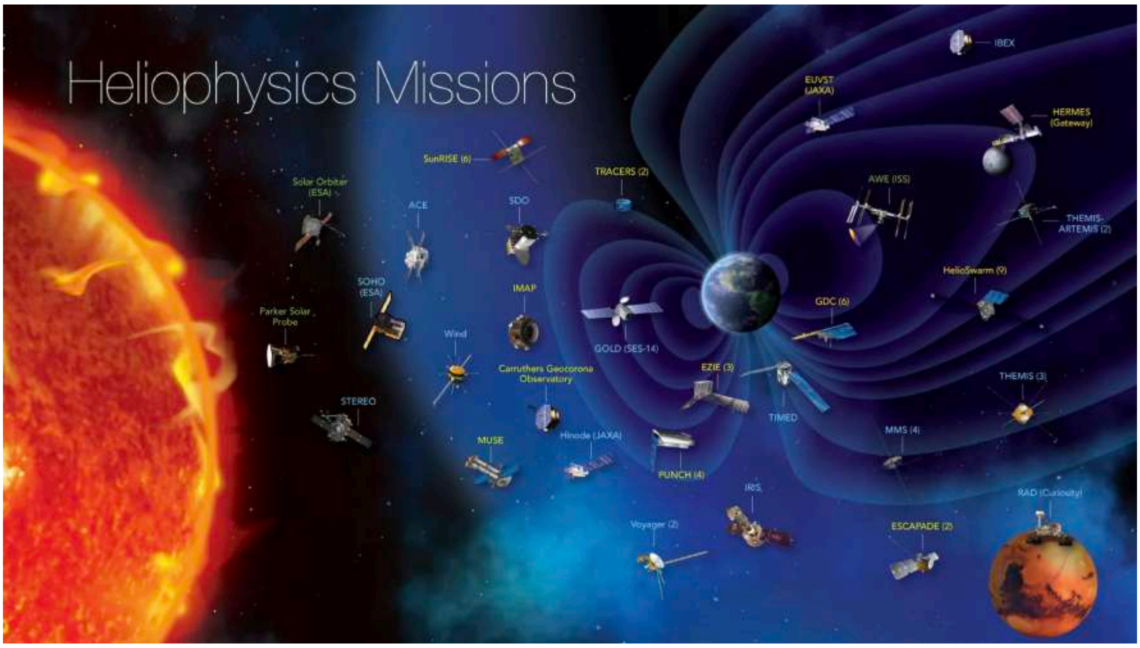

Figure 1.2: Graphic showing various space-based missions that have been used to study the Sun. Image credit: NASA. NOTE: This graphic is incomplete. For example, Aditya-L1 is not shown here.

1.1.3 Future of solar studies

As we saw, the Sun is a highly dynamical body with activity happening over a range of spatial and temporal scales. Despite studying it for over 4 centuries with telescopes, we still have many questions about it. Therefore, it is necessary to have a variety of different instruments that allow us to study it at different spatial and temporal scales over different wavelengths so that we can gain

---

[12] Image source for Figure 1.1 (d)

a holistic understanding. With this motivation, particularly over the last few decades, there have been a host of ground-based and space missions dedicated to observing the Sun. Some of the space missions that have been used to study the Sun are shown in Figure 1.2. The Parker Solar Probe, launched by NASA (National Aeronautics and Space Administration) in 2018, became the first man-made object to “touch the Sun” when it passed through the solar corona. India also launched its first dedicated space-based solar observatory, Aditya-L1 with a suite of instruments to study the Sun (Tripathi et al. (2023) and references therein) in September 2023.

On the ground as well, there are many new solar telescopes being built. For example, China currently has the largest array of radio telescopes dedicated for solar observations called the Daocheng Solar Radio Telescope (DSRT, Yan et al. (2022)). Then, there are large optical telescopes like DKIST (Daniel K. Inouye Solar Telescope, T. R. Rimmele, Warner, et al. (2020)) or the upcoming EST (European Solar Telescope, Quintero Noda et al. (2022)). Based on the current plans, EST is likely to be the first solar telescope to have an adaptive secondary mirror (ASM). Both DKIST and EST are 4 m telescopes which will have a diffraction-limited resolution of $0.025''$ at 500 nm. This corresponds to resolving features down to 18 km on the Sun’s surface! However, as we will see in the next section, things are not so ideal in ground-based optical observations.

1.2 Earth’s atmospheric turbulence

We construct larger telescopes for two primary reasons - better sensitivity (detect fainter objects) and better resolution (separate two objects that have smaller angular separations). Ideally, we expect the diffraction-limited resolution of a telescope (having a circular aperture of diameter ‘D’) to be of the order of λ/D, where λ is the wavelength of observation. For a circular aperture, the image of a point source, under diffraction-limited conditions is given by the Airy pattern. This is also called the point spread function (PSF). The fourier transform of the PSF is the optical transfer function (OTF); it gives the response of the system as a function of spatial frequencies. Under diffraction-limited conditions, the OTF of a circular pupil is given by:

$$\mathrm{T}(q) = \frac{2}{\pi}\left[cos^{-1}(q) - q\sqrt{1-q^2}\right], \tag{1.1}$$

where q is the normalised spatial frequency.

In reality, the Earth’s atmosphere is in-between any celestial object we want to observe and a ground-based telescope. We know that the Earth’s surface temperature increases and decreases due to the variation in heating by the Sun. This causes heating and cooling of the air and injects energy into the atmosphere causing motions at large scales. The kinetic energy of motions at large scales is transferred by being broken down into motions at smaller and smaller scales; at the smallest scales, this kinetic energy is dissipated as heat due to viscous friction. This is the principle of Kolmogorov’s theory of atmospheric turbulence (Kolmogorov, 1941). The largest scale at which the motions give rise to turbulence is called the outer scale (L_0) and the smallest scale at which the viscous dissipation starts is called the inner scale (l_0). The range of spatial frequencies within $1/L_0$ and $1/l_0$ is called the inertial range. Due to the turbulent motion, there are randomly distributed pockets of air called "eddies" of different sizes, each having its own characteristic temperature. The relative contribution of eddies at different sizes to the total wavefront distortions is given by the power spectral density of the refractive index ($\Phi_N(\mathbf{k})$). Here N denotes refractive index and $\mathbf{k}$ is the three-dimensional wave vector with the components (k_x, k_y, k_z). From the Kolmogorov law, within the inertial range (F. Roddier, 1981),

$$\Phi_N(\mathbf{k}) = 0.033 C_N^2 k^{-11/3}, \tag{1.2}$$

where, C_N^2 is the refractive index structure constant. It is a measure of the vertical distribution of the strength of atmospheric turbulence and has units of $\mathrm{m}^{-2/3}$. It is related to the refractive index structure function (D_N), which is the squared difference in the refractive index fluctuations between two points separated by a distance 'r', as (F. Roddier, 1981):

$$D_N(r) = C_N^2 r^{2/3}. \tag{1.3}$$

By integrating the total strength of the turbulence over all the heights in the atmosphere, we arrive at a single value called the *Fried's parameter* or r_0. It is given by (F. Roddier, 1981):

$$r_0 = \left[0.423 \left(\frac{2\pi}{\lambda} \right)^2 sec\zeta \int C_N^2(h) dh \right]^{-3/5}, \tag{1.4}$$

where ζ is the zenith angle and λ is the wavelength of observation. r_0 is typically of the order of few cms and from Equation 1.4, we can see that it has a larger value at longer wavelengths. So, what is the physical meaning of this parameter?

Consider the wavefront (surface of constant phase) arriving from a celestial object which is infinitely far away. We sample a very minuscule portion of the full wavefront which can assumed to be planar (just outside the Earth's atmosphere). We also know that turbulence in the atmosphere arises due to random temperature fluctuations, which give rise to random fluctuations of the refractive indices. Therefore, as the wavefront passes through the Earth's atmosphere, it is perturbed by the random path length fluctuations that it encounters. One of the effects occurs at large spatial scales and it introduces a slope to the wavefront (called the global tilt). This causes a shift of the image position on the detector plane. As the turbulent eddy is moved by the wind, the slope varies randomly. In a series of short-exposure images this manifests as a random variation of the image position (also known as *image motion*). This is superimposed by smaller-sized corrugations on the wavefront which lead to a loss of high-spatial frequency information about the source. Apart from this, there are also fluctuations in the amplitude of the wavefront. In a series of short-exposure images this manifests as a variation in brightness of the object; it is called scintillation (or is colloquially known as twinkling). When a long-exposure image of a point source is recorded, we see an approximately Gaussian function with a full-width at half-maximum corresponding to λ/r_0

(which is called “seeing” and has units of arc-seconds). This implies that the expected diffraction-limited resolution of $\propto \lambda/D$ has reduced to λ/r_0 (assumption being that D $> r_0$ as is the case in telescopes used for scientific study). This means that independent of the size of the telescope we use, our resolution is always limited by the atmospheric seeing.

The Fried’s parameter can also be described as the diameter of the circular region over which the rms phase variance is less than 1 radian. This can be understood as the region over which the perturbations introduced by the atmosphere are minimal and the wavefront is almost flat (or planar). It is related to the mean-squared phase variance between two points, $(\phi_1 - \phi_2)^2$, that are separated by the distance d as:

$$\langle(\phi_1 - \phi_2)^2\rangle = 6.88 \left(\frac{d}{r_0}\right)^{5/3} \text{radians}^2. \tag{1.5}$$

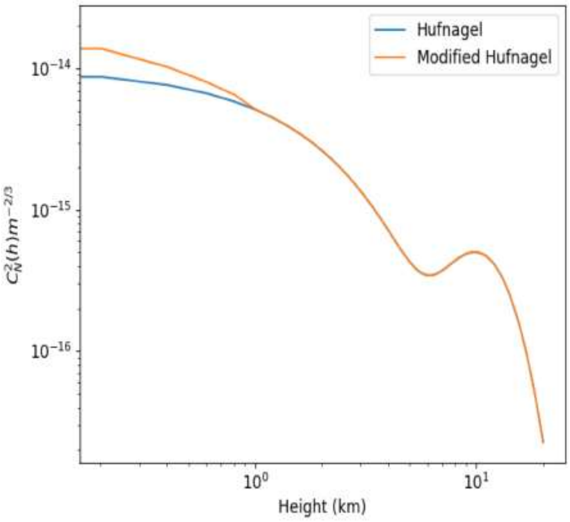

Figure 1.3: A plot of the Hufnagel model for C_N^2 is the blue profile (Equation 1.6). When the strong turbulence during the daytime is accounted, it is given by the orange curve (Equation 1.7).

The Fried’s parameter is one of the most commonly used metrics to describe the turbulence characteristics at a site. There are different techniques of measuring it (Fried, 1975; Sarazin and F. Roddier, 1990; Liu and Beckers, 2001; Rengaswamy, Ravindra, and Prabhu, 2019). However, in many cases, it is also beneficial to know the distribution of turbulence strength profile at the site. Once we know the C_N^2 profile, it can be integrated to estimate the r_0. Some of the techniques, specific to the daytime, that are used to measure the C_N^2 profile are discussed in Section 2.1. There have also been theoretical models that attempt to describe the typical profiles at sites. One of them given by Hufnagel (1974) is:

$$C_{N_H}^2(h) = A\left[2.2\times10^{-23}\left(\frac{z+h}{1000}\right)^{10} exp\left(\frac{-z+h}{1000}\right)\left(\frac{V_w}{\overline{V_w}}\right)^2 + 10^{-16} exp\left(\frac{-z+h}{1500}\right)\right], \tag{1.6}$$

where 'A' is a scaling constant, 'h' is the height above the ground in m, 'z' is the elevation of the site in m, and $\frac{V_w}{\overline{V_w}}$ is the ratio of upper to mean atmospheric wind speeds. An additional term must be added to account for strong daytime turbulence, and the total profile is given by Hill, R. Radick, and Collados (2004) as:

$$C_N^2(h) = C_{N_H}^2(h) + A_B exp\left(\frac{-h}{h_0}\right), \tag{1.7}$$

where A_B is the boundary amplitude and h_0 is the boundary scale height. Sample profiles generated using the Equations 1.6 and 1.7 are shown in Figure 1.3.

1.2.1 Isoplanatic Angle

Another parameter that is used to characterise the turbulence is the isoplanatic angle. It is the angular size of the sky region (alternatively, the angular size at the image plane) over which the point-spread function is invariant. In terms of the perturbed wave-fronts, it can be defined as the angular separation over which there is a significant correlation between the wave-fronts arriving at the telescope's pupil from two different directions. Quantitatively, it is be defined as the angular separation over which the difference between the root mean square wave-font errors of the wave-fronts traversing in those directions is equal to a radian. Therefore, the perturbations experienced by two wavefronts that are separated by an angle greater than θ_0 will not be significantly correlated. It is related to the Fried's parameter by the equation:

$$\theta_0 \propto \frac{r_0}{h_{\text{avg}}}, \tag{1.8}$$

where h_{avg} is the height of the strongest turbulence layer. The concept of isoplanatic angle is important when we think of the turbulence experienced by wavefronts traversing different volumes of the atmosphere before reaching the telescope pupil.

Now that we know the some important parameters of the atmospheric turbulence, let us look at the effect it has on our imaging. Equation 1.1 gives the ideal system response that we desire. However, in the presence of turbulence, the long-exposure seeing-limited transfer function is given by (Fried, 1966; F. Roddier, 1981):

$$\mathrm{S}(q) = \mathrm{T}(q) \times exp\left(-3.44\,(\alpha q)^{5/3}\right), \tag{1.9}$$

where α is the ratio D/r_0 (D is the telescope diameter and r_0 is Fried's parameter used to specify the strength of atmospheric turbulence).

One of the parameters used for characterising the performance of any optical system is the Strehl ratio. It is the ratio of the on-axis intensity of an aberrated PSF (aberrations due to optics or atmosphere) to the on-axis intensity of a diffraction-limited PSF. It has a maximum value of unity and a high value implies better performance of the system. The atmospheric perturbations can also be modelled like optical aberrations.

Zernike Polynomials

Zernike polynomials are a set of orthogonal polynomials that are defined over a unit circle (Noll, 1976; Lakshminarayanan and Fleck, 2011). They are used to quantify the aberrations in an optical system. Equivalently, the atmospheric turbulence can also be expressed in terms of the Zernike polynomial. Let the phase perturbations be $\phi(r,\theta)$; they can be expanded into a sum of polynomials as:

$$\phi(r,\theta) = \sum_{n,m} a_n^m Z_n^m(r,\theta), \tag{1.10}$$

where a_n^m are the coefficients (or amplitudes) and $Z_n^m(r,\theta)$ are the polynomials. Here r and θ are the variables for polar coordinates, n is the radial order of the polynomial and, m is the angular frequency. The Zernike polynomials ($Z_n^m(r,\theta)$) are given by:

$$\begin{aligned} Z_n^m(r,\theta) &= R_n^m(r) cosm\theta, \text{ for m} \geq 0, \\ Z_n^{-m}(r,\theta) &= R_n^m(r) sinm\theta, \text{ for m} < 0. \end{aligned} \tag{1.11}$$

m **n**	**0**	**1**	**2**	**3**	**4**	**5**	**6**
0	Z_1						
1		Z_2 Z_3					
2	Z_4		Z_5 Z_6				
3		Z_7 Z_8		Z_9 Z_{10}			
4	Z_{11}		Z_{12} Z_{13}		Z_{14} Z_{15}		

Table 1.1: Relationship between single and double indexing of Zernike Polynomials.

The radial function is given by:

$$R_n^m(r) = \sum_{l=0}^{(n-m)/2} \frac{(-1)^l (n-l)!}{l! [\frac{1}{2}(n+m)-l]! [\frac{1}{2}(n-m)-l]!} r^{n-2l} \tag{1.12}$$

Another notation for the Zernike polynomials uses a single subscript (say, j) instead of n and m, i.e,:

$$Z_j(r,\theta) = Z_n^m(r,\theta), \tag{1.13}$$

where $j = [n(n+2)+m]/2$. To convert from single to double indexed form, one can use the relations[13] $n = ceil([(-3+(9+8j)^{1/2})/2])$ and $m = 2j - n(n+2)$. The two notations are shown in tabular form in Table 1.1.

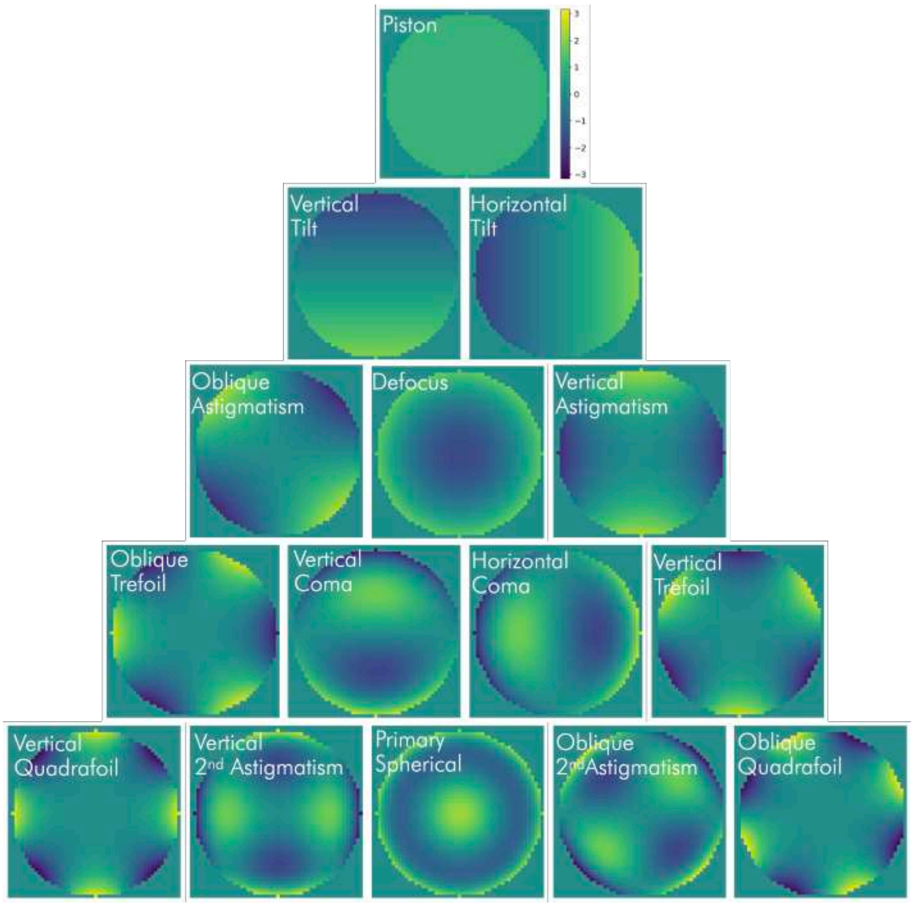

Figure 1.4: First 15 zernike polynomials. All images have the same color bar.

The first 15 zernike polynomials are generated and shown in Figure 1.4. Each row corresponds to one radial order of polynomials (order increasing by 1 in each row from top to bottom). Within each row, the polynomials corresponding to all the angular frequencies within that order are shown.

---

[13] The *ceil* term in the expression for n is the equivalent of the Python function math.ceil which is used to round up a number. (https://docs.python.org/3/library/math.html).

The colour bar is shown only in the first row but is the same for all the polynomials. As we have seen the turbulence introduced by the atmosphere can be compensated using AO systems. If perturbations up to N_Z terms of the zernike polynomials are perfectly compensated then the mean squared residual errors are given by:

$$\Delta_J \simeq 0.2944 J^{-\sqrt{3}/2} (D/r_0)^{5/3}, \tag{1.14}$$

where $J > 10$. The expressions for when correction is done for less than 10 terms can be found in Fried (1965) and Noll (1976).

Advantages of Zernike polynomials include:

- The polynomials are orthogonal. The coefficients of the different modes are independent of each other.
- The magnitude of the coefficient of a mode is proportional to the contribution of that mode to the total wavefront error.
- The coefficient of each mode is the RMS wavefront error due to that mode.

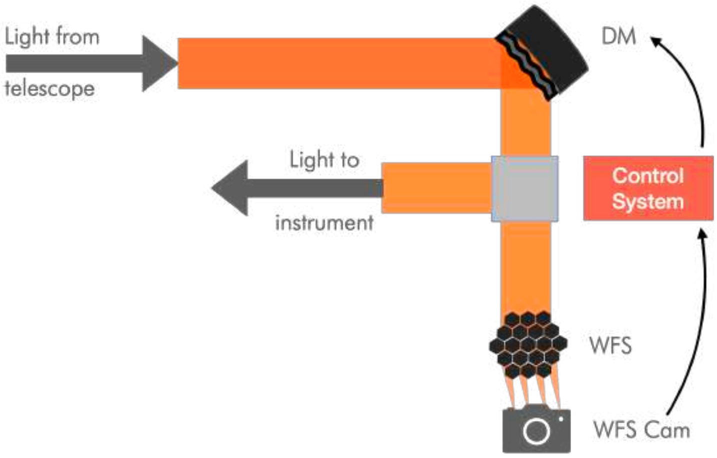

Figure 1.5: Schematic of a Single Conjugate AO (SCAO) system (not to scale).

Perhaps the easiest way to mitigate the deleterious effects of the Earth's atmospheric turbulence and have access to information from the entire electromagnetic spectrum is space-based telescopes. However, they are very expensive to construct, impose constraints on the system size due to the launching mechanisms and are difficult to upgrade. Therefore, there are advantages to correcting the turbulence effects on the ground.

1.3 Adaptive Optics

One way to overcome the deleterious effects of the Earth's atmosphere is to use an adaptive optics (AO) system to compensate for the wavefront perturbations in real-time. The idea was first put forth by Babcock (1953). He proposed that if the perturbations of the wavefront can be measured and fed back to an optical element that can change its shape based on the feedback information, it will be possible to correct for atmospheric seeing and instrumental aberrations. This is the working principle of the simplest AO system, called a Single Conjugate AO (SCAO) system. SCAO systems have three principal components as shown in Figure 1.5. They are – a wavefront sensor (WFS) to measure the phase distortions, an active optical element like a deformable mirror (DM) that can change its shape to correct the wavefront perturbations, and a control system that acts as an interface between the two. In a SCAO system, the WFS and the DM are both conjugated to the telescope pupil plane.

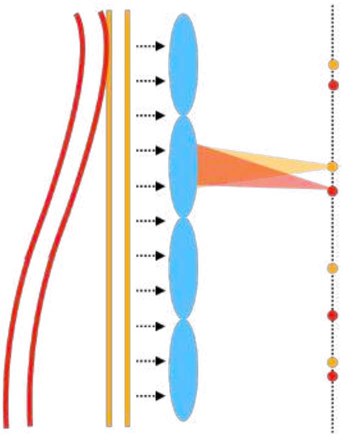

Figure 1.6: Diagram showing the principle of operation of SHWFS. The yellow and red curves are representative of planar and perturbed wavefronts, respectively. The direction of propagation of the wavefronts is shown using small black arrows. The blue ovals are 4 lenslets along one direction. The vertical dotted black line is the focal plane of the linear lenslet array. The yellow and red dots represent the positions where the images of each lenslet are formed (for a point source).

One of the commonly used WFS is the a SHWFS (Shack-Hartmann WFS). It is a two dimensional array (N×N) of lenslets. When a plane wavefront is incident on a SHWFS, it produces N×N PSFs. Ideally, the centers of each PSF are aligned with the optical axis passing through the centers of the corresponding lenslets. This is shown in Figure 1.6 by the yellow dots on the focal plane (shown as a dotted black line) of the lenslet array. It must be noted that for the sake of simplicity, Figure 1.6 is shown as a 1-D example. In reality, the wavefront is perturbed due to the turbulence (red curves) and the PSFs are shifted by an amount corresponding to the local tilt of the wavefront above each lenslet. The shifted positions of the centers are marked by the red circles. As a function of time, the image motion of each PSF varies randomly meaning the shifts vary with time. When a SHWFS is used in a solar telescope, each lenslet produces an image. Ideally the images are identical. However, they suffer a random motion as a function of time due to the effect of the turbulence. Therefore, by measuring the image motion at the focal plane of a SHWFS, we can estimate the local slope of the wavefronts.

The other important component of AO systems is the DM. There are different technologies in realising a DM. The surface can be either segmented or continuous. Then, actuators behind the mirror surface can be used to change the shape in the desired way. This can again be done using different techniques - voice-coil actuators, piezo-electric actuators etc. Two important properties of the actuators are pitch and stroke. The pitch is defined as the center-to-center distance between two adjacent actuators. This determines the level of AO correction that is possible. With a larger number of actuators we have the ability to correct for perturbations at finer spacial scales (equivalently at higher spatial frequencies). One of the main challenges of the future large telescopes is the requirement of large sized DMs (re-imaged pupil is large) with high actuator densities that can perform the desired levels of AO correction. The stroke determines the amount of the turbulence that can be compensated. The lowest order terms of tip and tilt (global slope of the wavefront) have the highest energies. To reduce the strain on the DM, practical AO systems correct for the tip-tilt separately; the DM only corrects for higher-order terms.

1.3.1 Image motion compensation

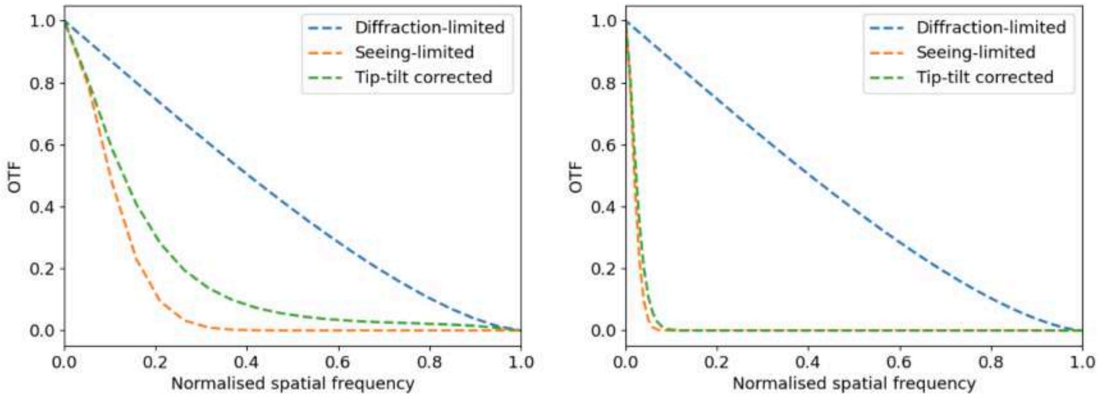

Figure 1.7: Plots of diffraction-limited (blue), seeing-limited (orange) and tip-tilt corrected (green) OTFs as a function of normalized spatial frequency. Left plots are for a 38 cm telescope with 10 cm r_0 at 430.5 nm. Right plots are for a 200 cm telescope (same atmospheric condition).

The correction for image motion alone is called image motion stabilization or tip-tilt correction. It is considered by some to be the simplest form of AO systems. In Section 1.2, we saw the equations for the diffraction-limited (Equation 1.1) and seeing-limited (Equation 1.9) transfer functions. A similar analytical model of the tip-tilt corrected transfer function is given by (Fried, 1966; F. Roddier, 1981):

$$\mathrm{S}_1(q) = \mathrm{T}(q) \times exp\left[-3.44\,(\alpha q)^{5/3}\left(1-q^{1/3}\right)\right]. \tag{1.15}$$

Figure 1.7 is a plot of the OTFs as a function of normalized spatial frequency for a 38 cm (left) and 200 cm (right) telescope. We can see that even under ideal diffraction-limited conditions (blue curves), the contrast decreases as a function of spatial frequency. This is due to the finite size of the telescope aperture. Under seeing-limited imaging (orange curves) we see a drastic fall in contrast compared to the diffraction-limited case. This shows the deleterious effects of the atmosphere on our science images. By compensating for the image motion, the contrast can be improved marginally as shown in the green curves. We can also see that with image stabilization the performance is better improved for smaller telescopes (left plot). For larger telescopes, the increase in performance is marginal. While tip-tilt correction as a standalone system can offer improved performance compared to seeing-limited imaging, it is not always sufficient. Therefore, a SCAO system with a DM is required to correct for aberrations at higher spatial frequencies.

1.3.2 Errors in AO

AO systems can never perform a “perfect correction” to the aberrated wavefront. There will always be some residual perturbations that are uncorrected. The main contributors are:

- Fitting error - This arises due to the uncorrected high spatial frequency terms in the residual wavefront caused by the finite number of actuators on the DM.

- Reconstruction error - This is made of all the sources that can reduce the accuracy of reconstruction (like aliasing, sampling error, noise, etc...).

- Temporal bandwidth error - This is due to the finite time for computing the command signals to the DM.

We now know the general operation principle of a SCAO system. Let us now look at the evolution of stellar AO systems. A few things must be kept in mind. First, we start with the history of stellar AO systems. Solar AO systems are discussed separately in Section 1.4 (to emphasize their importance within the context of this thesis). Furthermore, this is not a complete review of the evolution of all AO technology and systems in an astronomical context as that is beyond the scope of this thesis. It is a general overview of the progression of AO systems with technology and the birth of new techniques based on science drivers.

1.3.3 A brief history of the evolution of stellar AO

Following Babcock's suggestion, there were attempts both by the astronomical community and the US military in realising adaptive optics. In line with this thesis, we will focus only on the history of AO for astronomical applications. The first AO system for astronomical application that had a successful demonstration was the COME-ON (CGE Observatoire de Meudon ESO-ONERA) system at the 1.52 m telescope at the Observatoire de Haute-Provence (Merkle et al., 1989). Table 1 of Beckers (1993a) provides a list of AO efforts made at that time. Since those early days, the field of AO has advanced tremendously. One of the main limitations of SCAO systems is the requirement of a sufficiently bright source for the wavefront sensor. Foy and Labeyrie (1985) (and references therein) suggested that the limiting magnitude of a guide star for AO was between 10 - 13 magnitude. The scientific object under study may not have this required brightness. The alternative is to use another object which has the desired brightness (called guide star[14]). However, the guide star must also be located within one isoplanatic patch of the science object as the turbulence experienced by wavefronts from different angles on the sky will be different. If one uses only natural guide stars (NGS), then the areas on the sky over which AO correction can be done (called sky coverage) are limited. An early concept to overcome this was suggested by Linnik (1957). The idea was to use beacons. Today, most observatories create an artificial star also known as laser guide star (LGS). The LGS technique is often attributed to Foy and Labeyrie (1985). They suggested that by directing laser light at the atmosphere, an artificial light source (due to Mie scattering of dust or Rayleigh scattering due to molecules or resonance scattering of sodium atoms) of required brightness can be generated. Currently operational systems predominantly use the second or third methods. Sodium guide stars are preferred since they are higher up (almost 90 km) in the atmosphere and therefore sample a larger volume of the turbulence experienced by the astronomical object when compared to the Rayleigh scattering guide stars (which are at about 5 - 15 km) (Olivier and Max, 1994). A fairly comprehensive review of evolution of the laser technology used in LGS systems can be found in D'Orgeville and Fetzer (2016).

One of the disadvantages of using LGS is that they are insensitive to atmospheric tip-tilt . The absolute position of the LGS cannot be ascertained since the laser light travels through turbulent atmosphere. Therefore, an AO system would still require a natural guide star to perform image motion compensation. But, lower order terms of wavefront perturbations are more correlated over larger angles. For example, the isokinetic angle refers to the angle over which the slopes of the wavefronts arriving from different directions are well-correlated. This is greater than the isoplanatic angle. Despite this, a NGS for tip-tilt may not be available within the isokinetic angle. Therefore, the sky-coverage of LGS AO systems is also not 100%, but is better than NGS AO systems (B. L. Ellerbroek and Tyler, 1998). Olivier, Max, et al. (1993) discuss the effect of level of NGS tip-tilt correction on LGS AO systems in terms of AO performance (in terms of diffraction-limit) and sky-coverage. There are techniques being considered to estimate the tip-tilt information from laser guide stars themselves (Esposito, 1998). Another disadvantage of using

---

[14] The word "star" here can be a misnomer as it is used to denote any (typically point) bright source.

LGS is the finite height of the artificial source that we create. This is called the “cone effect” or “focal anisoplanatism”. This can be understood as follows: the light coming from a celestial object (scientific object, infinitely far away) traverses a volume of atmosphere that can be approximated as a cylinder. However, the artificial sources are at a finite distance from the telescope. The volume of atmosphere sampled by the wavefronts emitted by the LGS can be approximated to a cone. Therefore, the turbulence experienced by the scientific object and the LGS are not the same. This can be mitigated by opting for a guide star at a higher altitude or by using multiple guide stars (Tallon and Foy, 1990). Today, most large astronomical observatories use laser guide stars (selected references include Bonaccini et al. (1999), Bonaccini Calia et al. (2006), Le Mignant et al. (2006), Boccas et al. (2006), and Saito et al. (2010)). Upcoming facilities like the Thirty Meter Telescope (TMT) (Boyer, B. Ellerbroek, et al., 2010; Trubey et al., 2022), the European-Extremely Large Telescope (E-ELT) (Nijenhuis, Jonker, and Kamphues, 2022) and the Giant Magellan Telescope (GMT) (D’Orgeville, Bouchez, et al., 2013) have also planned for multiple guide star systems. Collectively these three telescopes are called the ELTs (Extremely Large Telescopes). Since most telescopes are crowded into some of the best observing sites in the world, one problem that must be kept in mind is the LGS of one telescope entering the field of view of another telescope (Summers et al., 2003; Gaug and Doro, 2018) or contamination of astronomical signals by scattering of laser light (Vogt et al., 2017).

Following this, there were developments in AO systems based on the scientific object under study or to overcome specific limitations of SCAO systems. The schematics of different types of AO systems that will be discussed here can be found in Figure 13 of Davies and Kasper (2012). For example, consider, LGS AO systems. We know that one of the issues that limits their performance is the cone effect. It is predicted that this will limit the maximum K-band Strehl for the ELTs to about 15% (Davies and Kasper, 2012). One way to overcome this is to use multiple guide stars to form a constellation in the sky and sense the wavefronts originating from multiple directions. Combining the information from all of them, a tomographic (3-D) reconstruction of the turbulent volume as experienced by the science object (typically on-axis at the center of the constellation) can be estimated (Tallon and Foy, 1990). This is then used to control a single DM (Baranec, Lloyd-Hart, Milton, Stalcup, Snyder, and R. Angel, 2006). Such systems are called Laser Tomographic AO (LTAO) (Costille et al., 2010; Wizinowich et al., 2023). The concept is similar to that used in CT scans where multiple 2-D scans are used to reconstruct a 3-D image. While it is preferred to use sodium LGS for LTAO systems, it is possible to use Rayleigh LGS for smaller telescopes using LTAO systems (Tatulli and Ramaprakash, 2013). LTAO systems are being considered for the ELTs (examples include an LTAO subsystem for GMT (Conan et al., 2013) and HARMONI on E-ELT (Fusco et al., 2010)).

Another drawback of SCAO systems is their limited AO-corrected field of view. The typical value is about 10-15 arc-seconds. This is because of the perturbations along different directions in the sky are not well-correlated. Therefore, in the case of extended objects (where the scientific field of view is larger) it is preferred to have larger AO-corrected field of view. This led to the development of Multi-Conjugate AO (MCAO) systems. Some early references to the concept include Dicke (1975) (and references therein), Beckers (1988) and B. L. Ellerbroek (1994). The idea is to use two or more deformable mirrors which will be conjugated to specific layers of the Earth's atmosphere so that the AO-corrected field of view can be increased beyond the isoplanatic size. Often, the DM is conjugated to the layer with the strongest turbulence. The work by Ragazzoni, Marchetti, and Valente (2000) was an experiment in tomographic reconstruction using three NGS for wavefront sensing to compensate the turbulence along a fourth star (approximately at the center of the field). This was followed by the MAD (Multi-conjugate Adaptive optics Demonstrator), which was one of the earliest experiments with MCAO. They considered two wavefront sensing modes. The star-oriented mode (Marchetti, Brast, Delabre, Donaldson, Fedrigo, Frank, Hubin, Kolb, Lizon, Marchesi, Oberti, Reiss, Soenke, et al., 2008) and the layer oriented mode (Ragazzoni, Almomany, et al., 2008). In the star-oriented mode, each WFS (SH-WFS) was pointed towards a guide star to measure the turbulence along that column of atmosphere. Then, a tomographic reconstruction was used to estimate the commands to the DM. In the layer-oriented mode, each WFS (Pyramid WFS) is for a layer of atmosphere. The light from all the guide stars are co-added onto the same detector (which is conjugated to the layer that is to be corrected). This is more photon efficient and therefore has better sky-coverage (in NGS systems). We know that the AO-corrected field of view of a SCAO system is the isoplanatic patch (θ_0). Similarly, Tokovinin, Louarn, and Sarazin (2000) derived an equivalent quantity, θ_M for MCAO systems (where M is the number of DMs). It depends on the C_N^2 profile, DM conjugate heights and scaled with wavelength and zenith angle. Other successful MCAO demonstrations include GeMS (Gemini Multi conjugated adaptive optics System) (Neichel, Rigaut, et al., 2013) on the Gemini South Telescope and the LINC-NIRVANA system (LBT INterferometric Camera and Near-InfraRed/Visible Adaptive iNterferometer for Astronomy) on the Large Binocular Telescope (LBT) (Herbst et al., 2018). One of the images taken using GeMS is shown in Figure 1.8 (right). It also shows images of the same field taken without AO and with SCAO system. One can see the performance improvement in the two cases. Given their good performance over larger fields, the ELTS have also planned for MCAO systems like MORFEO (Multiconjugate adaptive Optics Relay For Elt Observations, formerly MAORY) on E-ELT (Diolaiti, 2013) and NFIRAOS (Narrow-Field InfraRed Adaptive Optics System) on TMT (Crane et al., 2018). A review of MCAO for astronomy can be found in Rigaut and Neichel (2018).

To further push the corrected field of view beyond the MCAO systems, another type of AO called the Ground Layer AO (GLAO) is used. It can provide corrected fields up to 10 - 20 arcminutes. However, the quality of correction is poorer when compared to MCAO systems. It is often called a “seeing improver” due to the low level of uniform correction over a wider field of view. GLAO has almost uniform correction over the entire field with performance peaking at the center of the field. Compared to this, MCAO offers better performance (higher Strehl) but peaking around/near the guide stars (Marchetti, Brast, Delabre, Donaldson, Fedrigo, Frank, Hubin, Kolb, Lizon, Marchesi, Oberti, Reiss, Santos, et al., 2007). GLAO was proposed by Rigaut (2002). The concept was proposed when it was identified that a major contribution to the turbulence was the presence of a strong ground layer. The principle is to measure the wavefront along multiple directions. By averaging the measurements along different directions, we compute the contribution of the ground layers (effect of higher layers is cancelled). Then, the correction is applied to a single DM that is conjugated to a ground layer of the atmosphere. An analytical estimate of the performance of GLAO systems is given in Tokovinin (2004). The first GLAO demonstrations include Baranec, Lloyd-Hart, Milton, Stalcup, Snyder, Vaitheeswaran, et al. (2007) and Marchetti, Brast, Delabre, Donaldson, Fedrigo, Frank, Hubin, Kolb, Lizon, Marchesi, Oberti, Reiss, Santos, et al. (2007). Other demonstrations include Hart et al. (2008), Orban de Xivry et al. (2015), Abdurrahman et al. (2018), and Madec et al. (2018).

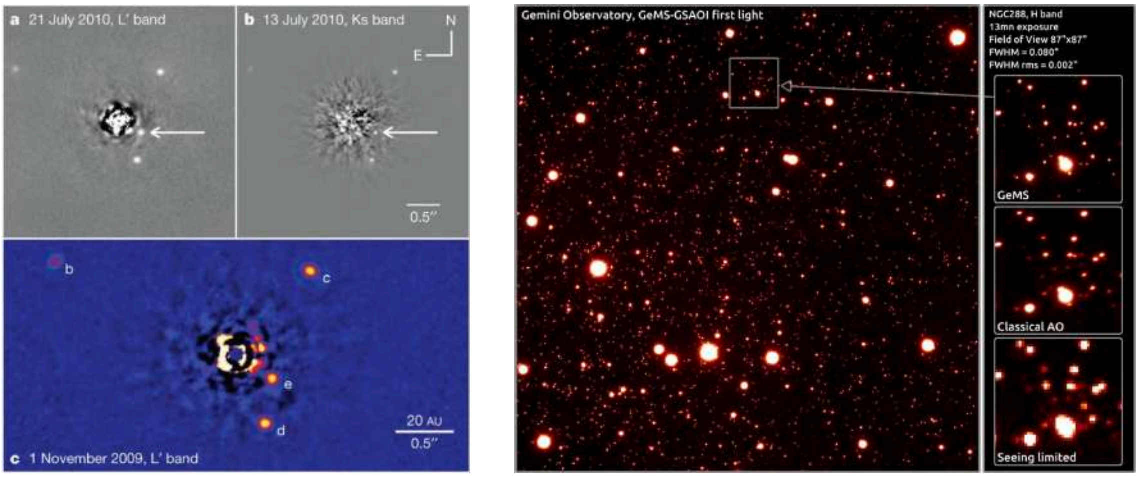

Figure 1.8: Images recorded with AO systems. Left (Image credit: Marois et al. (2010)): HR 8799 system showing an occulted star with at least 4 planets around it. Data taken using Keck II telescope over seven years. (NOTE: This image is AO + post-processed). Right (Image credit: Neichel and Rigaut (2012)): Images recorded with GeMS (Gemini Multi conjugated adaptive optics System). There are three images inset. From top to bottom, they are the MCAO, SCAO and seeing-limited images, respectively. The difference in the AO-corrected fields of the MCAO and SCAO systems can be seen by the sharper images over a wider field in the former case.

Recently there has been an increase in the study of circumstellar environments of stars (includes exoplanets, debris disks and protoplanetary disks). As of August 2024, there have been a total of 5743 confirmed exoplanets[15] detected using various techniques. Of these, we have direct images of only 82 planets (less than 2% of all confirmed planets). Direct imaging refers to analyzing only the light from the planet. There are two main difficulties in this technique. They are, the close angular proximity of the star and planet (can be as low as few hundredths of an arc-second) when viewed from the Earth and the differences in their brightness (can be between 10^4 to 10^{10})

---

[15] Exoplanet Archive

(Galicher and Mazoyer, 2024). For resolving two objects that are very close, we need to operate large telescopes at (or very close to) their diffraction-limits. The brightness difference can be overcome by using starlight suppressing techniques like coronagraphy or interferometry. For this as well, it is necessary to obtain a stable PSF in the focal plane. Therefore, AO becomes essential in the direct imaging of circumstellar environments. However, simple SCAO systems are not sufficient due to the extremely tight tolerances required. The AO systems must perform very high degrees of correction (Strehl ratio $> 80\%$ at near-IR, total residual error of the order of few tens of nm) at very fast rates (typically of the order of 1 - 3 kHz) over very small angles (typically less than an arc-second) (Guyon, 2018). These systems are called Extreme AO (ExAO or XAO) systems. The concept was first proposed by J. R. P. Angel et al. (1994) and Nakajima (1994). Some of the functional ExAO systems include SPHERE (Spectro-Polarimetric High-Contrast Exoplanet REsearch) at VLT (Very Large Telescope) (Beuzit et al., 2006), GPI (Gemini Planet Imager) at Gemini South Telescope (Macintosh, Graham, et al., 2006), MagAO (Magellan AO) on the Clay Telescope (Morzinski et al., 2014), SCExAO (Subaru Coronagraphic Ex AO) on the Subarau telescope (Jovanovic et al., 2015). All future ELTs have plans for ExAO systems (Hinz et al., 2012; Macintosh, Troy, et al., 2006; Kasper, Verinaud, and Mawet, 2013).

Future large ground-based stellar telescopes have all planned for the availability of multiple flavors of AO based on the scientific requirement (Hubin et al., 2006; Bouchez et al., 2023; Boyer, L. Wang, et al., 2023; Busoni et al., 2023; Bertram et al., 2023). This shows that the future of ground-based astronomy is intricately tied with AO systems. Since this thesis focuses on AO systems for solar telescopes, the following discussions shall be restricted to a daytime perspective.

1.4 Solar AO

1.4.1 The challenges

While the general principle of operation of solar and stellar AO systems are the same, there are some issues that are specific to the former (T. R. Rimmele, 2004). The first is the issues with wavefront sensing. During the daytime, there are no point reference sources which can be used by the WFS. Therefore, wavefront sensors have to operate on extended features like solar granulation (typical size of about $2''$) which are intrinsically low contrast and are time varying. WFS must be developed for granulations as they are ubiquitous on the solar disk and are independent of solar activity (unlike sunspots and pores). Furthermore, granulations are low contrast features. Therefore, a sensor that can work with granulations can also work with high contrast features like sunspot and pores. SHWFSs are currently favoured by solar AO systems. The second issue is the stronger daytime turbulence (smaller r_0) compared to that of nights. The near-Earth turbulence is stronger due to heating by the ground. Therefore, solar telescopes are typically raised to 20 - 40 m above the ground. However, solar telescopes are also typically smaller in diameter than stellar telescopes. So the D/r_0 ratio during daytime is comparable to that of 8 m class telescopes at nighttime (Rigaut and Neichel, 2018). But the faster evolving turbulence and the typical observations being at visible (shorter) wavelengths can place a more stringent bandwidth requirement for better performance of solar AO systems.

1.4.2 History of Solar AO

The first AO experiments for solar telescopes were carried out at the 76 cm Dunn Solar Telescope (then named Vacuum Tower Telescope, VTT) at the Sacramento Peak Observatory (Hardy, 1980). It was used to observe single or double star systems as well. During operation with the Sun, the performance of the image stabilization system was found to be satisfactory but the AO loop performance was unpredictable. This was followed by other works like Dunn, Streander, and Lühe (1989) and Dunn (1990).

One of the most challenging parts of a solar AO system is the wavefront sensing. There is a lack of point sources during the daytime; wavefront sensing must be done on low contrast, extended targets like granulations that are perennial features on the surface of the Sun. Initial techniques for wavefront sensing included SHWFS, lateral shearing interferometers (Wyant, 1975), OD-WFS (Optical Differentiation WFS) which uses a mask based on the solar scene under observation and works on the principle of Foucault knife-edge test (von der Luhe, 1988; T. R. Rimmele and R. R. Radick, 1996; Schmidt and I. von der Lühe O., 2007), the Focal Volume Technique (FVT, S. R. Restaino (1992) and Denker, S. Restaino, and R. Radick (1993)) and curvature WFS (Kupke, F. J. Roddier, and Mickey, 1994). Lockheed developed an AO system with a quad cell based WFS and segmented DM (Acton and Dunn, 1993). The operation was limited to high-contrast regions like pores or sunspots. One of the earliest systems that successfully utilized the correlating SHWFS for solar AO was the low-order AO system at NSO (T. R. Rimmele and R. R. Radick, 1998; T. R. Rimmele, 2000). This method is now widely used by most solar AO systems. Following this, a solar AO system was also implemented at the Swedish Solar Telescope (SST). First with a 50 cm telescope and a 37-electrode system (Scharmer, Shand, et al., 2000), then, with a 1 m telescope (Scharmer, Bjelksjo, et al., 2003). Soon after, there were other systems at the 70 cm Vacuum Tower Telescope (VTT) at Tenerife (van der Lühe et al., 2003) and at the 1.5 m McMath-Pierce telescope at Kitt Peak, Arizona (Keller, Plymate, and Ammons, 2003). The goal in the VTT AO system was to also compensate for the slowly-varying aberrations due to thermal effects in the telescope. Their experiments also led them to explore an MCAO system to improve the correction over a wider field (Berkefeld, Soltau, and O. von der Lühe, 2003). On the other hand, the McMath-Pierce telescope focused on developing a low-cost solar AO system in the infrared. These were some of the earliest low-order AO systems developed for solar telescopes.

Other efforts include the AO systems for the 1.5 m GREGOR solar telescope on Teide Observatory (O. von der Lühe, Berkefeld, and Soltau, 2002), the 50 cm MAST (Multi Application Solar Telescope) at the Udaipur Solar Observatory (USO) in India (Sridharan, Bayanna, et al., 2005; Bayanna, Kumar, et al., 2008), the 60 cm domeless telescope at Hida Observatory, Japan (Miura et al., 2008), THEMIS (Téléscope Héliographique pour l'Etude du Magnetisme et des Instabilité

Solaires) at Teide Observatory (Gelly et al., 2016), the 1 m New Vacuum Solar telescope (NVST) in China (C.-H. Rao et al., 2016) and, the 38 cm Kodaikanal Tower Telescope (KTT) at the Kodaikanal Observatory, India (Rengaswamy, Banyal, et al., 2020; Mathur et al., 2023). Meanwhile, the first generation low-order systems were being upgraded to high-order AO systems. For example, at BBSO, a high-order AO system was first developed for the 65 cm vacuum telescope (Didkovsky, Denker, et al., 2003; Didkovsky, Dolgushyn, et al., 2003). It was later upgraded to the AO-308 system for the 1.6 m New Solar Telescope (NST, also known as the Goode Solar Telescope, GST) at the Big Bear Solar Observatory (BBSO) (Shumko et al., 2014). The 37-electrode system of the SST was upgraded to an 85-electrode system (Scharmer, Sliepen, et al., 2024). With large aperture telescopes like DKIST and EST, AO becomes essential to achieve the desired performance. Some selected references of the AO systems for the two include Johnson, Cummings, et al. (2016), Marino, Carlisle, and Schmidt (2016), and Johansson et al. (2018) and Berkefeld and Soltau (2010), Montilla et al. (2016), and Femenía-Castella et al. (2022).

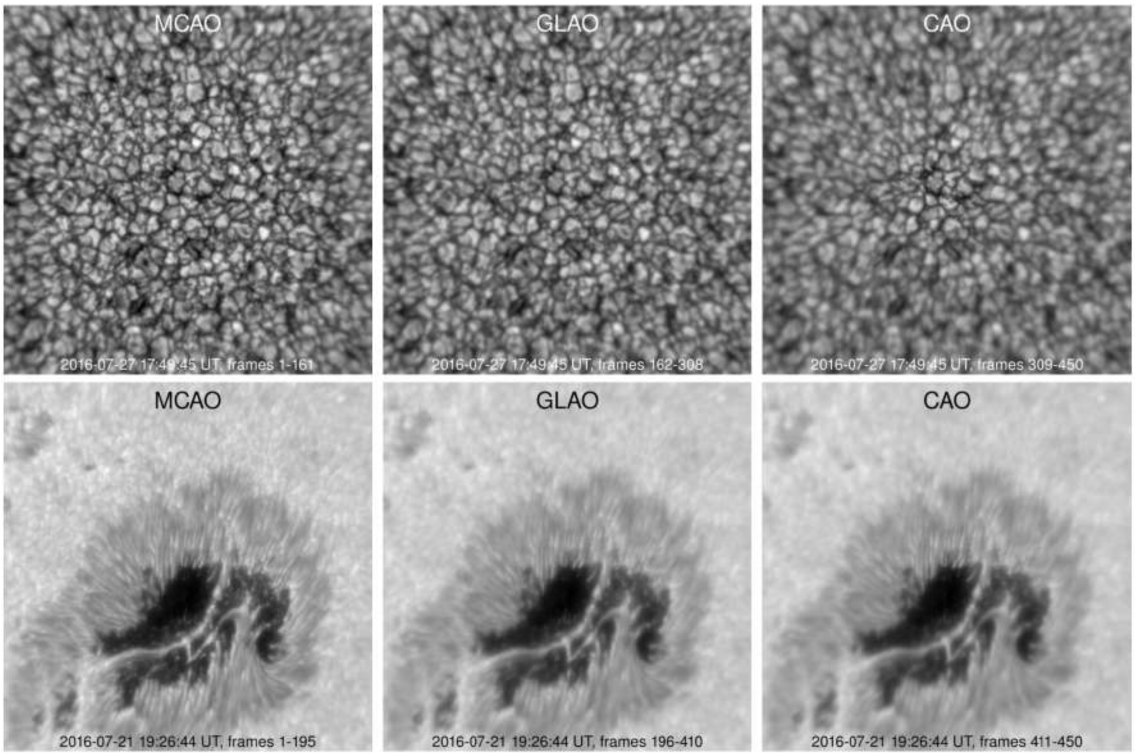

Figure 1.9: Images showing different levels of AO correction. Top row: solar granulation, bottom row: sunspot. Images recorded at 705.7 nm with a $53'' \times 53''$ field of view. From left: the columns correspond to MCAO, GLAO and SCAO systems. Image credit: Schmidt, Gorceix, P. R. Goode, et al. (2017)

.

After the success of SCAO systems, with the desire to increase the AO-corrected field of view, many solar telescopes had started planning for MCAO systems. A solar MCAO system was designed for DST (Moretto et al., 2004) and integrated at the telescope. Preliminary results can be found in Langlois et al. (2004) followed by T. Rimmele, Richards, et al. (2006) and T. R. Rimmele, Woeger, et al. (2010). Experiments were also planned and carried out at VTT (Berkefeld, Soltau, and O. von der Lühe, 2002) and GREGOR (Berkefeld, Soltau, Schmidt, et al. (2010)). These early experiments were to test out MCAO concepts. So, the MCAO module for VTT was added downstream to the SCAO module (second WFS is blind to pupil DM) to enable easy integration and was not optimized for performance. Preliminary results from VTT can be found in Berkefeld, Soltau, and O. von der Lühe (2005). The initial GREGOR design was such that, all the WFS were downstream to all the DMs (Berkefeld, Soltau, and O. von der Lühe, 2006). This was later modified so that the pupil WFS was upstream of the high-layer DMs to avoid misregistration between the pupil DM and WFS (Schmidt, Berkefeld, Heidecke, et al., 2014). An MCAO system was also developed for NVST (Zhang et al., 2016).

One of the big breakthroughs was the on-sky demonstration of MCAO called *Clear* system on NST at BBSO which had an AO-corrected field of about 53$''$ (Schmidt, Gorceix, P. R. Goode, et al., 2017). From Figure 1.9, we can see the difference between MCAO, GLAO and SCAO systems on the image quality of solar images. Each column of images from left to right represent data taken with the three systems respectively. The top row is a quiet-sun region of solar granulation and the bottom row is an active-region showing a sunspot. We can see that from SCAO to GLAO, there is an increase in the corrected field of view but the degree of correction is poorer (image is less sharp). But from GLAO to MCAO, there is an increase in sharpness of the image. Therefore MCAO systems are preferred when we require good correction over a wider field of view.

The *Clear* system was also used to identify the best sequence of DMs in an MCAO loop. There have been several theoretical and simulation-based studies to identify the best order of DMs in an MCAO system including Flicker (2001), Farley et al. (2017) and van Dam et al. (2023). The first two suggest that correcting for the lower layers first is preferable whereas van Dam et al. (2023) suggests the reverse. Schmidt, Gorceix, and P. Goode (2020) performed experiments with the pupil DM upstream and downstream of the high-altitude DMs. They found that having the pupil DM downstream was better but the improvement was very small.

1.4.3 Assessing image quality

The image quality of ground-based solar telescopes has been studied in detail over several decades, starting from the seminal work of Kiepenheuer (1964). With the advent of the theory on the effects of atmospheric turbulence on ground-based telescopes (F. Roddier (1981) and the references therein), it is now well understood that the image quality is characterized by a single parameter known as Fried's parameter (r_0) or the atmospheric coherence diameter. In ground-based solar imaging, r_0 is directly linked with the contrast of the images (F. Roddier, 1981). It is interesting to note that the use of image contrast as a measure of image quality was proposed by Kiepenheuer

(1964) even before the invention of the parameter r_0. As we saw in the previous section, modern large solar telescopes (Scharmer, Dettori, et al., 2003; Cao et al., 2010; Berkefeld et al., 2012; C. Rao et al., 2016; Venkatakrishnan et al., 2017; Johnson, Johansson, et al., 2020) are invariably equipped with adaptive optics (AO) systems to mitigate the deleterious effects of the Earth's atmospheric turbulence on the image quality. Understandably, the performance of the adaptive optics systems depends on the characteristic parameters of the atmosphere, namely, r_0 and the atmospheric coherence time τ_0.

The commonly used metrics to quantify image quality like Strehl ratio and encircled energy require knowledge of the PSF. For stellar telescopes, since most objects are point sources, this parameter is useful in characterising the associated AO systems. However, in the case of solar telescopes where the object is extended in nature, this parameter cannot be determined easily. Therefore, other metrics like rms granulation contrast are used to quantify the performance of solar telescopes and AO systems (Popowicz et al., 2017).

1.5 Motivation of thesis

From the discussions in Section 1.4.2, it is now clear that AO systems are essential in the functioning of future ground-based (solar) telescopes (Sankarasubramanian and T. Rimmele, 2008). India also has plans for a large ground-based optical solar telescope called the National Large Solar telescope (NLST) (Singh, 2008). It will have a 2 m aperture and is expected to be near Pangong Tso at Merak, Hanle (latitude: $33^\circ\ 43'$ N, longitude: $78^\circ\ 53'$ E). At 500 nm, the diffraction-limit of the telescope will be around $0.05''$. However, the median seeing at Merak is 4.5 cm at 500 nm (Rengaswamy, Ravindra, and Prabhu, 2019). This translates to a FWHM of about $2.3''$. Therefore, we need AO systems to realise the full potential of the telescope. In this context, the Indian Institute of Astrophysics has initiated a solar AO program. The overall goal of the program is develop local expertise in solar AO and related systems by developing and testing the capability on existing smaller telescopes.

1.5.1 Scope of this thesis

The thesis is titled "Solar Multi-Conjugate Adaptive Optics". It is imperative to explain the scope of the thesis under this title, considering the limited time frame for carrying out the work. At the start of this thesis work, we considered the status of solar AO within the country. At the time (August 2020), a low-order AO system was already demonstrated on the 50 cm MAST at USO. With the next logical step being MCAO, we focused on the same. This ensures the novelty of the work which is expected in a thesis. Although the long-term goal of the solar AO program at IIA is MCAO, we would need to design and demonstrate SCAO at our telescope to start with. Furthermore, other experiments like turbulence strength profiling and simulating the performance of solar AO systems which are related to SCAO/MCAO development had not been carried out. Therefore, in this thesis we have focused on measuring the daytime turbulence strength profile, estimating the isoplanatic angle during the daytime (for seeing-limited imaging), the design of SCAO and MCAO systems for KTT and performance evaluation of solar telescopes and AO systems using simulations. These will contribute to the institution's goals as well.

For the purposes of this thesis, we have primarily worked with the 38 cm Kodaikanal Tower Telescope (KTT) at the Kodaikanal Observatory (KO, latitude: 10° 14′ N, longitude: 77° 5′ E), Tamil Nadu for our studies (Bappu, 1967). A schematic of the telescope is shown in Figure 1.10. For all our experiments, we have used an aperture mask to reduce the size of the telescope to 36 cm. Therefore, for the reminder of this thesis, we will refer to it as a 36 cm telescope. One of the key design parameters of an MCAO system is the height to which the DM must be conjugated. For this, knowledge of the vertical distribution of the turbulence strength above the site is crucial. Thus far, there have been no $C_N^2(h)$ measurements at KO. So, the first part of this thesis deals with turbulence profiling experiments at KO. We have used two techniques to measure the near-Earth and high-altitude turbulence above our telescope. The techniques, simulations, experiments at the observatory and the results are detailed in Chapter 2.

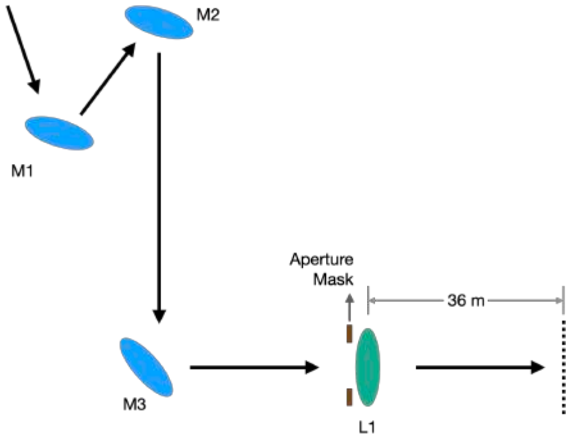

Figure 1.10: Schematic of KTT optical set-up (not to scale). The three blue ovals represent the primary (M1), secondary (M2) and tertiary (M3) mirrors. M1 and M2 are located on a tower roughly 11 m above the ground. M2 directs the light vertically down onto M3 which reflects it into the tunnel. A movable achromatic doublet of 38 cm diameter (L1, green oval) is at some distance away from M3. We have used a mask (brown bars) to reduce the aperture to 36 cm. The image of the Sun is formed 36 m away from L1 at the prime focus (dotted line).

As mentioned earlier, another parameter that quantifies atmospheric turbulence and is useful in the context of AO is the isoplanatic angle (θ_0). It is often calculated from turbulence profiling experiments using the relationship between r_0 and the strongest layer of turbulence (Equation 1.8). We have developed a new method that allows us to estimate it directly using deconvolution on long-exposure ground-based images of the Sun. To the best of our knowledge, this is one of the first direct methods to measure the isoplanatic angle in the daytime. For this, we have used the data taken using the 20 cm H-α telescope at Merak (Ravindra et al., 2018). We have opted for data taken at Merak since this is an extension of earlier studied using deconvolution on the data recorded from Merak (Rengaswamy, Ravindra, and Prabhu, 2019; Unni. C et al., 2021). The details of the technique and the results of our analysis are summarized in Chapter 3.

We have made optical designs of AO/MCAO systems for KTT. The design considerations and possible limitations of the systems are discussed in Chapter 4.

Finally, as seen in Section 1.4.3, one of the existing problems in solar instrumentation is the quantification of the system performance due to the inapplicability of traditional metrics like PSF (lack of access to the PSF). Under such circumstances, how can one possibly quantify the performance of a large ground-based solar telescope? What is the metric that could be specified as a requirement for the telescope (for example, to a telescope manufacturer/vendor)? As AO is likely to be working efficiently only under good atmospheric conditions (large r_0 and high τ_0), what is the metric that can be used for image quality: (a) when conditions are not optimal for AO to be operational (no-AO mode), (b) when conditions are optimal for AO but only a partial compensation of the wavefront distortion is achieved (low order AO), (c) when a high degree of correction is done under good atmospheric conditions? These questions are answered in as much quantitative nature as possible in Chapter 5.

Chapter 2

Turbulence strength profile estimation

"When I meet God, I am going to ask him two questions: Why relativity? And why turbulence? I really believe he will have an answer for the first."

(an apocryphal quote often attributed to) Werner Heisenberg.

The work presented in this chapter has been reported in the following publications:

Forward modelling of turbulence strength profile estimation using S-DIMM+
Saraswathi Kalyani Subramanian, Sridharan Rengaswamy, 2023, **Society of Photo-Optical Instrumentation Engineers (SPIE) Conference Series**, 12638.

Daytime turbulence strength profile measurement at Kodaikanal Observatory
Saraswathi Kalyani Subramanian, Sridharan Rengaswamy, Prasanna Gajanan Deshmukh, Binukumar G. Nair, S. Mahesh Babu, 2024, **Journal of Astronomical Telescopes and Instrumentation Systems**, 10(3), 039004.

2.1 Introduction

The effect of the Earth's atmosphere on ground-based astronomy is a well-studied problem. Over the years, the instruments for studying the atmosphere have also advanced and become more sophisticated along with the evolution of AO systems. They differ in the principle with which they study the atmosphere (or its effects) and the quantities they measure. As stated in Section 1.5.1, we are interested in measuring the $C_N^2(h)$ profile during the day. Therefore, we will focus on techniques relevant to the same.

One of the earliest methods to estimate the turbulence profile involved using temperature sensors to measure the temperature structure function ($D_T(r)$). Then, the turbulence strength profile ($C_N^2(h)$) was estimated using the relationship between it and the temperature structure constant (C_T^2). Typically, the sensors are hoisted using a mechanism like a balloon (Bufton et al., 1972; Barletti et al., 1976). Following this technique, we used a tethered balloon to measure the near-Earth turbulence at KO. Hereafter, we refer to this method as balloon-measurements in this thesis.

Another way to study the properties of the atmosphere is to use the images obtained using ground-based telescopes. One of the effects of turbulence on short-exposure images is the random motion of the image on the detector plane (also known as "angle of arrival fluctuations"). This is due to a global tilt of the wavefront. Some early work in measuring the image motion of solar images include Brandt (1969) and Brandt (1970). By measuring the relative shift between consecutive images, the properties of the turbulence can be estimated. An important instrument developed to take advantage of this random image motion property is the Differential Image Motion Monitor (DIMM). The first comprehensive study of seeing using DIMM was reported by Sarazin and F. Roddier (1990). The principle of the method is as follows: the same object is imaged using two small apertures (with a common mount). A finite angular tilt is introduced in the light path of one of the apertures so that two identical images of the same object are formed at the focal plane. Both images will exhibit random motions at the focal plane due to atmospheric turbulence. The differential image motion of the two images is related to the Fried's parameter by (Sarazin and F. Roddier, 1990):

$$\sigma_l^2 = 2\lambda^2 r_0^{-5/3}\left[0.179D^{-1/3} - 0.0968d^{-1/3}\right], \tag{2.1}$$

and

$$\sigma_t^2 = 2\lambda^2 r_0^{-5/3}\left[0.179D^{-1/3} - 0.145d^{-1/3}\right]. \tag{2.2}$$

Equations 2.1 and 2.2 represent the longitudinal and transverse differential image motions (σ_l and σ_t, respectively) measured by two apertures of size 'D' that are separated by a distance 'd'. Longitudinal image motion refers to the image motion along the line connecting the centres of the two apertures. Similarly, transverse image motion refers to the motion along the direction perpendicular to the line connecting the apertures. 'D', 'd' and λ are known instrumental parameters, and σ_l and σ_t are found from the DIMM measurements (ensemble averaged), allowing us to estimate r_0 at the site. The elegance of this instrument is in its use of differential image motion. This reduces the effect that other sources (telescope vibration, jitter, etc...) have on the image motion measurements, leaving only the contribution of the atmosphere. When the object under study is the Sun, and the instrument is called S-DIMM (Solar-DIMM) (Beckers, 2001; Kawate et al., 2011). Typically, the limb region of the Sun was imaged and used to estimate the image motion for two reasons. First, there is a better contrast of the limb against the dark background sky. Secondly, if a part of the solar disk with an angular size greater than the isoplanatic angle is used, then the different regions of the image are subject to different turbulent volumes of the atmosphere. Therefore different parts of the image will have different image motions. The resulting image will be distorted and this can be avoided by using the solar limb. However, one disadvantage of using the image motion of the limb is that only the longitudinal image motion can be estimated (Beckers, 2001). While this still allows seeing estimation, having estimates along both directions gives a better SNR. Although the (S-)DIMM is a well-tested instrument for measuring r_0, it only provides information about the integrated effect of the turbulence. We, however, are interested in knowing the vertical distribution of the turbulence above our telescope. This can be done by extending the (S-)DIMM. Instead of using two apertures, the whole pupil plane can be re-imaged onto a SHWFS and split into several sub-pupils.

The idea of using a SHWFS to measure the high-altitude turbulence during the daytime was first put forth by Waldmann, Berkefeld, and O. von der Lühe (2007). Following this, Scharmer and van Werkhoven (2010) proposed S-DIMM+ (similar to SLODAR (SLOpe Detection And Ranging, (Wilson, 2002)) for nighttime), which uses a SHWFS to capture images of a region on the Sun. Then, the covariances of the differential image motion of the different sub-aperture images are used to determine the C_N^2 profile. It was later repeated with modifications at the Big Bear Solar Observatory (BBSO) (Kellerer et al., 2012) and Fuxian Solar Observatory (FSO)(Z. Wang et al., 2018). The measurements were all made with telescopes of apertures 1 m or more since large telescope apertures are required to measure the high altitude turbulence. This is because, in this method, the largest separation between the lenslets (as projected on the pupil plane) determines the maximum height up to which the system is sensitive to turbulence. Further improvements include the work by Ren et al. (2015) called Multi Aperture Seeing Profiler (MASP), using a combination of two smaller telescopes to achieve the performance of a single larger telescope and by Ran, Zhang, and C. Rao (2024) using auto-correlation in the place of cross-correlation. We have used the S-DIMM+ proposed by Scharmer and van Werkhoven (2010) to measure the higher-altitude seeing at our site.

The final daytime turbulence strength measurement technique we considered works by measuring the scintillation in the light from the source. As seen in Section 1.2, the image motion or blurring (seen in short and long-exposure images, respectively) is the effect the atmosphere has on the phase of the wavefront. Another effect manifests as amplitude fluctuations (scintillation). The concept was first put forth by Seykora (1993). It was further extended by Beckers (1993b) and is known as SHABAR (SHAdow BAnd Ranging) (Beckers, 1999; Liu and Beckers, 2001). It uses an array of photo-detectors to measure the scintillation in solar flux over several baselines. The disadvantage of this method is the measurements are made over the full disk of the Sun (0.5° field-of-view). This makes it insensitive to high altitude turbulence or requires large baselines to overcome the height limitation. Nevertheless, it was extensively used to measure the near-ground turbulence in the DKIST (Daniel K. Inouye Solar Telescope; formerly ATST, Advanced Technology Solar Telescope) site survey (Socas-Navarro et al., 2005). As reported in Hickson and Lanzetta (2004), a baseline of 2.6 m would allow measurement of turbulence profile only up to a height of 300 m. Furthermore, there are challenges in maintaining the pointing of the array and tracking the source. Therefore, we did not consider this method for our experiments.

In this chapter, we start with the principle of both methods in Section 2.2. Then, we present the details of the simulation work carried out for S-DIMM+ in Section 2.3. We have carried out experiments at KO using the balloon instrument and S-DIMM+ instrument. The details of the instrument are described in Section 2.4. The data recorded and their analysis is described in 2.5. The first turbulence strength profiling campaign results at KO are summarized in Section 2.6.

2.2 Methods

The basic working principles of the two methods we used in our turbulence profiling experiment are summarized in the following subsections.

2.2.1 Balloon-measurements

The first method we considered was the balloon-measurements. This is one of the simplest techniques to measure the C_N^2 profile at a site, and it can be used for both daytime and nighttime estimates. Another advantage of this method is that it enables direct measurement of the temperature structure function, $D_T(r)$. This is very useful as it indicates the turbulence parameters at the site without the assumptions of any models. It is also used widely by those interested in atmospheric sciences.

$D_T(r)$ is measured as the mean square difference temperature fluctuations between two points separated by a distance 'r.' By mounting two temperature sensors spatially separated by a certain distance and having a mechanism to displace them in height, the temperature structure function can be measured as a function of height (selected references include Bufton et al. (1972), Barletti et al. (1976), Abahamid et al. (2004), McHugh, Jumper, and Chun (2008), Roadcap and Tracy (2009), and van Iersel et al. (2019)). Then, assuming Kolmogorov's theory of turbulence, the temperature structure function parameter (C_T^2) can be found as (F. Roddier, 1981):

$$D_T(r) = C_T^2 r^{2/3}. \tag{2.3}$$

Then, the turbulence strength profile, $C_N^2(h)$ can be estimated as:

$$C_N^2(h) = \left[80 * 10^{-6} \frac{P(h)}{T^2(h)}\right]^2 C_T^2(h), \tag{2.4}$$

where P is the pressure in milli bar and T is the absolute temperature in kelvin.

2.2.2 S-DIMM+

S-DIMM+ (Scharmer and van Werkhoven, 2010) is an optical method of determining the C_N^2 profile. While the traditional (S-)DIMM uses only two images, S-DIMM+ produces multiple subaperture images of the same region of the Sun using a SHWFS. The analysis is done by estimating the differential image motion between pairs of sub-fields within pairs of sub-aperture images at a time. We are using the Fourier transform cross-correlation (FCC) method for estimating the image motion (see Appendix A). The size of the sub-field used for determining the image motion (ϕ), the minimum separation between two lenslets (as projected onto the pupil plane, s_{min}), and the number of lenslets across the diameter (N_{ll}), determine the maximum height H_{max} in the atmosphere up to which the instrument is sensitive. Similarly, the minimum height δh is determined by the maximum possible separation between two sub-fields (α_{max}) and s_{min}. They are given as:

$$\delta h = \frac{s_{min}}{\alpha_{max}} \quad \text{and} \quad H_{max} = \frac{s_{min} N_{ll}}{\phi}. \tag{2.5}$$

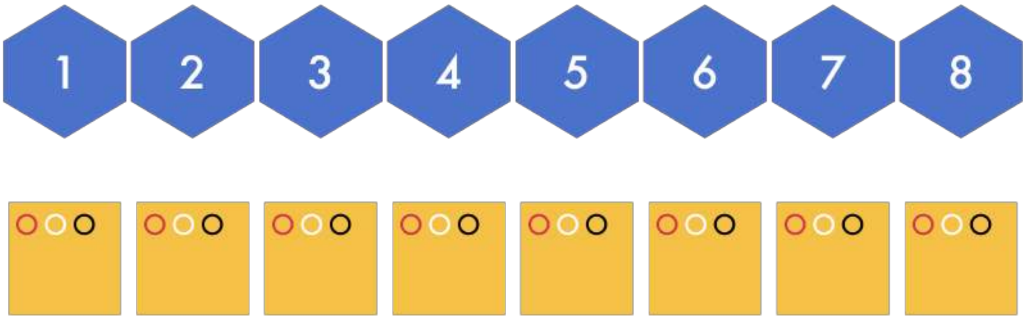

Figure 2.1: Pictorial representation of one row of lenslets in pupil plane (shown as blue hexagons in the top row). The numbers on each lenslet are marked for ease of understanding and do not carry any further meaning. The yellow squares in the bottom row represent the solar images in image plane formed by each corresponding sub-aperture in the top row. Refer to text for explanation of the circular fields marked in each sub-aperture image. (Image not to scale).

First, two sub-apertures are chosen. Only the relative separation between them (written generally as s) is important and not their absolute positions. For example, in the top row of Figure 2.1, consider the lenslets 1 and 2. The separation between them is s. There exist a total of seven possible combinations of lenslets having this separation (2 and 3, or 3 and 4, and so on). Then, two sub-fields within their images are chosen. Again, only the relative separation between the fields (written generally as α) is considered. Consider the images formed by sub-apertures 1 and 2 in the bottom row of Figure 2.1. Let the first sub-field chosen be represented by red circles. This is taken as zero field angle. If the second sub-fields are the white circles, then they are said to be at an angle α (= a) away. Alternatively, if the sub-fields represented by the black circles are chosen as the second set of sub-fields, they are at an angle α (= $2a$) away from the red circles. Similar to the pupil plane separation (s), there are redundant combinations in the image plane separations as well. Once the two sub-fields are chosen, the longitudinal (δ_{x1}) and transverse (δ_{y1}) image motions measured using the first sub-fields of two sub-apertures, and the longitudinal (δ_{x2}) and transverse

(δ_{y2}) image motions measured using the other sub-fields of the same two sub-apertures are estimated. The underlying assumption of S-DIMM+ is that the total image motion measured (δ_{x1}, δ_{x2}, δ_{y1}, δ_{y2}) can be expressed as the sum of the individual image motions due to all the layers. The two components of image motion between the first pair of two sub-fields (arbitrarily assumed as the zero field position) formed by two sub-apertures having a separation of s in the pupil plane can be written as:

$$\delta_{x1}(s,0) = \sum_{n=1}^{N_a} \big(x_n(s) - x_n(0)\big) \text{ and } \delta_{y1}(s,0) = \sum_{n=1}^{N_a} \big(y_n(s) - y_n(0)\big). \tag{2.6}$$

Here, $x_n(s) - x_n(0)$ refers to the longitudinal image motion between the sub-fields due to the n^{th} layer. Similarly, $y_n(s) - y_n(0)$ refers to the transverse image motion between the same two sub-fields due to the n^{th} layer. 'N_a' refers to the total number of layers in the atmosphere.
The two components of image motion between the second pair of sub-fields (formed by the same two sub-apertures) which are at an angle α from the first pair can be written as:

$$\delta_{x2}(s,\alpha) = \sum_{n=1}^{N_a} \big(x_n(s+\alpha h_n) - x_n(\alpha h_n)\big) \text{ and } \delta_{y2}(s,\alpha) = \sum_{n=1}^{N_a} \big(y_n(s+\alpha h_n) - y_n(\alpha h_n)\big). \tag{2.7}$$

The terms within the summations of Equation 2.7 can be interpreted similar to Equation 2.6, but for the other sub-field. The process is repeated for all combinations of sub-aperture images and sub-fields to build the longitudinal and transverse covariance matrices, $M_x(s,\alpha)$ and $M_y(s,\alpha)$, respectively. FCC is used to estimate the image motions. The time averages of the two covariance matrix measurements are expressed as:

$$\langle M_x(s,\alpha)\rangle = \sum_{n=1}^{N_a} c_n F_x(s,\alpha,h_n), \tag{2.8}$$

and

$$\langle M_y(s,\alpha)\rangle = \sum_{n=1}^{N_a} c_n F_y(s,\alpha,h_n). \tag{2.9}$$

The functions F_x and F_y are given by:

$$F_x(s,\alpha,h_n) = 0.5 * I\left(\frac{\alpha h_n - s}{D_{\text{eff}}}, 0\right) + 0.5 * I\left(\frac{\alpha h_n + s}{D_{\text{eff}}}, 0\right) - I\left(\frac{\alpha h_n}{D_{\text{eff}}}, 0\right), \tag{2.10}$$

$$F_y(s,\alpha,h_n) = 0.5 * I\left(\frac{\alpha h_n - s}{D_{\text{eff}}}, \frac{\pi}{2}\right) + 0.5 * I\left(\frac{\alpha h_n + s}{D_{\text{eff}}}, \frac{\pi}{2}\right) - I\left(\frac{\alpha h_n}{D_{\text{eff}}}, \frac{\pi}{2}\right), \tag{2.11}$$

where the function I is given by Fried (1975). As reported in Scharmer and van Werkhoven (2010), we too noticed underestimation in the calculations of Fried (1975) (refer to Appendix B for more details). Furthermore, the approximate form of this equation for the longitudinal and transverse cases is given by Equations 2.1 and 2.2, which are valid when the separation between the sub-apertures is greater than half the sub-aperture diameter. The F_x and F_y terms of Equations 2.1 and 2.2 are a function of the variables 's' and α, the linear and angular separation between the regions used for image motion measurements in the pupil and image planes, respectively, h_n - the height above the ground in the Earth's atmosphere that is being probed, and D_{eff}, is the effective diameter of the sub-pupil projected at different heights. These two functions can be estimated using the system parameters.

The left-hand side of Equations 2.8 and 2.9 are calculated from the sub-aperture images (simulated or observed). Each element of the matrices corresponds to two sub-fields having a combination of the linear pupil plane (s) and angular image plane (α) separations which were used to determine the image motions. By iterating over all possible combinations of s and α, the two matrices can be constructed. One frame of lenslet array images is used to compute one longitudinal and one transverse covariance matrix. A time series of such frames is used for determining the ensemble average. The equations are then solved for the c_n coefficients using a linear least squares fit. Then, using Equations 2.12 and 2.13, we can determine the r_0 values and the turbulent strengths of the layers ($C_N^2 dh$) at different heights, respectively as:

$$c_n = 0.358\lambda^2 r_0^{-5/3}(h_n) D_{\text{eff}}^{-1/3}(h_n), \tag{2.12}$$

or

$$c_n = 5.98 D_{\text{eff}}^{-1/3}(h_n) C_N^2(h_n) dh / cos(z), \tag{2.13}$$

where λ is the wavelength of observation and $cos(z)$ is the inverse of the airmass.

2.3 Simulations for S-DIMM+

The S-DIMM+ method has primarily been used to estimate the C_N^2 profile using telescopes of apertures 1 m or more (Scharmer and van Werkhoven, 2010; Kellerer et al., 2012; Z. Wang et al., 2018). We developed our own simulations in Python (done at H-α wavelength, 656.3 nm) to test if the method can be used with our system and site parameters. Furthermore, it was also used to determine the optimal size of the sub-field used for correlation (ϕ), the number of sub-apertures to be used for the inversion, the number of temporal averages required and the best height grid for which our system can perform the inversion. We also verified its ability to successfully retrieve the given input turbulence strength profile.

The first step of the simulation was to produce a set of instantaneous SHWFS images that were shifted with respect to each other due to multi-layer atmospheric turbulence, similar to our experimental set-up. Therefore, each lenslet sub-aperture image contains 56×48 pixels with a sampling of $0.413''$/pixel to match the images we would get from the experimental set-up (details in Section 2.4.2). Figure 2.2 shows the simulation procedure diagrammatically.

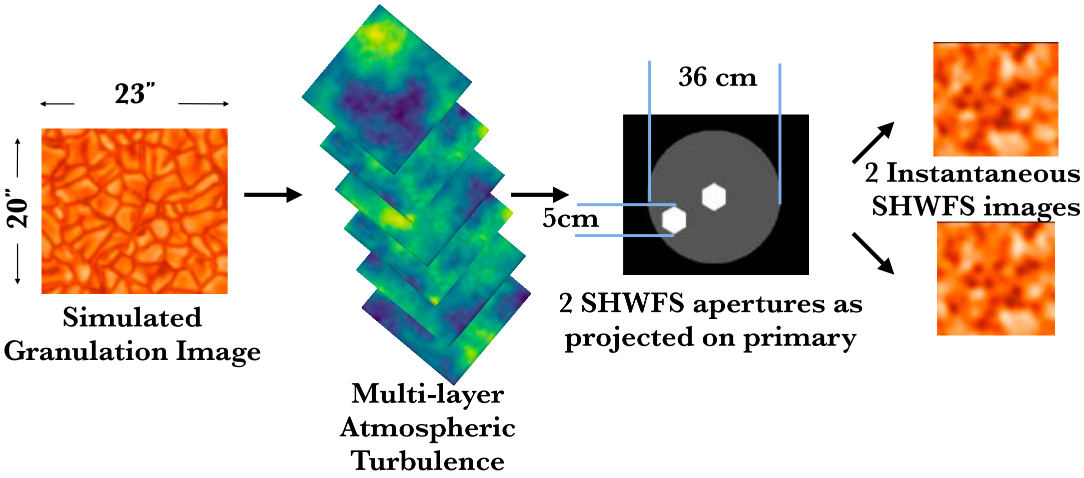

Figure 2.2: Diagrammatic representation of simulation workflow (images not scaled). From left to right are the simulated solar granulation used as "objects", followed by multi-layer atmospheric turbulence, a telescope with a lenslet array, and finally, two sets of instantaneous images produced by the SHWFS. The grey circle represents the masked KTT primary objective lens of 36 cm diameter. The small white hexagons indicate two lenslets projected back to the telescope pupil. The diagonal of the hexagons is about 5 cm.

The steps involved in simulating one frame of instantaneous SHWFS images were:

- Choosing an "object". We used simulated solar granulation images (courtesy Prof. S. P. Rajaguru of IIA, see Section 5.2.1) of about $23'' \times 20''$ to match the images we got from our experiment.
- Generating multiple phase screens that follow Kolmogorov's theory of atmospheric turbulence with the variation in projected pupil size with height accounted for.
- Determining the cumulative Optical Transfer Function (OTF) of each lenslet as the product of the OTFs of each individual layer by considering the portion of the phase screen that that lenslet would have sampled.
- Finding the instantaneous image formed each lenslet as the inverse Fourier transform of the product obtained by multiplying the cumulative OTF of each lenslet with the Fourier transform of the solar "object".

The process is repeated by sampling different regions of the phase screens to produce a series of frames similar to observations. One of the major assumptions of our simulations is that the PSF (at a given instant of time) for one sub-aperture is uniform across the field of view. This is not true in reality; the PSF is invariant only within the isoplanatic angle.

(a) **(b)**

Figure 2.3: Long exposure PSFs of one lenslet as the wavefront propagates through different layers of the atmosphere. (a) After passing through the layer at 4 km. (b) After passing through the layer at 3 km.

(a) **(b)**

Figure 2.4: Long exposure PSFs of one lenslet as the wavefront propagates through different layers of the atmosphere. (a) After passing through the layer at 2 km. (b) After passing through the layer at 1 km.

Figures 2.3, 2.4 and 2.5 are long exposure PSFs of one lenslet as the wavefront propagates through different layers of atmospheric turbulence. We can see the PSF widening (equivalent to blurring) as it encounters more layers of atmospheric turbulence. The layer heights for the different PSFs are given in the figure captions.

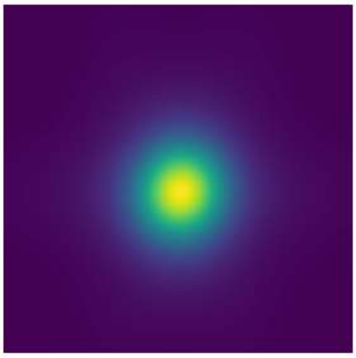

Figure 2.5: Long exposure PSF of one lenslet at the pupil plane after passing through 5 layers of atmospheric turbulence.

Furthermore, we highlight through our simulations that improper sampling of the phase screen leads to a systematic underestimation of r_0 or a failure of the inversion code. Due to the discrete nature of the simulation, there was an error in the generation of the hexagonal sub-pupil when not sampled properly. Therefore, it was always ensured that the error in the sub-pupil area was always less than 2%.

2.3.1 Results of simulations

The first test we performed using the simulations was to verify the underlying assumption of Equations 2.6 and 2.7. Consider a simple two-layer atmospheric model. The equations state that the total image motion due to the two layers is equivalent to the sum of the image motion induced by the two layers individually. We simulated a time series of 1000 data frames (using the steps detailed above) and estimated the total and the sum of individual image motions between sub-aperture images at each instant of time. This can be seen from the plots in Figure 2.6. Both plots show the sum of the image motions due to two individual layers versus the total image motion due to both layers. The values from the left plot were estimated by considering a small portion of the full sub-aperture image, i.e., $\phi \sim 13.2\times 13.2$ arc-seconds^2 (or 32×32 pixels), and the right plot was made by considering the full sub-aperture image for the image motion calculation. The correlation coefficients are inset within the respective plots. Here, since it is a simulation we know the exact image motion (sum of image motions due to each individual layer). Therefore, correlation can be considered as a measure of accuracy of estimating the image motion (total image motion). Ideally, the plot of the total and exact image motions must match giving rise to a straight line of slope = 1. However, due to the finite size of the window we are using for FCC, there is an inaccuracy in the estimated image motion. All points that lie away from the ideal line are due to the inaccurate total image motion value. They fall in distinctive lines due to the discreet minimum measurement of 1 pixel. While both cases have an acceptable accuracy (correlation coefficient > 0.8) when the total image motion is computed, the larger field is more accurate. Therefore, using a larger region (ϕ) to estimate the image motion is preferable.

So the question is, how large do we go? On the one hand, a larger ϕ is preferable since the image motion estimation is more accurate. This is crucial since, in the actual experiment, we can only estimate the total image motion due to all the layers. However, on the other hand, as seen in Equation 2.5, a smaller field increases the maximum height in the atmosphere up to which the system is sensitive. From the same equation, it can also be shown that a smaller field also increases the maximum separation between the two field regions (α_{max}). This decreases the minimum height at which the system is sensitive. The optimum value of ϕ will allow us to estimate the image motion (and subsequently the turbulence strength profile) accurately whilst having a good height resolution for the inversions. To estimate this optimum value, we considered more layers of atmospheric turbulence and repeated the image motion estimates. The trade-off between height sensitivity and accuracy was studied by varying the size of the sub-field chosen for analysis.

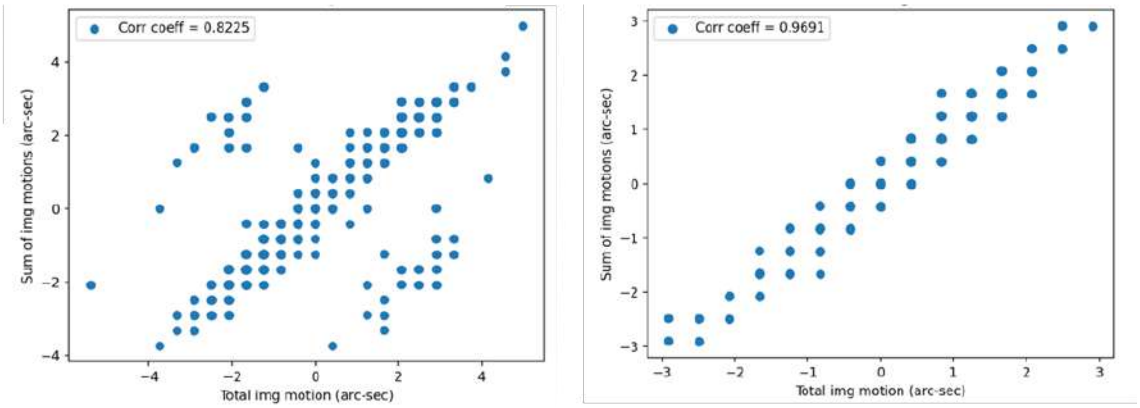

Figure 2.6: Plots of the sum of image motions due to two individual layers versus total image motion due to both layers. The left plot was made by considering $\phi \sim 13.2\times13.2$ arc-second^2 (a 32×32 window), and the right plot with a full sub-aperture image (20×20 arc-second^2). The correlation coefficients between the two sets of image motion calculations are inset in the respective plots.

The results of the image motion estimates for a four-layer atmospheric model are shown in Figure 2.7. The left and right plots use a 32×32 window and a 48×48 window, respectively to estimate the image motions. The correlation coefficient values are inset within the plots. We see again that the larger field (48×48 window) is more accurate in estimating the total image motion.

We found that using a $13.2''\times13.2''$ sub-field allowed at least 180 of every 200 frames to have accurate image motion measurements (the sum of individual image motions matched the cumulative image motion). So, we opted to use the same ϕ in our image motion estimates for further analysis. Additionally, this was set as a threshold to identify instances of poor seeing where the magnitude of image motion is very high, increasing the likelihood of underestimation. Therefore, for every batch of 200 frames, it was ensured that less than 10 % of the frames were "bad" with a bad frame being defined as one that returned image motion values within 6 pixels of the edge on any side. If more than 10 % of the frames were bad, then all 200 frames were rejected from the analysis (simulation and real data).

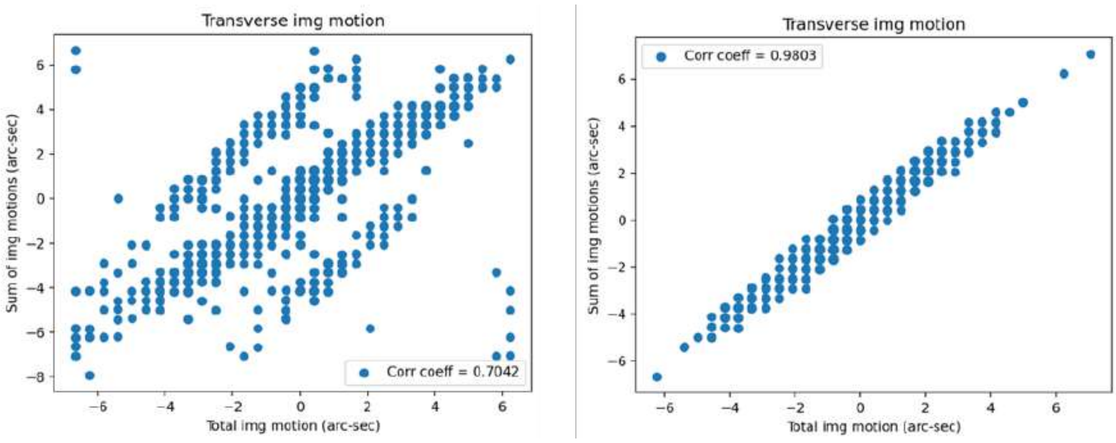

Figure 2.7: Plots of the sum of image motions due to two individual layers versus total image motion due to both layers. The left plot was made by considering $\phi \sim 13\times13$ arc-second^2 (a 32×32 window), and the right plot with $\phi \sim 19\times19$ arc-second^2 (a 48×48 window). The correlation coefficients between the two sets of image motion calculations are inset in the respective plots.

The first part of the simulation, as described above, produces only a series of instantaneous SHWFS images as we would get from the experiment. These are used to estimate the image motion values which will be used to form the two covariance matrices, $M_x(s,\alpha)$ and $M_y(s,\alpha)$ (Equations 2.8 and 2.9). Since $F_x(s,\alpha,h_n)$ and $F_y(s,\alpha,h_n)$ can be estimated using known system parameters (Equations 2.10 and 2.11), the c_n coefficients can be found using a linear least squares fit. Then, using Equations 2.12 or 2.13, the turbulence parameters can be estimated. The process of finding the turbulence parameters from the image motion estimates is called the "inversion procedure". We developed our own "inversion code" in Python for this use.

2.3.2 Inversion code

The inversion code uses the covariance of image motions from a sequence of instantaneous SHWFS images and inverts them to obtain the turbulence strength profile (Equations 2.8 and 2.9). The preliminary version of the code was reported in Subramanian and Rengaswamy (2023a). We then modified the code to better reflect the parameters of our actual experimental setup (Subramanian, Rengaswamy, et al., 2024). This helped us show that our inversion code was robust and was able to retrieve the given input parameters for a variety of system configurations. Hereafter, we will discuss only the modified code, as it is the same as the experimental setup that we used and better reflected the r_0 values we have observed at our site previously (Rengaswamy, 2016).

We first started with a simple single-layer model. The assumption here is that there is only one layer of atmospheric turbulence at a specific height (second column of Table 2.1). Phase screens generated according to the Kolmogorov theory of atmospheric turbulence (Rengaswamy, 2001; Unni. C et al., 2021) were generated at specific values of r_0 (third column of Table 2.1). Then, the inversion code was used, and the "measured" values of r_0 are summarized in the fourth column of Table 2.1. Here, we tested the number of covariance matrices that need to be ensemble-averaged before fitting for their c_n coefficients in Equations 2.8 and 2.9. Each frame of the SHWFS images produces one set of longitudinal and transverse covariance matrices. We found that averaging over 200 frames was sufficient to perform good inversions. Typically in solar high-resolution imaging, about 200 - 300 frames are used when ensemble averaging is required and our results are consistent with this. The errors associated with each inversion code output (column 4) are obtained by averaging the retrieved r_0 from multiple sets of 200 covariance matrices. As seen from the table, the input r_0 values were retrieved successfully (with acceptable errors) by the inversion code under different seeing conditions. This shows that the code is able to retrieve the input parameter satisfactorily for the simplest case. We can also notice that the errors associated with each inversion increases with height. This could be due to the decreasing sensitivity of the technique with height.

Table 2.1: Summary of inversion parameters for a single layer at different heights. The input and output r_0 values of the inversion code are in columns 3 and 4, respectively.

Case	**Layer heights (km)**	**Input r_0 (in cm)**	**Output r_0 (in cm)**
1	0	2	2.70 ± 0.05
2	0	5	5.80 ± 0.09
3	0	8	9.58 ± 0.16
4	1	5	4.67 ± 0.08
5	2	8	5.91 ± 0.08
6	2.5	8	5.55 ± 0.18
7	2.5	12	8.45 ± 0.13

We then increased the complexity by considering a two-layer model to represent the atmosphere. Table 2.2 shows some sample results from the different cases we tried. First, consider case 2. The retrieved r_0 values are inverted when compared to the input. This is because the

S-DIMM+ method fails at strong seeing conditions. The original work by Scharmer and van Werkhoven (2010), identified that inversions failed at poor seeing (< 75% of sub-aperture diameter). We verified this with our system parameters. Our sub-aperture diameter is 5 cm. We found that for multi-layer models when the r_0 was lesser than 3.75 cm, inversions failed.

Table 2.2: Summary of inversion parameters for a two-layer atmospheric model. The inputs are the heights (column 2) and r_0 values (column 3) of the layers. The output is the retrieved r_0 values (column 4).

Case	**Layer heights (km)**	**Input r_0 (in cm)**	**Output r_0 (in cm)**
1	0, 1	5, 5	4.02 ± 0.10, 6.96 ± 0.61
2	0, 1	2, 5	5.51 ± 0.33, 2.06 ± 0.21
3	0, 1	5, 2	5.03 ± 0.66, 2.81 ± 0.18
4	0, 1	4, 5	3.79 ± 0.10, 6.05 ± 0.71
5	0, 1.5	4, 8	4.22 ± 0.03, 9.04 ± 1.35
6	0, 2	4, 8	4.33 ± 0.06, 9.07 ± 0.86
7	0, 2	5, 9	5.18 ± 0.12, 10.99 ± 0.97
8	0, 2.5	5, 9	5.31 ± 0.04, 11.37 ± 1.97
9	0, 2.5	5, 16	5.81 ± 0.06, 14.53 ± 2.69

Finally, we opted for a six-layer model. We have used 12 unique values of angular separations (α) from 0 to about $9''$ in steps of about $0.8''$. For our system parameters, the minimum and maximum heights are 0 km (pupil of the telescope) and 6 km, respectively. We also found that a height grid with layers roughly 0, 1, 2, 3, 4, and 6 km above the ground gave good inversions (able to detect and identify the presence of a strong layer of turbulence). It must be noted that the "ground layer" in the S-DIMM+ procedure is the height of the primary mirror, which is at 2345 m above sea level, and it will be referred to as GL-(S-DIMM+).

We tested for different turbulence conditions in the six-layer model. Figure 2.8 shows two cases. The first case (blue curves with circular markers) has an ideal profile with turbulence decreasing with height. The second profile (orange curves with triangular markers) has one strong turbulence layer at 3000 m. For both cases, the input and output profiles are shown by solid and dashed curves, respectively. An ensemble average of 200 matrices is done prior to fitting the theoretical covariance functions. The error bars in the output curves arise from averaging the results over multiple such sets of 200 matrices. The inversion is able to detect the given trends, albeit not the exact input turbulence strengths. This trade-off is acceptable since we are interested in identifying the height of the strong layer of turbulence and not in measuring the exact strength of that layer. It can be seen that the strengths at 6000 m layer are consistently underestimated. The underestimation of the turbulence at higher heights is an intrinsic limitation of the S-DIMM+

method. While the code underestimates the turbulence from higher heights, it is still able to identify the strongest turbulence layer, which is the primary aim of this experiment.

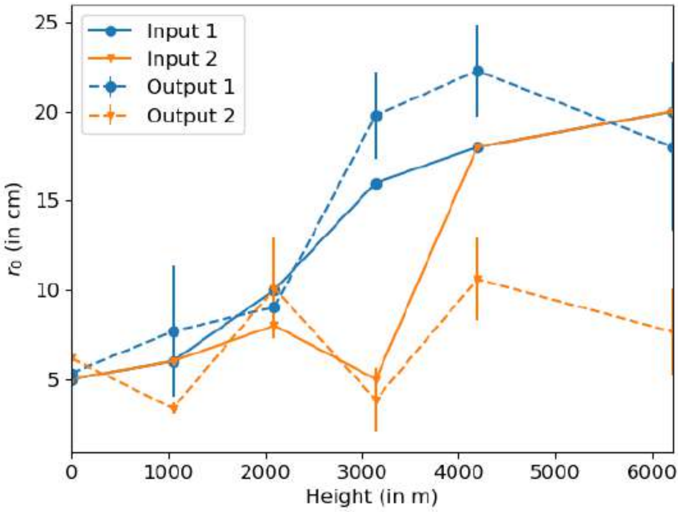

Figure 2.8: Results of the inversion (from simulation) are shown. The solid profiles show the vertical distribution of r_0 that was considered as input in the simulation code for generating multi-layer turbulence. The dashed profiles are the retrieved parameters from the inversion code. The two colours or markers represent two different sets of inputs and corresponding outputs.

Further we found that found that using only the sub-aperture images along the diameter of the telescope is sufficient for the inversions. This is because that row of images covers all the possible combinations of separation values (s) and the image motion estimates from other sub-aperture images are required only when to improve the SNR. A similar finding was also reported in Kellerer et al. (2012).

2.4 Experimental set-up

We conducted near-simultaneous measurements with the balloon measurements and the S-DIMM+ method at KO in January 2024. The experimental set-ups are explained below.

2.4.1 Balloon-Measurement set-up

We have used latex balloons filled with hydrogen. The balloons were procured from Pawan Balloon (Pune, India). The hydrogen gas (99.99%) was procured from Sri Venkateshwara Carbonic

Gases Pvt Ltd (Coimbatore, India). The volume of hydrogen gas required for a payload of about 3.2 kg was 4.7 m^3 (Nayak et al., 2013; Safonova et al., 2016). Photographs of the balloon taken during the experiment are shown in Figure 2.9. The payload consists of two parts, an IP65 waterproof plastic enclosure (Figure 2.12 (b)) housing all the electronics components and a rod mounted with seven immersion-type Pt-100 sensors (marked in Figure 2.9 (b)). The IP65 enclosure was kept in a Styrofoam box during the balloon flight.

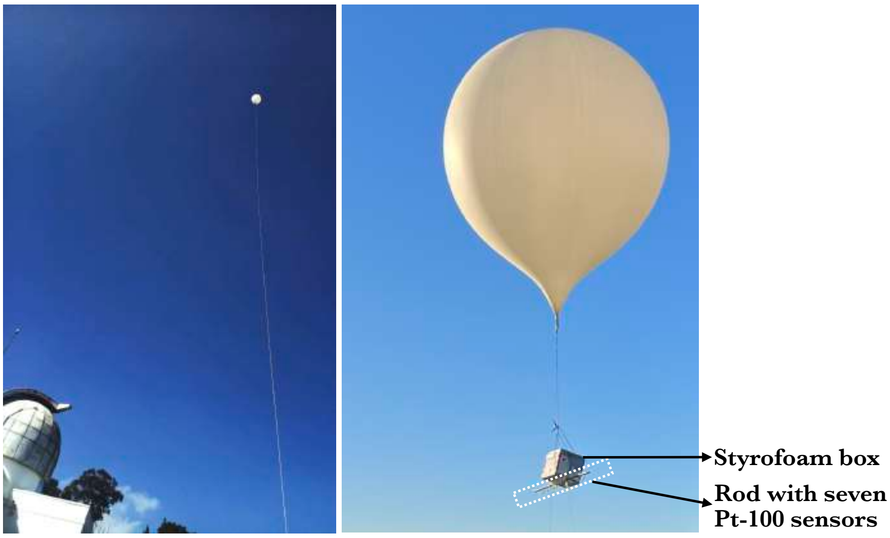

(a) (b)

Figure 2.9: Photographs of the tethered balloon during measurements. (a) Balloon-measurements setup with the dome of KTT on the bottom left. (b) Zoomed picture of the setup. A white dotted box marks the rod with Pt-100 sensors mounted. A thermally insulated Styrofoam box houses the electronics.

2.4.1.1 Data logger electronics

The electronics setup involves a custom-built microcontroller-based data logger called IIA Data Logger (IDL). At its heart is the ATmega 328 Arduino Nano microcontroller, which receives sensor readings from an Analog to Digital Converter (ADC - ADS1115) and timing information from a Real Time Clock (RTC - DS3231). It saves the collected sensor data along with the time stamp onto the SD Card. A set of eight immersion-type Pt-100 temperature sensors connected in resistance divider mode with eight precision resistances (5K Ohm) are used. Only seven of these sensors were used during the actual experiment as one was kept as backup to be used in case one of the other sensors failed. The voltage across the Pt-100 is measured using 16bit ADC

(ADS1115) with an input range configured to +/-0.256 V using an internal Programmable Gain Amplifier (PGA). All the sensors are sampled using the same ADC one after the other. The sensor to be sampled is selected by using an analog multiplexer (CD74HC4067) controlled by the microcontroller. The various components and their interactions are shown as a block diagram in Figure 2.10.

Each measurement happens in a burst mode every 1 sec, with 10 sets of measurements of all the 8 sensors. The time required for sampling data from all eight sensors is 80 ms, with 10 ms between each sensor reading. Since this is a field experiment, provision of an LED indicator is given to indicate data is being recorded. Additionally, Bluetooth connection allows users to connect with the microcontroller and receive present data with a time stamp for sensor functionality check. The entire system works with a 7.4 V, 2200 mAh Lithium Polymer battery pack and can last up to several hours of operation.

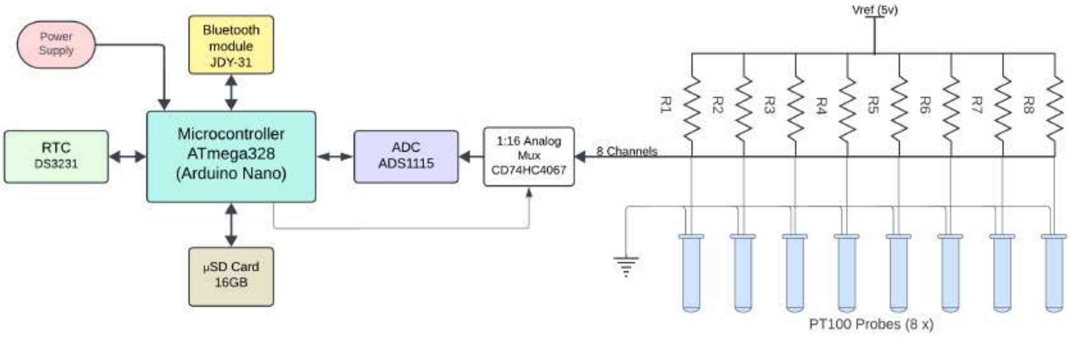

Figure 2.10: Block diagram of the electronic components of IDL. Image courtesy: Dr. Prasanna Gajanan Deshmukh (IIA).

2.4.1.2 Calibration

In the actual experiment, the IDL records only the ADC counts. We need to map it back to the temperature sensed by each sensor. This is done via calibration. The photographs shown in Figure 2.12 were taken during the calibration, which was done in two stages. First, resistance with a known value was connected to the circuit in the place of the Pt-100 sensor, and the counts were recorded for a few seconds. This was repeated with different resistances. As stated before, each second records 10 values of resistance data. This is averaged to get a single value of ADC counts.

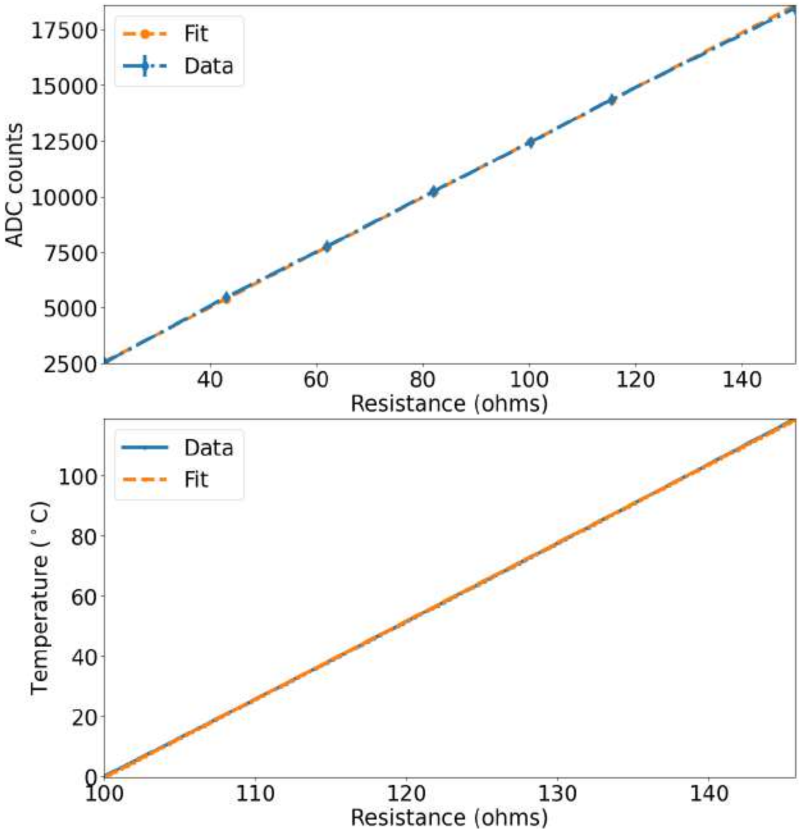

Figure 2.11: Calibration curves for balloon-measurements. Top curve shows ADC Counts vs resistance (Ω) and the bottom curve shows temperature (°C) vs resistance (Ω).

The standard deviation of the 10 points is also calculated. If the standard deviation is more than 10 counts, these points are considered outliers and removed. Then, a straight line was fit to convert ADC counts to resistances. This is shown in the top curve of Figure 2.11. The solid blue curve is from the data recorded. The error bars arise from averaging the data counts recorded over a few seconds. The magnitude of the error bars is much smaller than the actual values of the counts. The dashed orange curve is the straight line fit (described by the following equation):

$$\text{ADC counts} = 123.17 \times \text{Resistance}(\Omega) + 100.87. \tag{2.14}$$

Then, the resistances were converted to temperature values using the standard table (European Standard of Pt-100 Temperature vs Resistance Table). This is shown in the bottom curve of Figure 2.11. The straight-line fit for this is given by the equation:

$$\text{Temperature}(^\circ\text{C}) = 2.60 \times \text{Resistance}(\Omega) - 260.77 \tag{2.15}$$

We first verified if the Pt-100 performance was as per the specification by measuring the sensor's resistance at the ice point and boiling point of water. At ice point (0°C), the Pt-100 must have 100 Ω resistance. This can also be seen from Equation 2.15, which satisfies this condition. These tests act as verification of our calibration procedure.

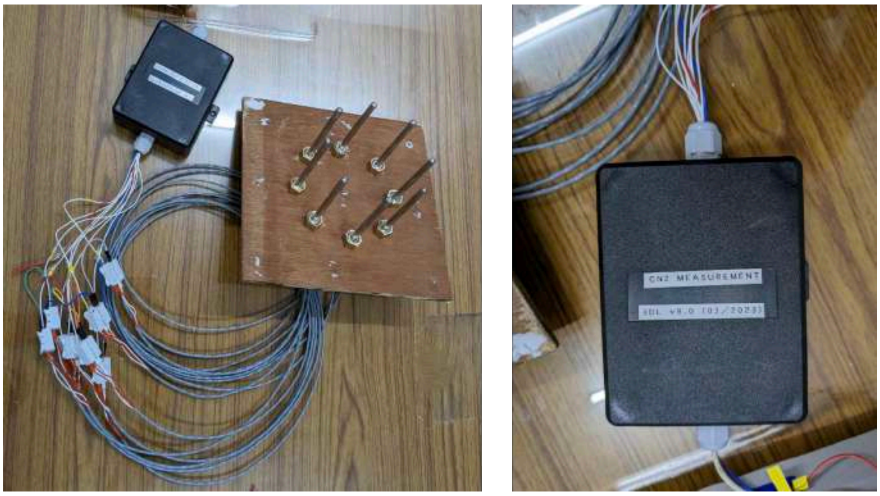

(a) (b)

Figure 2.12: Pictures of the balloon-measurements set-up taken during calibration. (a) The immersion-type Pt-100 temperature sensors were mounted on a wooden block in a circular fashion for convenience during calibration when they were immersed in ice/boiling water. (b) Photograph of IP65 enclosure enclosing the electronics used for this experiment. Image courtesy: Dr. Prasanna Gajanan Deshmukh (IIA).

2.4.2 S-DIMM+ set-up

At the focal plane of KTT (dotted line in Figure 1.10), we used a field stop to select a region of about 23×20 arc-seconds^2. Reimaging optics were used to reduce the beam diameter and fully illuminate eight lenslets across the diameter with an image scale of about 0.4″/pixel on the detector plane. Data was recorded using two wavelength filters - one at H-α (centered at 656.3 nm with 3.5 nm bandwidth) and one continuum filter (centered at 540 nm with 10 nm bandwidth). Additionally, a polariser-analyser combination was used to control the intensity of the incident light. Finally, an OKO Tech SHWFS (serial number: FS1540-H300-F18-16.04)[1] mounted with a

---

[1] WFS technical passport

uEye camera (IDS UI-1540LE-M-GL66) was used to record the lenslet array images.

Table 2.3: Observation set-up parameters for S-DIMM+

Parameter	Value
Telescope Primary Diameter	36 cm
Focal length	36 m
Wavelength(s) of observation	656.3 nm and 540 nm
Focal length of collimating lens	250 mm
Pitch of SHWFS	300 μm
Pitch of SHWFS projected on pupil	$\sim$ 4.5 cm
Diagonal of the hexagon as projected on the pupil	$\sim$ 5 cm
Number of lenslets across Dia	$\sim$ 8
Focal length of lenslet array	18 mm
Pixel size	5.2 μm
Full well capactiy	40000 e^-
Image scale	0.413 $''$/pixel
Field-size of one sub-aperture image	$23'' \times 20''$
Frame rate	79 fps
Exposure time	1 ms

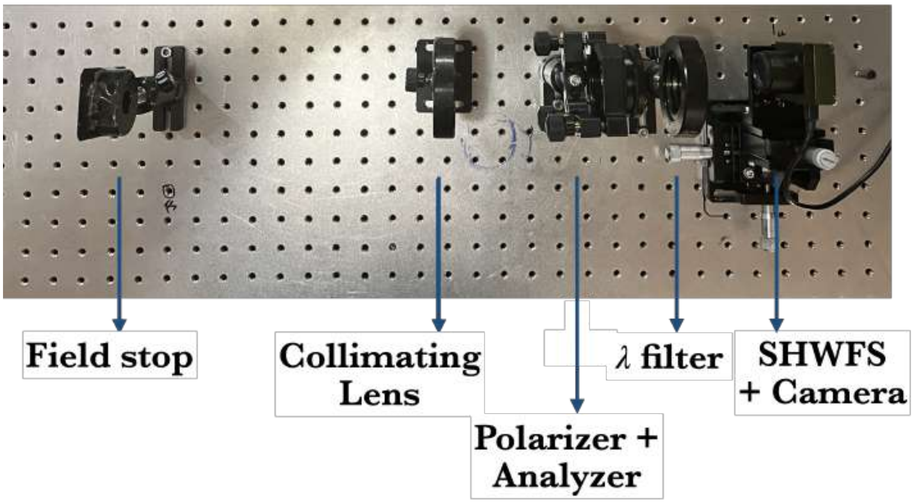

Figure 2.13: Optical setup at the telescope focal plane for S-DIMM+ measurements.

2.5 Data and Analysis

The turbulence profiling experiments with the two instruments were done on the 16th, 17th and 18th of January, 2024. They were done near-simultaneously with the balloon as close to the dome of KTT as possible. Figure 2.9 (a) shows this.

2.5.1 Balloon-measurements

Three data sets were recorded on the 17th of January 2024. The first set started at about 5:10 UT (10:40 AM local time) and lasted about an hour. The balloon's initial height was 10 m, and its final height was 180 m. The second set started immediately after the first set at about 6:00 UT. This also lasted for about an hour, and data was recorded from 180 m to 10 m (in the descent phase). The third set started around 8:45 UT (after local meridian transit) and lasted almost two hours. The balloon reached a maximum height of 350 m. These three sets will be referred to as sets 1, 2, and 3, respectively.

For the profile measurement experiments, the seven Pt-100 sensors were mounted on a flat rod about 1.3 m long. This allows 21 possible combinations of baselines when the sensors are chosen two at a time. There were eleven unique baselines from 10 cm to 110 cm in steps of 10 cm. Two holes were made at the ends of the rod to allow a Nylon rope to tie it to the balloon. Additionally, another rope with markings every 10 m was used to hold and hoist the balloon. The duration to move between heights (separated by 10 m) was about 20 s. Then, an additional 1 min 40 s was allowed for the medium to settle down. It was maintained at a given height for one minute. Therefore, for each height, around 600 points of data were recorded by each of the seven sensors. There is roughly a 10 m offset between the "ground level" of the balloon-measurements and that of S-DIMM+ (GL-(S-DIMM+)).

The analysis procedure was as follows:

- For each height, the counts recorded by each sensor were collected.
- Using the calibration method described in Section 2.4.1.2, the temperature recorded by each sensor was calculated.
- The bias offset (ensemble averaged mean) of each sensor was removed.
- Using two sensors at a time, the temperature structure function was found as the mean square difference of the temperature fluctuations between the points.
- C_T^2 and then C_N^2 were found using Equations 2.3 and 2.4 respectively. By using Equation 2.3, we are assuming a Kolmogorov model of atmospheric turbulence. For substituting in Equation 2.4, the pressure (in millibar) at a given height (h) above the ground can be

expressed as Lide and Frederikse (1996):

$$P(h) = \left(\frac{44331.514 - h}{11880.516} \right)^{\frac{1}{0.1902632}}. \tag{2.16}$$

The above process is repeated for the twenty-one possible combinations of two sensors. The C_N^2 profiles obtained from each are averaged to get the cumulative profile. An important point is that there is a finite time delay between the measurements made by the different sensors. The delay is a function of the two sensors chosen. This is a consequence of opting for a simpler setup to ease the calibration procedure by using a single ADC for all the sensors.

2.5.2 S-DIMM+

We recorded bursts of data, each containing 2000 frames with an exposure time of about 1 ms. We have observed different active solar features (sunspots or pores) for our analysis. Two such frames are shown in Figures 2.14 and 2.15. Both of these were observed with the same optical set-up at 540 nm with 1 ms exposure time. Figure 2.14 was taken on 18th January around 5:30 UT (closer to local noon) and Figure 2.15 was taken on 18th January around 2:30 UT. The first difference between the two images is the number of sub-aperture images (due to the number of illuminated lenslets) despite being taken with the same setup. This is because the observations were taken in January when the declination of the Sun was around -21° (very close to the extreme southern limit).[2] Despite moving the primary mirror to the edge of the mount, it was not fully illuminated until the zenith angle of the Sun was sufficiently high. The SHWFS is at the re-imaged pupil plane and we see the effect of partial illumination of the primary mirror here as well. Figure 2.14 shows the images from all the sub-apertures as expected with a fully illuminated primary mirror. Another point that can be noticed is the quality of the images. At a mountain site like Kodaikanal, it is expected that the seeing degrades as a function of day due to ground heating (Figure 1 of Brandt (1969) shows diurnal variation of seeing at a mountain site using visual estimate of image quality). We can see from the two SHWFS frames that the early morning images are much sharper than the ones taken closer to local noon.

The data analysis procedure was as follows:

- Each recorded image frame contains fifty sub-images corresponding to the fifty fully illuminated lenslets. Out of these, only the eight across the diameter, along with one other image (identified as the one with the highest contrast, called reference image), are used for the analysis.

---

[2] Declination calculated by providing relevant information at https://gml.noaa.gov/grad/solcalc/azel.html
Latitude: 10.2391° North, Longitude: 77.4977° East
Offset to UTC: 5.5 hours (no daylight savings time),
Dates: 16, 17 and 18 January 2024,
Time: 08:00 AM IST and 11:15 AM IST

- The regions where these nine images lie are identified. Each sub-image occupies 56x48 pixels. The corresponding regions of the flat and dark images are used for calibration.
- The covariance matrices are estimated as described in section 2.2.2 using two sub-aperture images and two sub-fields within them at a time.[3]
- 200 covariance matrices were ensemble averaged and then fitted to the theoretical equations to estimate the strength of turbulence.

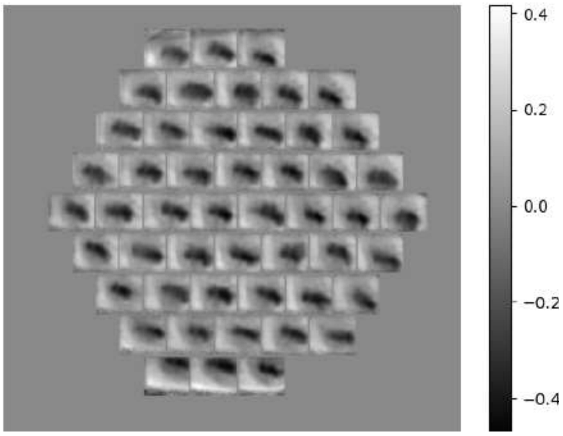

Figure 2.14: One frame containing the images of a sunspot as recorded by lenslet array at 540 nm (exposure time $\sim$ 1 ms). Each sub-image has a field of view of about 23×20 arc-second^2. Standard image processing steps of dark and flat correction have been done. The images are also made zero mean.

---

[3] NOTE: Here, we are using a third image (chosen as the sub-aperture image having the highest contrast within that frame) as reference image to estimate the *differential* image motion. For example, δ_{x1} is the difference of the image motion obtained using reference image and sub-aperture image 1 and that obtained using reference image and sub-aperture image 2. The first advantage of this is the elimination of the effect of other sources like telescope vibrations on the image motion estimation. Ideally, the image motion estimated directly between the two sub-aperture images should be equal to the difference in the image motion estimated when the sub-aperture images are compared with a reference image. Using our simulations we found that using the reference image is better particularly when the reference image is between the two sub-apertures and when the magnitude of image motion is large. This is because the maximum image motion that can be estimated using FCC is half the window size and using the differential method allows us to calculate values that might lie beyond the measurement limit when the two images are directly considered.

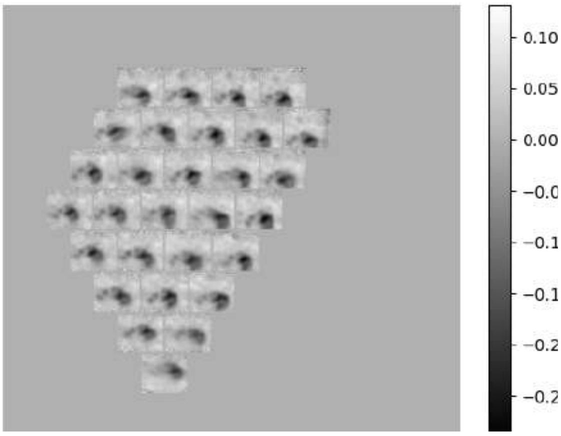

Figure 2.15: One frame of SHWFS images recorded early morning (around 2:30 UT). Field of view of each lenslet image, exposure time and wavelength of observation same as Figure 2.14.

2.6 Results and discussions

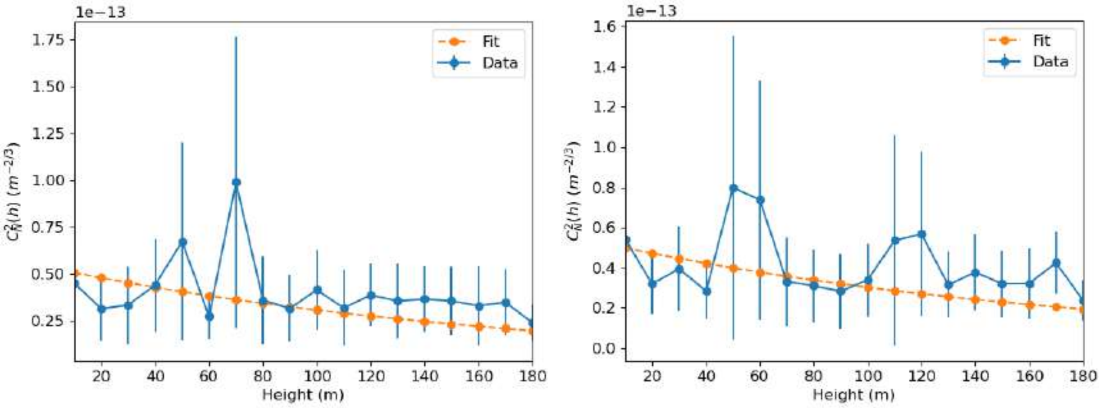

(a) (b)

Figure 2.16: Results from the balloon experiment taken on 17th before local meridian transit. (a) From data set 1 (ascent phase) and (b) set 2 (descent phase). The solid blue curves in the two plots are from the values calculated from the experiment, and the dashed orange curves are from the fit of the daytime component. For the fits shown here, $\frac{V_w}{V_w}$ = 3 and h_0 = 180 m were used.

The results of the near-Earth turbulence and the higher-altitude turbulence measured at KO are given below.

2.6.1 Near-Earth turbulence

As mentioned in Section 2.5.1, three sets of data 1, 2, and 3 were recorded. There was very minimal wind while recording data set 3 and the rope holding the balloon was almost vertical. The temperature structure functions ($D_T(r)$) for the three data sets were calculated. The results are given in Appendix C. Then, the C_N^2 profiles were calculated using the steps in Section 2.5.1 and the results are shown by solid blue curves in Figure 2.16 (a), (b), and Figure 2.17 respectively.

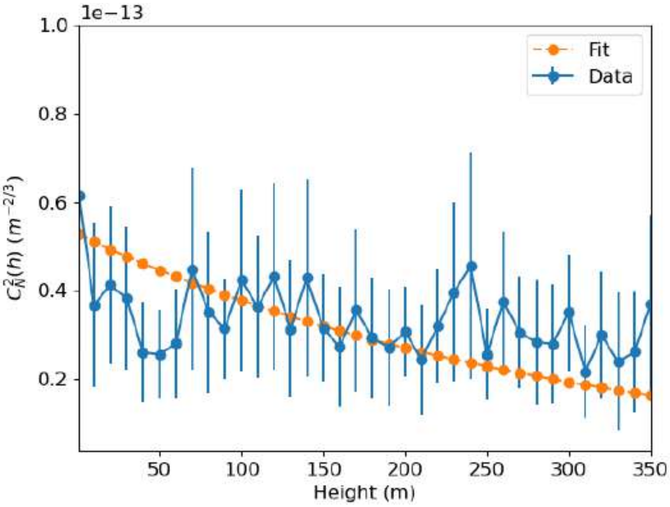

Figure 2.17: Results from the balloon experiment taken on 17th after local meridian transit. The color (or style) of the curves are the same as those in Figure 2.16. For the fit shown here, $\frac{V_w}{V_w} = 3$ and $h_0 = 300$.

We initially fitted the three data sets for the model given by Equations 1.6 and 1.7. Following that, since the balloon has a maximum measurement height of 350 m, we fitted only for the daytime component described by the second term of Equation 1.7. In both cases, we assumed different wind speed ratios $\left(\frac{V_w}{V_w}\right)$ and boundary scale heights (h_0) We would need to carry out more experiments with the balloon (or other equipment) going to larger heights to better understand and constrain the scale height. We found that fitting only for the daytime component did not significantly change the results compared to the fitting for the full model (see Appendix D). This shows that the daytime component dominates in near-Earth turbulence. The term A_B was used as a parameter for the fit. The integral of the C_N^2 profile gives the integrated r_0.

Table 2.4: Results from balloon-measurements for data set 1. The measured data was fitted to the daytime contribution model (Equation 1.7 second term). The results of the fit for different combinations of wind velocity ratios and boundary scale height (first and second columns, respectively) are shown below. The fitted values of A_B are shown in the third column. The r_0 (at 500 nm) estimated from the fit at finer sampling are given in the last column. r_0 estimated using measured profile from data set 1 was 38.79 cm (at 500 nm).

$\frac{V_w}{\overline{V_w}}$	h_0 **(m)**	A_B	r_0 **(cm) - from fit 20 cm sampling**
0.3	100	6.47e-14	4.76
3	100	6.47e-14	4.76
0.3	180	5.34e-14	4.35
3	180	5.33e-14	4.35

Table 2.5: Results from balloon-measurements for data set 2. The column headers are the same as Table 2.4. r_0 estimated using measured profile from data set 2 was 38.21 cm (at 500 nm).

$\frac{V_w}{\overline{V_w}}$	h_0 **(m)**	A_B	r_0 **(cm) - from fit 20 cm sampling**
0.3	100	6.42e-14	4.85
3	100	6.42e-14	4.85
0.3	180	5.27e-14	4.48
3	180	5.27e-14	4.48

The results of the fit are shown graphically in Figures 2.16 (a), (b) and Figure 2.17 as dashed orange curves. It can be seen from these figures that the experiment is able to detect the overall trend predicted by the daytime component. The assumed exponential fit is consistent with the data within the error bars, though visually it may not appear to be the best fit. Once the parameter A_B was estimated for each curve, it was used to generate a model atmosphere at finer sampling (every 20 cm). The r_0 is estimated with the C_N^2 profile modeled using a finer sampling. An earlier study at the observatory used image motions and estimated the median r_0 to be about 3.9 cm at 500 nm (Rengaswamy (2016)). We find that our r_0 estimates, when measured from a fine sampled C_N^2 profile, match with the earlier results well. These results for the three data sets are shown in Tables 2.4, 2.5, and 2.6, respectively. From the tables, it can be seen that for a given data set, varying the wind velocity ratio and boundary scale height does not significantly change the results of the fit. However, we did note that a boundary scale height (h_0) of 300 m gave a better fit for data set 3 compared to the other two sets having a good fit for a h_0 of 180 m. We need to repeat the experiment to understand if this is due to the diurnal variation.

Table 2.6: Results from balloon-measurements for data set 3. The column headers are the same as 2.4. r_0 estimated using measured profile from data set 3 was 28.49 cm (at 500 nm).

$\frac{V_w}{\overline{V_w}}$	h_0 **(m)**	A_B	r_0 **(cm) - from fit 20 cm sampling**
0.3	180	6.12e-17	3.17
3	180	6.12e-17	3.17
0.3	300	5.28e-14	2.91
3	300	5.28e-14	2.91

2.6.2 High-altitude turbulence

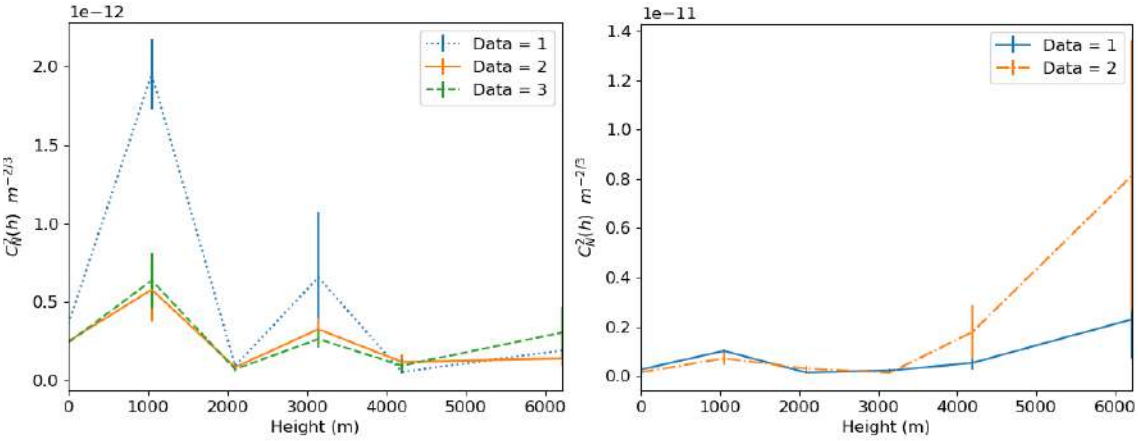

(a) (b)

Figure 2.18: Results from the S-DIMM+ inversion. (a) Results from three sets of data taken before zenith. (b) Results from two sets of data taken after zenith. The profiles are not airmass corrected.

Figure 2.18 (a) and (b) show the results obtained from the S-DIMM+ method pre and post-local noon, respectively. In the former, the dotted blue and solid orange curves (Data 1 and 2) are obtained from data recorded at 656.3 nm, and the dashed green curve using data recorded at 540 nm (Data 3). Data set 1 was observed on 16th January, 2024 at about 6:45 UT. Data set 2 and 3 were recorded on the 18th of January, 2024 at about 6:45 UT and 5:30 UT, respectively.

Similarly, in the post-noon curves, the solid blue curve was estimated with data recorded at 656.3 nm, and the dashed orange one used data taken at 540 nm. The former data set was observed on the 17th of January, 2024 at about 8:50 UT and the latter on 18th of January, 2024 at about 7:15 UT. In both the pre- and post-noon cases, each data set corresponds to four bursts of 2000 frames each. The time gap between two bursts (within one data set) was about $3 - 5$ min. The error bars arise from averaging over the inversion results from the four bursts of data in each data set. From the figures, it can be seen that our inversion code is not wavelength-dependent.

Before noon, we identified the presence of a strong turbulence layer at about 3 km above the telescope. Another strong layer at roughly 1 km above the telescope can also be seen. But, as stated in Section 2.3.2, our inversion code was over-estimating the turbulence at this height. Therefore, the detected turbulence at 1 km may be due to a systematic from the code or due to an actual strong layer at that height. We cannot rule out either of these possibilities. We also saw the evolution of turbulence during the day, with the seeing worsening with time. This is expected for a mountain site like Kodaikanal, as the ground heats up as the day progresses. We could observe this effect visually as the degradation in the quality of the SHWFS images (Figures 2.14 and 2.15). This can also be seen in Figure 2.18 (b), which shows that the turbulence has increased by an order of magnitude compared to the pre-noon profile. The error bars associated with this profile are also higher as the inversion is known to fail under poor seeing conditions (Scharmer and van Werkhoven, 2010).

Chapter 3

Deconvolution as a probe of the atmosphere

> *"Astronomy is much more fun when you are not an astronomer."*
> *Brian May (Fireworks In A Dark Universe)*

The work presented in this chapter has been reported in the following publication:

Measurement of isoplanatic angle and turbulence strength profile from H-alpha images of the Sun **Saraswathi Kalyani Subramanian**, Sridharan Rengaswamy, 2023, *Adaptive Optics for Extremely Large Telescopes (AO4ELT7)*, 22.

3.1 Introduction

In image processing, deconvolution is employed to improve the contrast by removing the response of the optical system from the image (Starck, Pantin, and Murtagh, 2002). From Figure 1.7, we can see that the transfer functions of ideal diffraction-limited telescopes (blue curves) decrease as a function of spatial frequency. This shows that the contrast of the image reduces at higher spatial frequencies even under ideal imaging conditions. By removing the response of the system from the image, ideally, we will obtain uniform system response (equivalently restoring the original contrast of the object) across all spatial frequencies. A simulated example of this is shown in Figure 3.1. From left to right, we have (a) the "true object", (b) the image formed by an ideal diffraction-limited 20 cm telescope and (c) the deconvolved image. Here, the "true object" is a simulated solar granulation image (courtesy Prof. S. P. Rajaguru of IIA, see Section 5.2.1). We can see that even under ideal conditions, there is a loss of contrast between images (a) and (b). When we remove the system's response (here, we compute the inverse Fourier transform of the division of the Fourier transform of the object by the OTF of the telescope), we can retrieve the "true object". It must be kept in mind that the example shown here is very idealistic. No noise has been considered, and the OTF of the system is known exactly. In reality, retrieving the "true object" perfectly is very difficult. However, we will see an improvement in contrast post-deconvolution. Therefore, astronomers primarily use deconvolution to remove the effect of the instrument and improve the image quality.

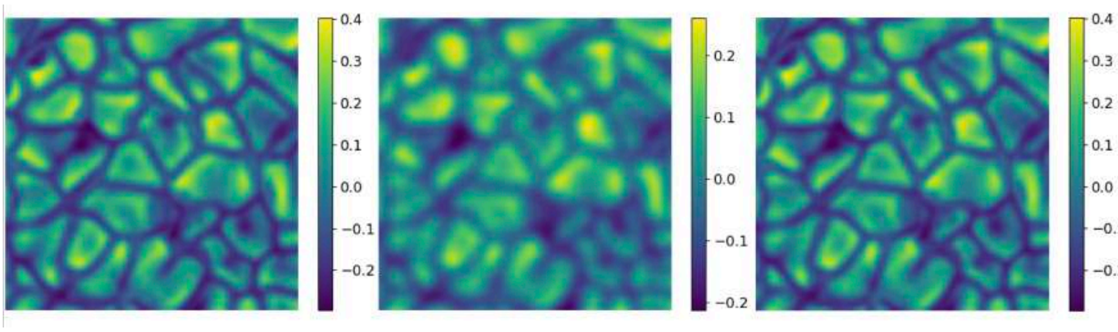

(a) (b) (c)

Figure 3.1: Simulated example to illustrate the use of deconvolution. (a) Solar "object" which is simulated granulations with a field of view of $27'' \times 27''$. (b) The image formed by an ideal diffraction-limited 20 cm telescope (at 656.3 nm). (c) Image post deconvolution with the ideal OTF.

Deconvolution can be applied to seeing-limited images or AO-corrected images. AO systems can only partially compensate for the turbulence. Therefore, post-processing techniques using deconvolution are often employed to enhance the contrast further. Refer to Löfdahl, van Noort, and Denker (2007) (and references therein) for commonly used image restoration techniques for solar images. In the case of images acquired with ground-based telescopes, we know that they contain an imprint of the atmosphere. This can be used to study the properties of the atmosphere (Brandt, 1970; O. von der Lühe, 1984; Sridharan, Dashora, and Venkatakrishnan, 2004; Rengaswamy, Ravindra, and Prabhu, 2019; Unni. C et al., 2021). In Section 3.2 we briefly recap the deconvolution procedure that can be used on long-exposure seeing-limited images of the Sun to estimate the r_0 at a site. This part of the study has already been reported in Rengaswamy, Ravindra, and Prabhu (2019) and Unni. C et al. (2021). In this thesis, we wanted to exploit the extended nature of the Sun to extract other parameters of the turbulence. The Sun, having an angular diameter of 0.5°, is a unique extended source. The only night time object that can perhaps be compared is the Moon. However, the angular size of the Moon also changes with its phases. Extended sources are continuous distributions of point sources. Using that to our advantage, we can infer information about the turbulence at different directions in the atmosphere[1]. We also know that the isoplanatic angle is a measure of the decorrelation of the perturbations encountered by the wavefronts along different directions. Therefore, we have used deconvolution on seeing-limited solar images to estimate the isoplanatic patch during the daytime (defined for long-exposure images). The procedure is explained in Section 3.3. Finally, we discuss our results in Section 3.4.

3.2 Parametric Search Method

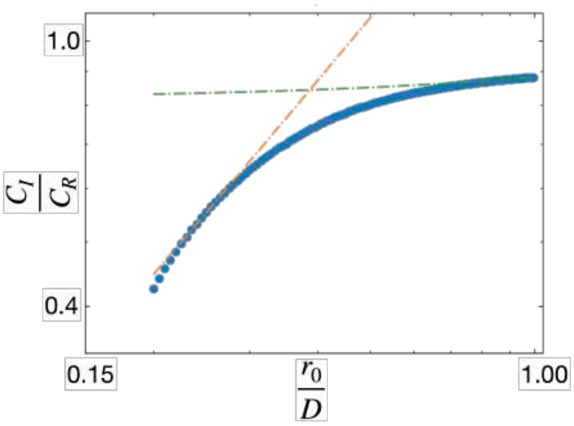

Figure 3.2: Log-log plot of contrast ratio as a function of r_0/D (blue cure). The dashed green and orange lines are the straight lines fit to the ends of the blue curve.

The Parametric Search Method (PSM) (Rengaswamy, Ravindra, and Prabhu, 2019; Unni. C et al., 2021) is used to estimate the r_0 by deconvolving the long-exposure seeing-limited images. The steps can be summarized as:

- A segment of long-exposure seeing-limited image of size N×N is chosen. Normal image processing steps of flat and dark correction are done.
- A box mean is applied to the segmented image to reduce the noise and obtain a “smooth image” and estimate the noise. Then, this is subtracted from the original image.

---

[1] As mentioned in Section 1.3.3, GLAO and MCAO utilize multiple point sources in the field to analyze the turbulence volume and then perform AO correction. In the case of an extended source, we can consider the different regions of the object as different sources in the sky; the wavefronts emitted by them sample different volumes of the turbulent atmosphere.

- The noise-removed image is made zero mean. Then, the contrast is estimated as the standard deviation of the intensity values (refer to Equation 5.1). This is the initial contrast of the image (C_I).

- The original segmented image (before noise-removal) is multiplied with a Hanning window of N×N. This is done to reduce the ringing effect in the Fourier domain. Then, the Fourier transform of the segmented image is calculated.

- The power spectrum of the original cropped image is found as the modulus square of the Fourier transform. The noise is estimated as the mean of the signal beyond the diffraction limit.

- The Wiener filter defined by

$$W(q) = \frac{S(q)}{(S(q) * S(q)) + N/[P(q) - N]}, \tag{3.1}$$

  is estimated. $S(q)$ is the seeing-limited long-exposure transfer function (Equation 1.9). The term $N/[P(q) - N]$ is the ratio of the noise-to-signal power spectrum.

- The restored image is found as the inverse Fourier transform of the product of $W(q)$ and the Fourier transform of the segmented image. The restored image is divided by the Hanning window.

- The contrast of the restored image is found (C_R). The ratio of the contrast of the original image to that of the restored image is found (C_I/C_R).

The above steps are repeated for different OTFs generated with different values of r_0. A plot of the contrast ratios as a function of r_0/D is generated as shown in Figure 3.2. Two straight lines are fit to the extremes of the curve (orange and green dashed lines). The x-coordinate of the point of intersection of the two lines is an estimate of the r_0 ('D' is known). This can be repeated for different segments within an image and for different images acquired throughout the day to understand the diurnal variation of r_0. It is a good method to estimate the r_0 at a site, and it exploits the data from small solar telescopes, which are standard at most observatories.

The PSM has been applied to the data recorded with the 20 cm H-α telescope (Ravindra et al., 2018) at Merak, Ladakh in previous studies (Rengaswamy, Ravindra, and Prabhu, 2019; Unni. C et al., 2021). At the telescope, a Lyot filter (centre λ = 656.28 nm with a 0.5 Å) passband is used. The pixel scale is 0.27″/pixel, and images were taken with 0.7 s exposure time. The median seeing was found to be about 2.7″ at 656.3 nm. We have considered some of the data used in Rengaswamy, Ravindra, and Prabhu (2019) and extended the method further to estimate the isoplanatic angle (see Section 1.2.1 for definitions).

3.3 Measurement of isoplanatic angle

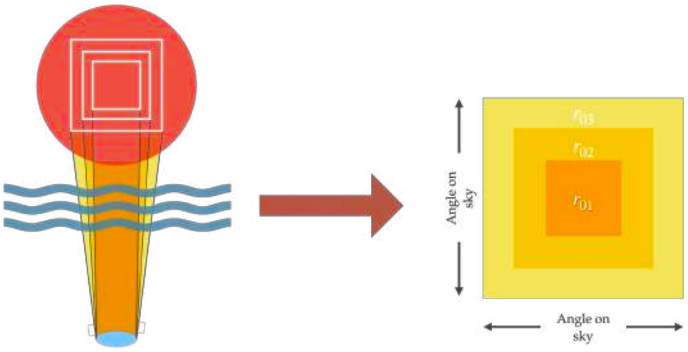

Figure 3.3: Cartoon representation (not to scale) of process of estimating r_0 map from extended PSM. The left portion of the figure shows how choosing different fields of view on the Sun samples different regions of the atmosphere. The right portion shows the r_0 map that is built as a function of field of view.

We extend PSM by increasing the image size used for the deconvolution process in each iteration. We first choose a segment of a certain field of view, apply PSM and estimate an r_0 value. This can be repeated for a number of segments (of the same size) within the same image. Then, a larger segment is chosen and the process is repeated. By applying PSM to segments of different sizes, we obtain a measurement of r_0 for each iteration. This gives us r_0 as a function of the field of view. At larger fields of view, the wave-fronts emitted sample a large volume of the atmosphere; by selecting different regions of the object, we can sample different volumes of the atmosphere. This has been shown in Figure 3.3. The left portion of the figure shows how choosing different fields of view (marked by three white squares of different sizes) on the surface of the Sun (red circle) allow us to sample different volumes (yellow and orange inverted frustums of cones) of the atmosphere (blue waves). The Sun is in the sky-plane and the light blue oval represents the telescope pupil (pupil plane). This allows us to build an r_0 map (shown on the right part of Figure 3.3) with the colours in the map corresponding to those of the 2-D projections of the frustums of the cone denoting the regions of atmosphere sampled.

3.4 Results

The results of the analysis of the data taken from Merak are shown in Figures 3.4 to 3.25. Each figure corresponds to the results analyzed from data acquired on one date and has two plots. The plot on the left is the r_0 (in cm) at 656.3 nm estimated from the extended PSM as a function of the field of view (in arc-seconds) of the segmented image that was used for deconvolution. The date on which the analyzed data were recorded are inset in the corresponding plots. The orange points are the r_0 values estimated from the deconvolution procedure. The iterative deconvolution procedure for the extended PSM was applied to 36 different segments within each image. The maximum angular distance between the two segments chosen for analysis was about $8'$. These were averaged to produce one point (orange point) per image. The process was repeated for all the images recorded in a day. This results in the vertical dispersion of r_0 values at each field angle. The average of the results from all the images recorded on that day are shown in blue points. The plots on the right are r_0 (in cm) estimated from deconvolution as a function of time of observations (UT). The blue, green and orange markers correspond to the field of view of the segments used for deconvolutions ($10.80''$, $15.12''$, and $20.52''$, respectively). This shows the diurnal variation in r_0 (the values are not air mass corrected). The gaps in some of the plots are due to gaps in observation.

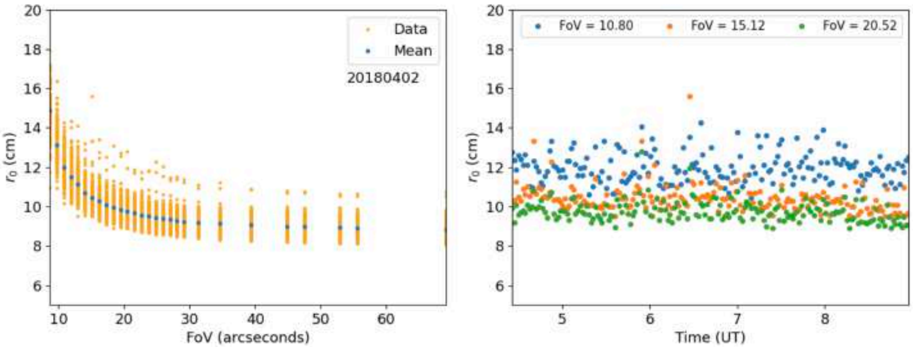

Figure 3.4: Plots of r_0 (cm) estimated through PSM. Left plot is r_0 as a a function of angle (arc-seconds). The angle here is the field of view of the segment of solar image used for the deconvolution process. The orange points correspond to the values estimated from one image. The mean of all the r_0 values for that day are given in blue points. The date on which the analyzed data were recorded is given inset within this plot. The right plot is r_0 versus time of observation (UT). The blue, orange and green markers correspond to $10.80''$, $15.12''$ and $20.52''$ fields respectively.

It can be seen from the figures that as the angular size of the image used for deconvolution increases, the measured value of r_0 decreases. This can be understood as follows: At a very narrow field of view, there is a significant overlap between the air columns through which the constituent wave-fronts traverse before reaching the finite-sized telescope pupil and the relative contribution of the high-altitude turbulence is significant. As the field of view increases, the degree of overlap between the constituent wave-fronts decreases. The resultant wavefront at the pupil encompasses the turbulent effects over the frustum of a cone whose volume increases with the field of view. The area covered by the wavefronts at higher layers also increases. This makes larger fields of view more sensitive to ground-layer turbulence which is stronger during the daytime. Furthermore, the r_0 values begin to plateau beyond a certain field of view - we identify this as the isoplanatic patch size for our long exposure images. Beyond this, we do not see a further degradation of r_0. This appears to be counter-intuitive as it seems to suggest that the r_0 values are decreasing (equivalent to varying PSF) within the isoplanatic angle but reach a plateau (nearly constant PSF) beyond it[2]. However, it must be kept in mind that even though the theoretical definition of isoplanatic angle suggests that the PSF is invariant within this angular region, in practise there will be differences in the PSFs. Furthermore, the decrease in r_0 values is due to the increase in decorrelation of the perturbations when the wavefronts from wider angles are included. The point of plateau is the minimum decorrelation beyond which we do not observe a further decrease in the value of r_0. We estimate the isoplanatic patch size to be between 15 to 20 arc-seconds. C. P. Wang (1975) has shown that the isoplanatic patch size is dependent on the spatial resolution. For low resolution seeing-limited (long exposure) imaging with small telescopes, the isoplanatic size could be quite larger than that expected for speckle imaging or AO correction. After AO correction, the wavefront statistics are no longer Kolmogorov-type. So there is complete lack of homogeneity and isotropy. So all these atmospheric parameters lose original meanings. Therefore, in AO corrected images, one should expect a lower r0 than that for AO uncorrected images. Also, in the case of daytime imaging, the isoplanatic size is expected to be larger than that at night time owing to lower altitude of the seeing layer due to ground heating. The combination of these two factors give rise to an isoplanatic angle around 15″ - 20″ which might higher than expected.

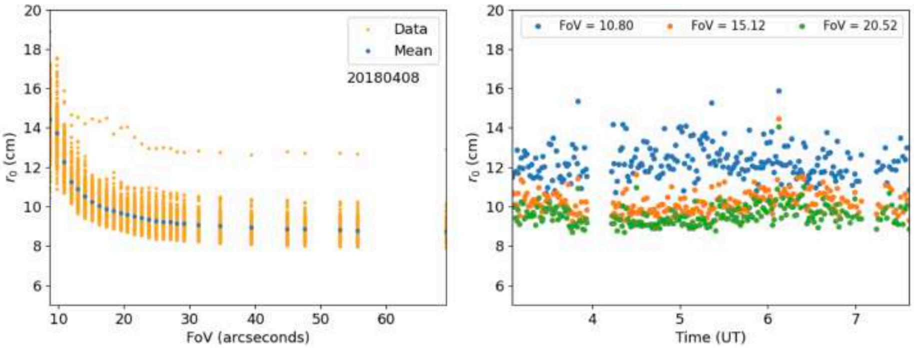

Figure 3.5: Plots r_0 (cm) estimated through extended PSM as a function of angle (left plot) and time of observations (right plot). Markers and legends same as Figure 3.4.

---

[2] A similar trend is noticed when one studies the rms contrast of solar granulation (Equation 5.1). When a small field of view is considered, (a) the estimated contrast seems higher and (b) there is significant variation in the contrast when different regions of same angular field sizes are considered. However, as the field of view is increased, the contrast values eventually reach a plateau beyond which there is no significant change in the contrast. At this field angle, homogeneity is also satisfied, i.e, angular fields of same size anywhere on the Sun do not show significant variations in the contrast values.

In the plots showing the diurnal variation, we can see that the r_0 values are mostly constant and fluctuate about a mean value throughout the day. In some data sets, there is a small decreasing trend as a function of time. Typically, at lake sites it is expected that the seeing does not vary significantly throughout the day. Furthermore, the fluctuations in the estimated r_0 at smaller fields is more than the fluctuations at larger fields.

An interesting point to be noted is that the r_0 values at $26''$ as measured in this work is overestimated when compared to the r_0 values estimated in Rengaswamy, Ravindra, and Prabhu (2019) (for the same set of data). We believe that this is due to the number of averages. Here, we have estimated the r_0 at each field of view at 36 unique positions within an image. In Rengaswamy, Ravindra, and Prabhu (2019), it was done over 121 segments which gives a better averaging. This will only shift the entire curve as an offset and will not affect our isoplanatic size measurements which are based on the plateauing of r_0 and not on the absolute value of r_0.

We believe that this work can be further extended to analytically constrain the C_N^2 profile at a site using the r_0 values we estimated from the extended PSM. The process has been described in Appendix E.

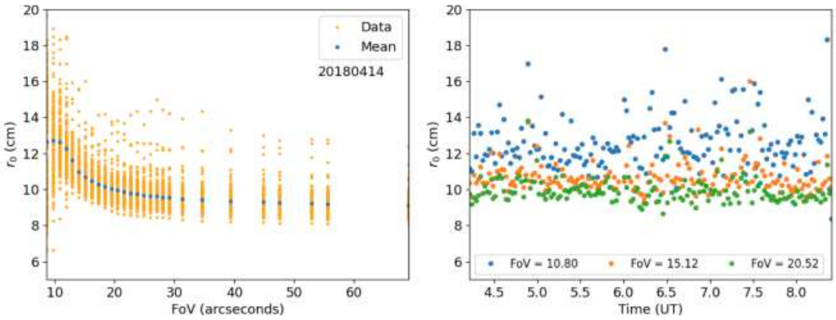

Figure 3.6: Plots r_0 (cm) estimated through extended PSM as a function of angle (left plot) and time of observations (right plot). Markers and legends same as Figure 3.4.

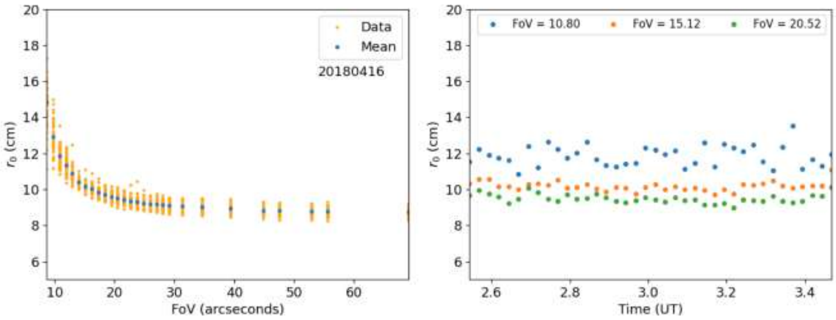

Figure 3.7: Plots r_0 (cm) estimated through extended PSM as a function of angle (left plot) and time of observations (right plot). Markers and legends same as Figure 3.4.

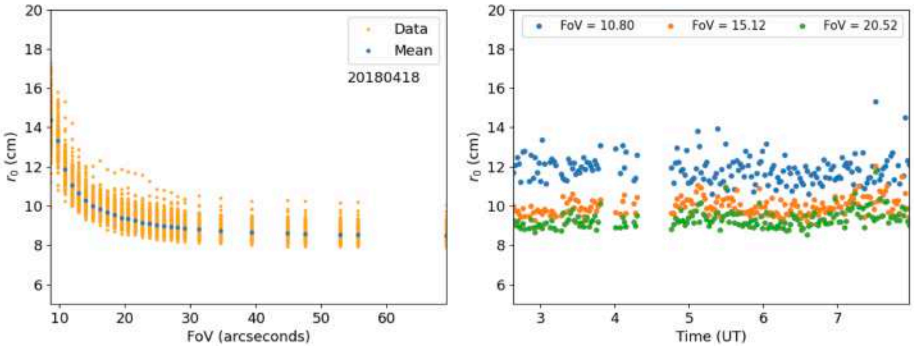

Figure 3.8: Plots r_0 (cm) estimated through extended PSM as a function of angle (left plot) and time of observations (right plot). Markers and legends same as Figure 3.4.

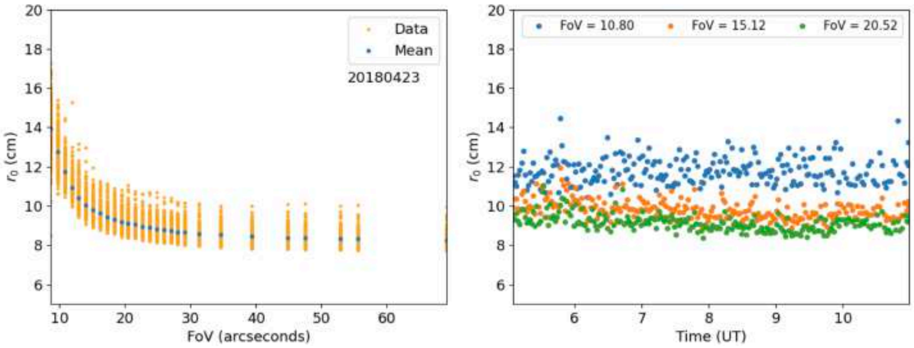

Figure 3.9: Plots r_0 (cm) estimated through extended PSM as a function of angle (left plot) and time of observations (right plot). Markers and legends same as Figure 3.4.

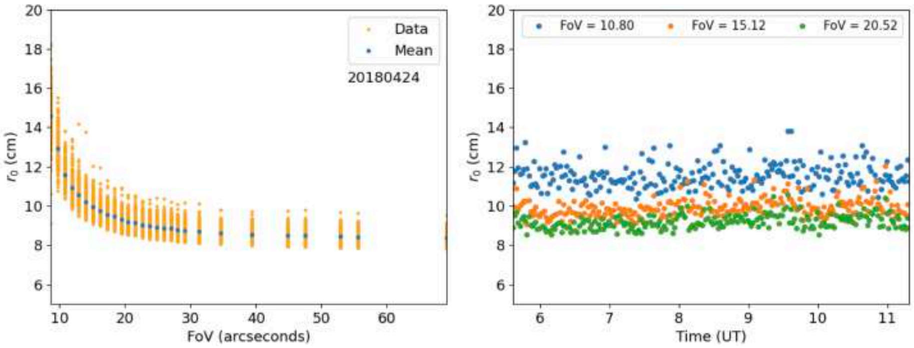

Figure 3.10: Plots r_0 (cm) estimated through extended PSM as a function of angle (left plot) and time of observations (right plot). Markers and legends same as Figure 3.4.

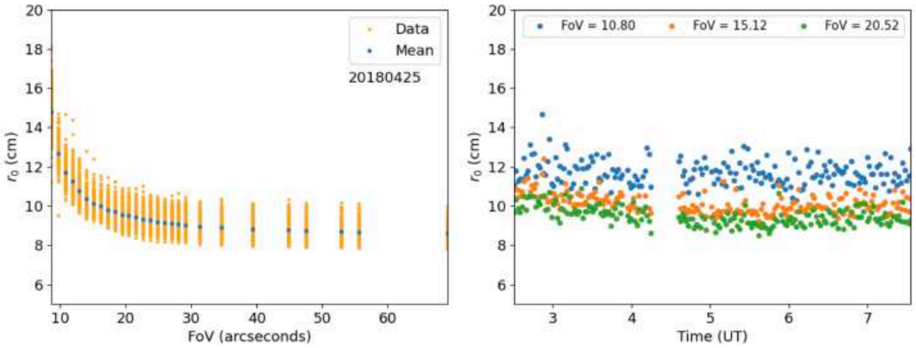

Figure 3.11: Plots r_0 (cm) estimated through extended PSM as a function of angle (left plot) and time of observations (right plot). Markers and legends same as Figure 3.4.

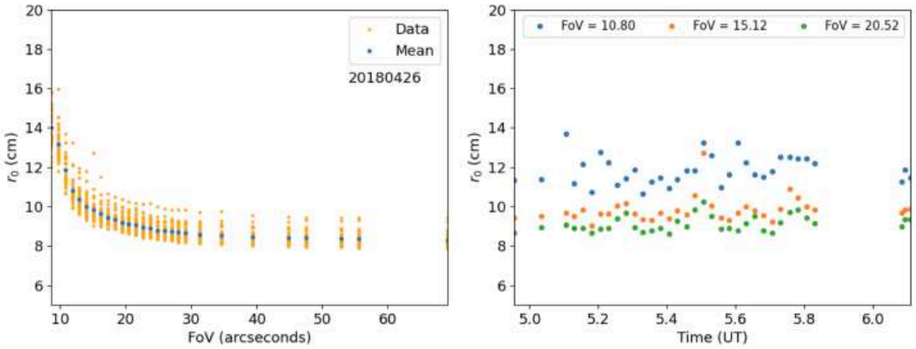

Figure 3.12: Plots r_0 (cm) estimated through extended PSM as a function of angle (left plot) and time of observations (right plot). Markers and legends same as Figure 3.4.

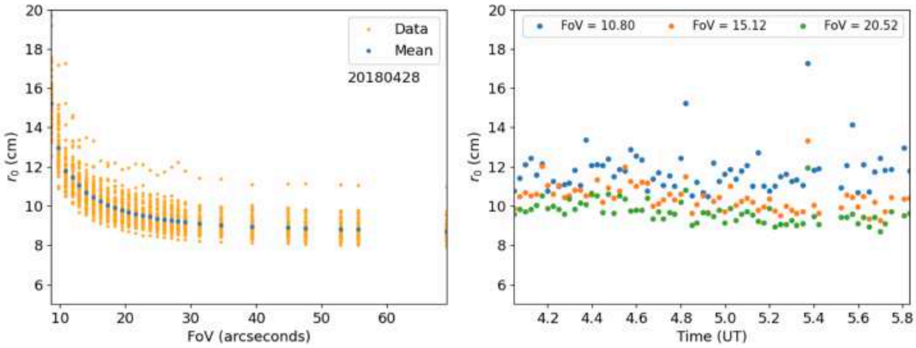

Figure 3.13: Plots r_0 (cm) estimated through extended PSM as a function of angle (left plot) and time of observations (right plot). Markers and legends same as Figure 3.4.

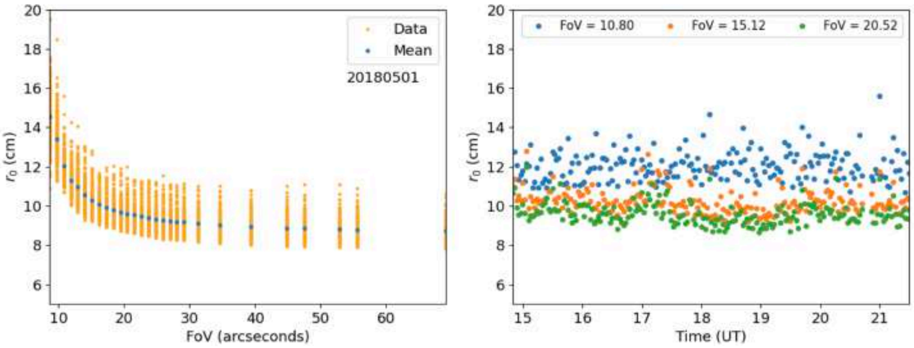

Figure 3.14: Plots r_0 (cm) estimated through extended PSM as a function of angle (left plot) and time of observations (right plot). Markers and legends same as Figure 3.4.

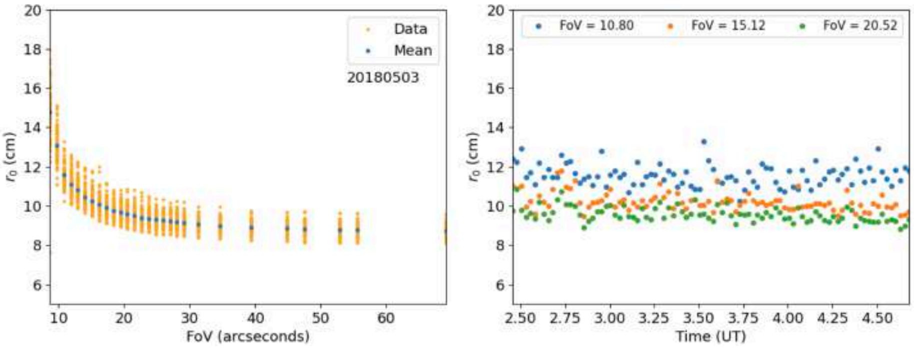

Figure 3.15: Plots r_0 (cm) estimated through extended PSM as a function of angle (left plot) and time of observations (right plot). Markers and legends same as Figure 3.4.

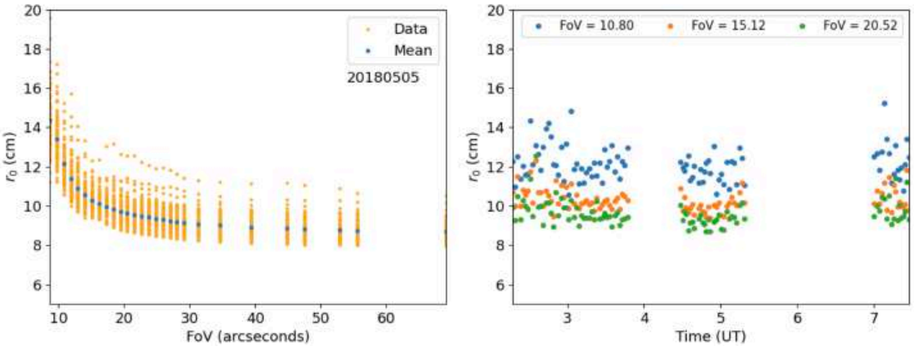

Figure 3.16: Plots r_0 (cm) estimated through extended PSM as a function of angle (left plot) and time of observations (right plot). Markers and legends same as Figure 3.4.

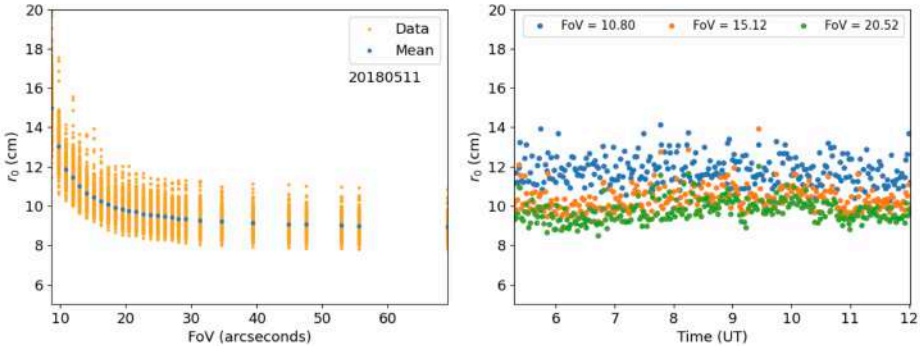

Figure 3.17: Plots r_0 (cm) estimated through extended PSM as a function of angle (left plot) and time of observations (right plot). Markers and legends same as Figure 3.4.

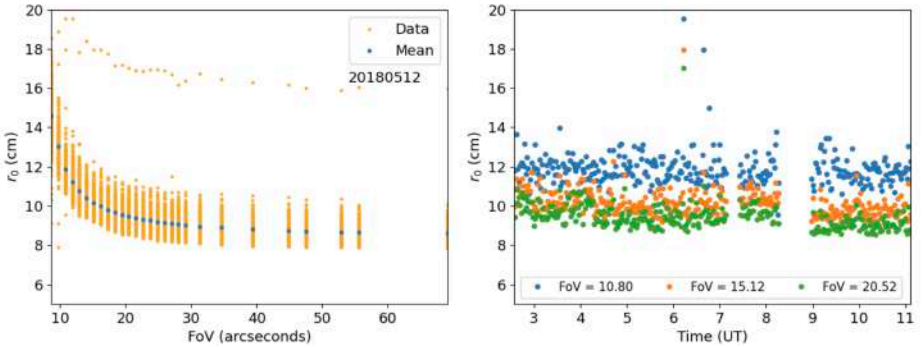

Figure 3.18: Plots r_0 (cm) estimated through extended PSM as a function of angle (left plot) and time of observations (right plot). Markers and legends same as Figure 3.4.

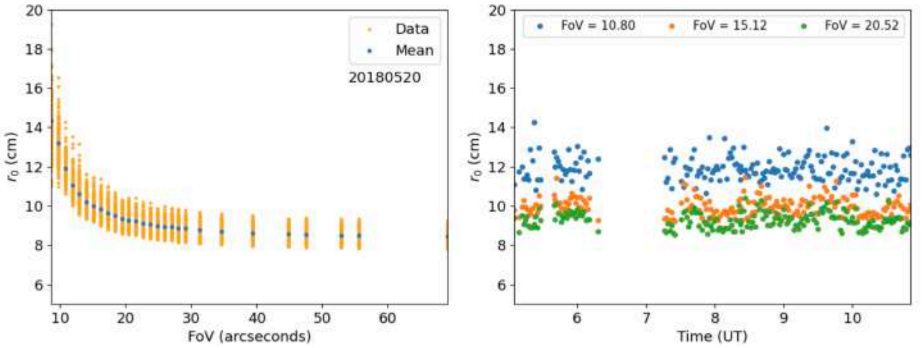

Figure 3.19: Plots r_0 (cm) estimated through extended PSM as a function of angle (left plot) and time of observations (right plot). Markers and legends same as Figure 3.4.

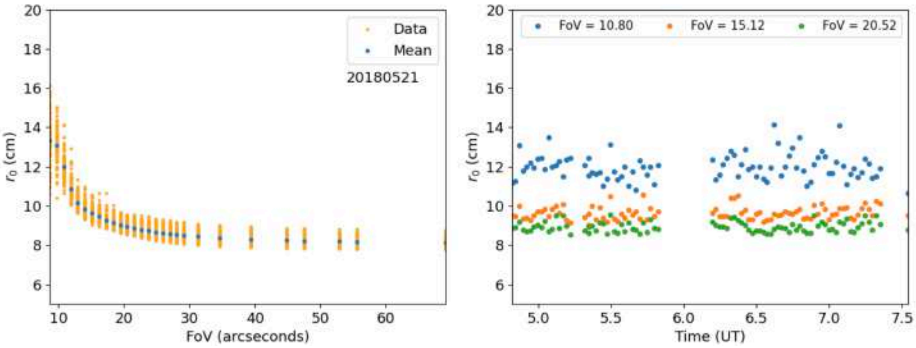

Figure 3.20: Plots r_0 (cm) estimated through extended PSM as a function of angle (left plot) and time of observations (right plot). Markers and legends same as Figure 3.4.

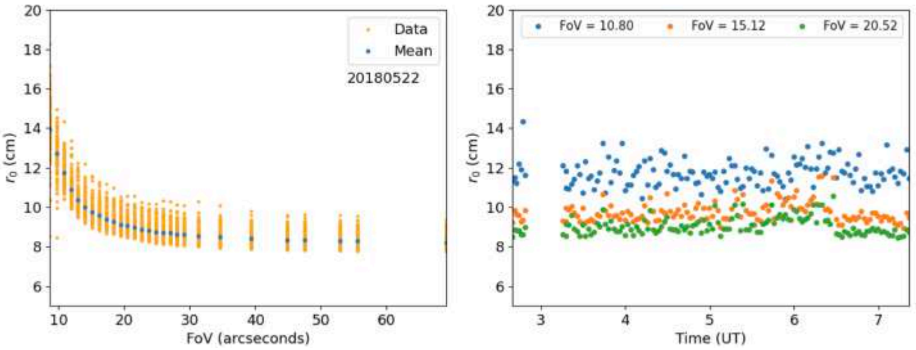

Figure 3.21: Plots r_0 (cm) estimated through extended PSM as a function of angle (left plot) and time of observations (right plot). Markers and legends same as Figure 3.4.

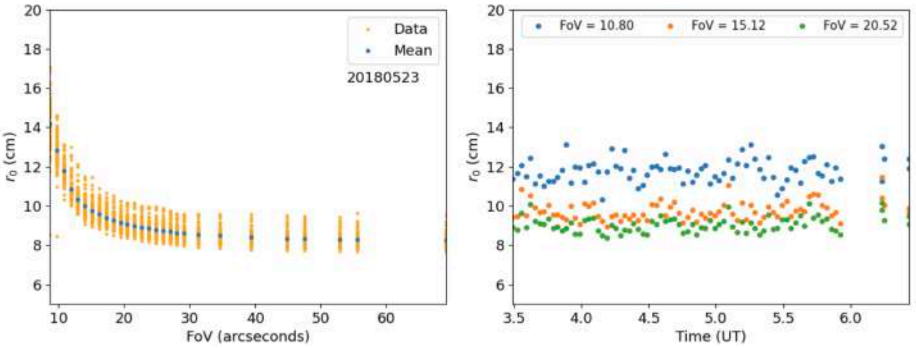

Figure 3.22: Plots r_0 (cm) estimated through extended PSM as a function of angle (left plot) and time of observations (right plot). Markers and legends same as Figure 3.4.

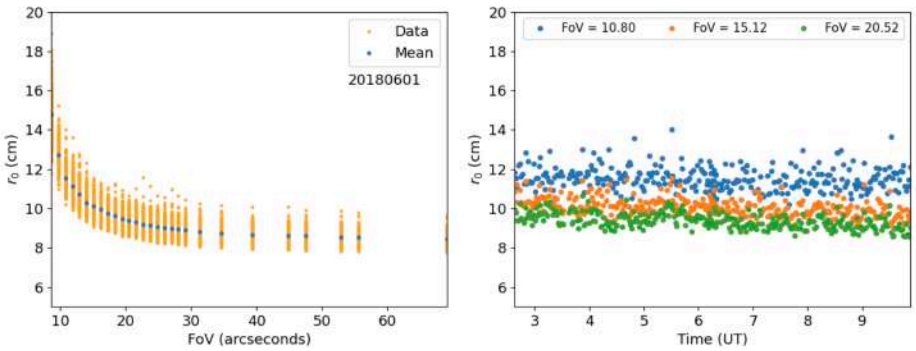

Figure 3.23: Plots r_0 (cm) estimated through extended PSM as a function of angle (left plot) and time of observations (right plot). Markers and legends same as Figure 3.4.

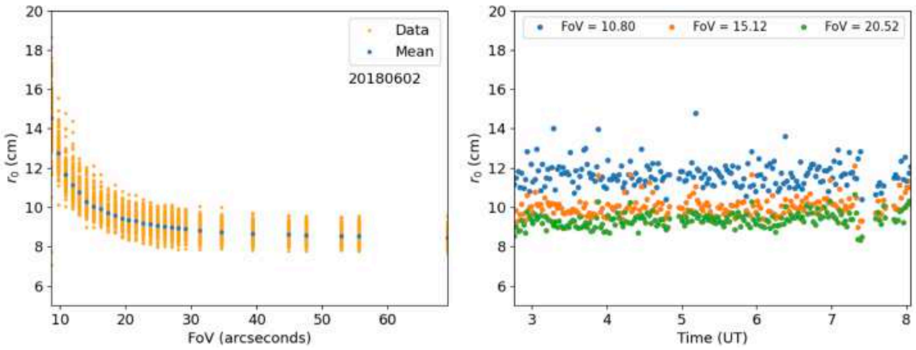

Figure 3.24: Plots r_0 (cm) estimated through extended PSM as a function of angle (left plot) and time of observations (right plot). Markers and legends same as Figure 3.4.

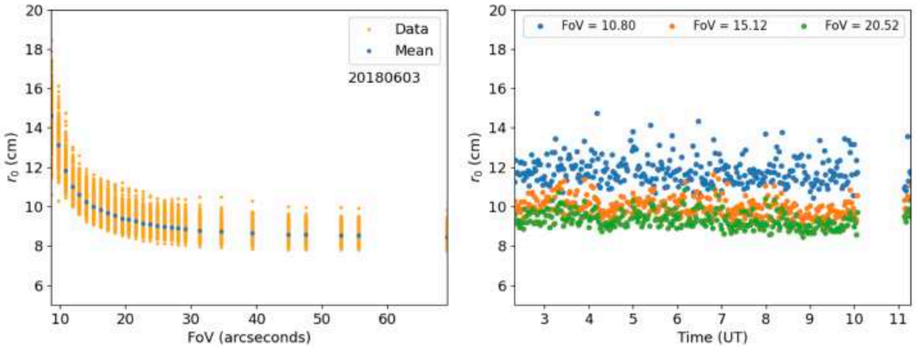

Figure 3.25: Plots r_0 (cm) estimated through extended PSM as a function of angle (left plot) and time of observations (right plot). Markers and legends same as Figure 3.4.

Chapter 4

AO and MCAO Systems

> *"Science is magic that works."*
> *Kurt Vonnegut (Cat's Cradle)*

The work presented in this chapter has been reported in the publication:

Design of AO and MCAO system for the Kodaikanal Tower telescope
Saraswathi Kalyani Subramanian, Sridharan Rengaswamy, 2024, **Proc. SPIE 13097, Adaptive Optics Systems IX**.

4.1 Introduction

As stated in Section 1.5, the long-term goal of the AO program at IIA is demonstration of AO/MCAO system at KTT. In that context, we have begun work on the design of the systems. We discuss the design of the AO system in Section 4.2. This design has been set-up in the laboratory along with some work on the control code for the WFS completed. In the section, we also detail the alternate SCAO system that we designed due to constraints of the WFS camera. Finally, we will discuss the design of the MCAO system in Section 4.3.

4.2 AO System

We begin with discussions of the schematic and the various parameters we considered during the design of the SCAO system. The schematic is given in Figure 4.1. The image of the Sun is formed at the prime focus (dashed line in Figure 1.10) of KTT. A field stop can be placed here to select the desired field of view which will be used in our AO system. First, an achromatic lens is used for collimating the light. After reflection by the TT (tip-tilt) mirror, the light is split into two branches. One branch will focus the light onto a camera called as the TT camera or correlation tracking camera. The other branch is further split into two post reflection by the DM. One of the split branches is imaged onto a science detector. This will be the AO-corrected science arm. The light can also be fed to any other science instrument like a spectrograph or a spectro-polarimeter. The second branch of light is for wavefront sensing (here, with a SHWFS). The reimaging optics preceding the SHWFS is planned such that there is an intermediate focus. This will allow us to use a second field stop to further reduce the field of view seen by the WFS camera, if required.

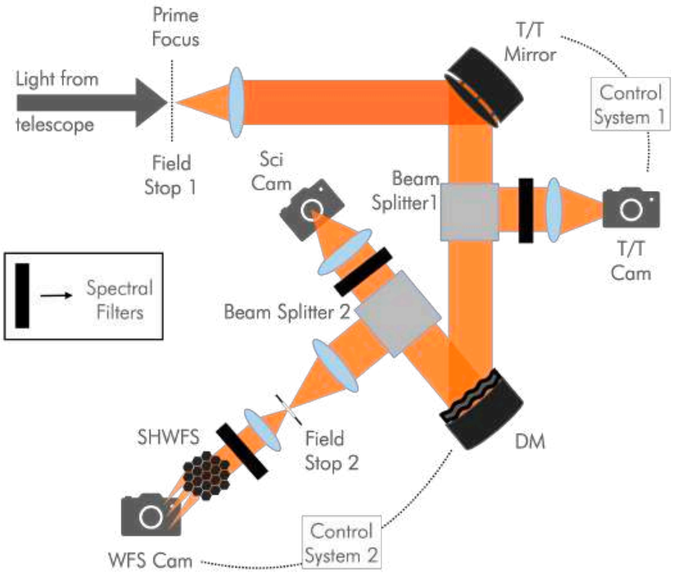

Figure 4.1: Schematic representation of SCAO setup for KTT (not to scale).

One important facet of our design is the use of a separate correlation tracking camera which will be used for the control of the TT mirror. This requires an additional beam splitter (reducing the light to the WFS and science cameras), additional optics (lens for imaging) and another detector and associated electronics. The alternate would be to exclude that arm from the SCAO design and reconstruct the global wavefront from the local slope measurements of the SHWFS. We opine that our design will offer better TT control since reconstructing the global slope from local measurements may not be perfect. Furthermore, for the seeing conditions at our site combined with the smaller size of our telescope, global image motion will be the dominant error. In our design, the field of view in the TT camera is also larger than that of the SHWFS for this reason. The plan for on-sky demonstration is to achieve image stabilization first by only controlling the TT mirror and then starting the loop for higher order control. Furthermore, since our science instrument for

AO demonstration is only imaging (not photon starved), we can afford the loss in intensity (at the science camera) in our design.

Now, we need to specify some parameters so that we can design the system. For example, the number of fully illuminated sub-apertures will determine the level of AO correction. Fewer sub-apertures will sparsely sample the wavefront and can perform only low-order correction. To begin with, we are interested only in understanding the complexities and functioning of the AO system. Therefore, we planned for and designed a low-order AO system. The number of actuators in the DM which will be used for control also depends on the number of sub-apertures. Finally, we also need to determine the field of view that will be seen by each of the three cameras. The plan is to acquire images for the correlation tracking camera at H-α, for the SHWFS camera at 540 nm and for the science camera at 854.2 nm. These are shown by thick black bars which represent spectral filters in the schematic (Figure 4.1).

From earlier studies, we know that the median seeing at Kodaiakanal (Rengaswamy, 2016; Subramanian, Rengaswamy, et al., 2024) is about 4.5 cm at 550 nm and our goal is to develop a low-order AO system. Therefore, we set two to three times median r_0 (= 9 cm to 13.5 cm) as the limits for each hexagonal sub-aperture diagonal (equivalent to circle diameter) when projected on the pupil. This corresponds to 3, 4 or 5 lenslets across the diameter. It is better to have an odd number of lenslets to match the mapping with actuator geometry. However, having 3 lenslets across the diameter corresponds to a total of 7 lenslets across the pupil. The sampling is very coarse. Therefore, we opted to have 5 lenslets across the diameter in our AO design. The diagonal of one sub-aperture as projected on to the pupil is 7.2 cm. Typical AO correction happens within the isoplanatic angle, therefore the field of view at the WFS camera can be a maximum of $13''$ (accepting some amount of anisoplanatic effects). On the other hand, it is better to have a larger field of view to measure the global tilt (the lower order terms are correlated over a wider field of view - see Figure E.1). We decided that the maximum field of view at the TT and science cameras can be 1 arc-minute. An interesting point is that having the science camera field of view be larger than the isoplanatic angle allows us to see the effect of anisoplanatism and the effect of AO-correction over a small region of the image (near the AO lock point).

4.2.1 Design

The SCAO design for KTT has a field stop at the prime focus to restrict the field of view entering the AO system to 30×30 arc-second^2. Following this a 1000 mm focal length collimator is used to collimate the light onto the TT mirror, where the beam diameter is 14.2 mm (for the given field of view). Then, the light in the correlation tracking arm is brought to a focus using a 100 mm focal length lens. An Andor Zyla 5.5 camera is used as the correlation tracker. The image formed here has a pixel scale of $0.37''$/pixel. The diffraction-limit of KTT at H-α is about $\sim0.46''$. The sampling at the correlation tracking camera is less than a pixel per diffraction limit of the full primary aperture. Our images are under-sampled for the diffraction-limit. This is acceptable since the images are seeing-limited to start with.

Table 4.1: Summary of SCAO (a) system parameters.

Parameter	Value
Number of lenslets fully illuminated	19
Diagonal of lenslet (projected to pupil plane)	7.2 cm
Pixel scale on WFS camera	$0.25''$/pixel
Field of view of WFS camera	13×13 arc-second^2
Number of actuators illuminated	37
Pixel scale on correlation tracking camera	$0.37''$/pixel
Field of view on correlation tracking camera	30×30 arc-second^2
Pixel scale on science camera	$0.26''$/pixel
Field of view on science camera	30×30 arc-second^2

The other arm transmits the light to the DM which is placed at the back focal plane of the collimating lens. It is crucial that the DM is aligned properly to the conjugate of the pupil plane. We are using a 37 actuator MMDM from OKO Tech. The beam diameter on the DM is about 10.2 mm and illuminates all 37 actuators. The DM is tilted such that the angle of incidence of the beam is about 10° (Bayanna, Louis, et al., 2015). After reflection by the DM, the light is once again split into two arms. One arm is used for the science imaging (ANDOR iKon-L 936 camera). A 300 mm focal length lens is used to focus the light on the camera; AO-corrected image will be available at a sampling of $0.26''$/pixel. The KTT diffraction-limit at 854.2 nm is $\sim0.6''$. The other arm is for wavefront sensing. First, a 200 mm focal length lens is used to form an image; a field stop is used in the intermediate focal plane before the WFS to restrict the wavefront sensing field of view to 13×13 arc-second^2. Following this, a 30 mm focal length lens is used to collimate the beam; the lenslet array is placed at the re-imaged pupil plane. We are using the SHWFS from OKO Tech (serial number: FS1540-H300-F18-16.04) mounted on a camera from uEye (IDS UI-1540LE-M-GL66). The image on the WFS camera has a sampling of $0.25''$/pixel. For a 7.2 cm sub-aperture, the diffraction-limit is about $1.9''$ at 540 nm. Therefore the image at the SHWFS camera is highly oversampled. This will be compensated in the control code by resampling the images to $0.5''$/pixel. This also reduces our computational load as it reduces the size of the image. We have developed programs in C using the two image motion estimation algorithms (with optional parabolic interpolation) discussed in Appendix A. We noticed that the maximum speed of our WFS camera is 250 fps (frames per second) with the current set-up (for a full image size of all 19 lenslets is about 290×250 pixels). This might be too slow since the daytime turbulence strength is much stronger than nighttime and, therefore, requires faster correction. However, we are not aiming for diffraction-limited correction. Therefore, we anticipate that we will have acceptable performance (for a low-order AO system). On-sky testing is required to better understand and quantify this performance. Therefore, we have also considered an alternate design for the SCAO set-up. The current set-up is called SCAO (a) and its parameters are summarized in Table 4.1.

4.2.2 Alternate design - SCAO (b)

Since our goal was to demonstrate a low-order solar SCAO system, the speed of the WFS camera might not severely limit the performance of the current system. However, if we want to upgrade the system in the future by increasing the order of terms for which correction is done (more sub-apertures illuminated on lenslet array), we require a new set-up. The alternate design only modifies the WFS-arm of the SCAO (a) set-up; it is called SCAO (b). The components for this are yet to be procured and this is still in the design stage. Only the WFS arm is modified. We have considered the hexagonal lenslet array from OKO Tech (APH-Q-P1000-F36,7). This has a pitch of 1000 μm and a focal length of 36.7 mm. This along with the ANDOR Zyla 5.5 camera (same as the correlation tracking camera) have been considered for the design. As a first step, we will keep the number of lenslets the same as SCAO (a) and improve only the the speed of the control. This will help us ascertain if we are truly limited by the speed of the WFS camera in SCAO (a). Then, we will increase the number of fully illuminated lenslets. For example, increase the number of lenslets across the diameter to 7 (see Table 4.2). The sampling in the image plane has maintained close to that of SCAO (a), but can be changed by adding additional optics between the lenslet array and the detector, if required. This is the main advantage of the SCAO (b) design. In the SCAO (a) setup was limited by the lenslet array and camera being fused together on a single mount. This reduces flexibility in the design. Decoupling the re-imaged pupil plane and the detector plane, allows us to introduce another set of reimaging optics between the re-imaged pupil (lenslet array) plane and image (camera). SCAO (b) also allows us to have a larger field of view at the wavefront sensor, when compared to SCAO (a). This allows us to reuse the same components for the MCAO setup.

Table 4.2: Summary of SCAO (b) system parameters. NOTE: Only parameters that have been changed from SCAO (a) are shown in this table.

Parameter	Value
Number of lenslets fully illuminated	37
Diagonal of lenslet (projected to pupil plane)	5.9 cm
Pixel scale on WFS camera	0.28″/pixel

4.3 Design of MCAO

From the results of the work reported in Chapter 2, we know that the second DM of our MCAO system must be conjugated to the 3 km layer above the observatory. We have designed it such that, the WFS that will control the pupil DM is kept in-between the pupil and high altitude DMs. This is similar to the configuration at the Dunn Solar Telescope (T. Rimmele, Hegwer, et al., 2010) and the Vacuum Tower Telescope (Berkefeld, Soltau, and O. von der Lühe, 2005). Apart from being easy to modify an existing system and switching between SCAO and MCAO modes, it has the added advantage of the first SHWFS being "blind" to the effect on the high altitude DM (Schmidt, Berkefeld, and Heidecke, 2012). The MCAO uses the same lenslet + WFS camera design as the SCAO (b) design. We have opted for having the same number of lenslets as the SCAO (a) system as a starting point.

Figure 4.2 shows the schematic of the planned system. The first part of the system is the same as SCAO (a or b) left undisturbed. Only the science channel is modified to introduce a second DM (which will be conjugated to the 3 km layer) and a second SHWFS. This SHWFS is the same as the one used in SCAO (b) setup ((APH-Q-P1000-F36,7)). We use a fold mirror to fold the beam due to space constraints at the telescope. Since the current plan is to run the lower layer loop and higher layer loop independently, the control code will not have significant differences. To start with, it is planned to have a field of view of about 30x30 arc-second^2 at the second SHWFS. This will be split into four guide regions of 12x12 arcsecond^2 each and used to control DM$_{3\mathrm{km}}$. It currently designed such that the two DMs have the same specification. The full field of view can be extended to $1'$, once we achieve satisfactory performance with a smaller field.

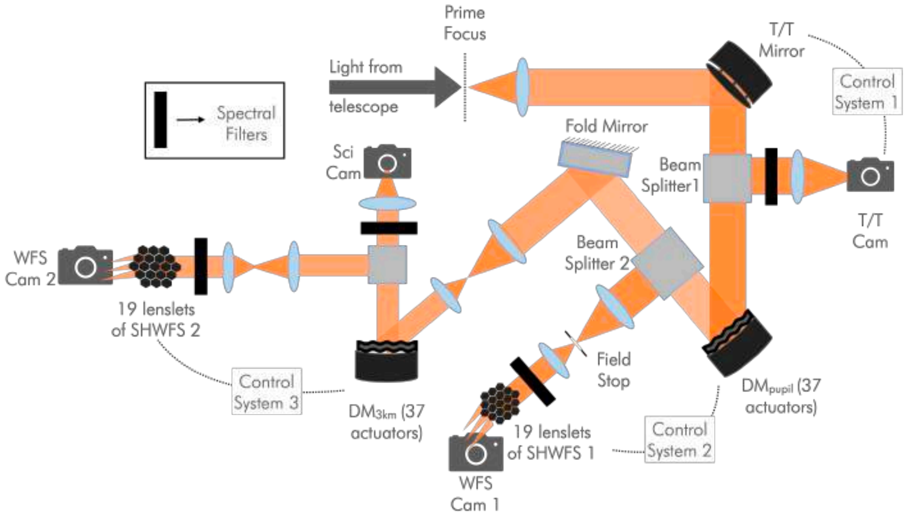

Figure 4.2: Schematic representation of MCAO setup for KTT (not to scale).

Chapter 5

Image Quality Specification for Solar Telescopes

> *"Looking through the atmosphere is somewhat like looking through a piece of old, stained glass. The glass has defects in it, so the image is blurred from that."*
>
> *Nancy Grace Roman*

The work presented in this chapter has been reported in the publication:

Image Quality Specification for Solar Telescopes
Saraswathi Kalyani Subramanian, Sridharan Rengaswamy, 2023, **Solar Physics** 298, 15.

5.1 Introduction

As stated in Setion 1.4.3, it is important to have an image quality metric so that we can specify/quantify the performance of our solar telescope and AO system. There are many parameters that are used to characterize the image quality of solar telescopes (Popowicz et al., 2017). The image quality metrics (IQM) are broadly classified into three categories - full reference, reduced reference, and no-reference methods (Deng et al., 2015). As the names suggest, the first two metrics are completely or partially dependent on a reference image based on which the quality of other images can be determined. The metrics of the last category are completely independent of a reference image. In the case of ground-based telescopes, where the image is corrupted by the atmosphere and instrumental effects, it is difficult to select an ideal reference image. Therefore, no-reference IQM is preferred. The rms granulation contrast is one such metric.

Therefore, in this thesis, we use it to specify the image quality both in the presence and absence of the adaptive optics compensation. Although there is quite a bit of intrinsic variation of the rms granulation contrast (Scharmer, Löfdahl, Sliepen, et al., 2019), its choice as a metric is quite useful and practical owing to the presence of granulation throughout the solar disk independent of the solar activity cycle. The intrinsic low contrast of the granulation prevents their use for adaptive optics wavefront sensing when their observed contrast is further lowered due to poor observing conditions (low r_0).

In Section 5.2, we start by describing the simulations that we have developed in Python. Then, in Section 5.3, we validate our simulations by comparing our results from well-established analytical expressions for various parameters. Section 5.4 presents the results of simulations and compares them with the results from another image quality metric. Here, we also compared our simulations with previously reported values of rms granulation contrasts and Strehl ratios from the literature. This was then used to estimate the efficiency of solar AO systems.

5.2 Simulations

Our aim was to develop a database that would allow users to quantify the performance of solar telescopes and AO systems, given the diameter of the telescope (D), the seeing (specified as r_0), and the level of AO correction (expressed as the number of Zernike terms compensated, N_z). For this, we developed our own simulations in Python with 'D', r_0, and N_Z being the main free parameters. We opted for rms contrast (C_{rms}) of the solar granulation as a metric. For a two-dimensional digital image array $s(x,y)$, it is defined as

$$C_{rms} = \left[\frac{s - \langle s \rangle}{\langle s \rangle}\right]_{rms}, \tag{5.1}$$

where $\langle\ \rangle$ indicates spatial average and $s(x,y)$ could be an object intensity distribution or an image intensity distribution. We have also considered another IQM called Median Filter Gradient Similarity (MFGS). It is a no-reference IQM. The results from this are discussed in Appendix F.

The overall flow of the simulations is shown diagrammatically in Figure 5.1. As shown in the image, we first consider simulated granulation images (see Section 5.2.1). This is followed by an ideal diffraction-limited telescope pupil of diameter (D, see Section 5.2.3.1). This gives rise to an ideal diffraction-limited image. If we consider atmospheric turbulence described by the Kolmogorov theory of turbulence (Section 5.2.2), we get seeing-limited images. Finally, if we model AO corrections (Section 5.2.3.2), we get AO-corrected images. The metric is always applied to an average long exposure image (with or without AO correction, as the case may be) normalized to unit mean intensity (measured in counts). For the results shown in Figure 5.1, we have used D = 200 cm, r_0 = 10 cm and N_z = 35 terms.

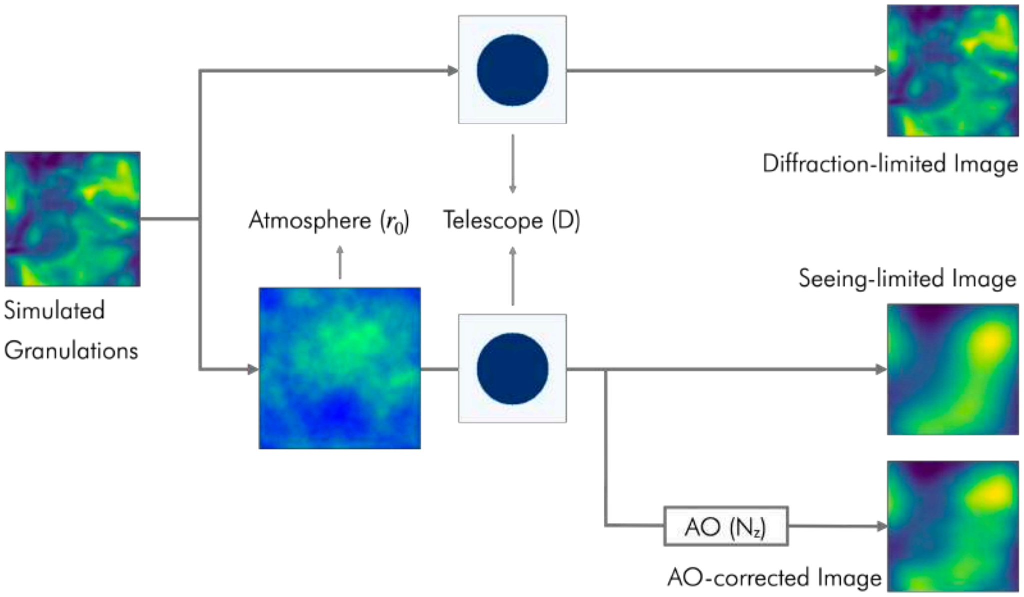

Figure 5.1: Diagrammatic representation of simulation workflow (images not scaled). The simulated granulations are the “objects”. The branch which simulated only a telescope of aperture ‘D’ gives ideal, diffraction-limited images. If a single layer of atmospheric turbulence (specified using Fried’s parameter, r_0) is used, it gives seeing-limited images. Finally, if AO correction is done (specified as the number of Zernike terms corrected, N_z), it gives AO-corrected images.

5.2.1 The Object Model

We used simulated solar granulation images as against space or ground-based images as input objects in our simulations. This choice was driven by the fact that neither space-based images nor ground-based images—AO corrected alone or AO plus speckle or phase-diversity corrected—are likely to be completely free from residual instrumental effects and thus may bias the results based on their use. Further, with the advent of advanced cluster computational facilities, we are now able to synthesize instantaneous bolometric solar granulation images fairly accurately. The high-resolution structure of the solar photospheric granulation employed in this work is a snapshot of the bolometric intensity from a 3D numerical simulation carried out with the radiative magnetohydrodynamic (MHD) code CO5BOLD (Freytag et al., 2012), which solves the coupled system of compressible MHD equations that include an imposed gravitational field and non-local, frequency-dependent radiative transfer. The simulations were performed on a 3D Cartesian box of size 9.6 x 9.6 x 2.8 Mm^3, with a uniform grid size of 15 x 15 x 10 km^3 in (x,y,z). The vertical domain ranges from about 1300 km below the optical depth $\tau_{500} = 1$ surface (photosphere) to 1500 km above it in the chromosphere and the gravitational field is uniform and vertical with values of log (g) = 4.44.

A constant entropy inflow is supplied at the bottom boundary of the simulation domain to maintain an average surface effective temperature of T_{eff} = 5770 K. The simulation box set up as above was derived from a CO5BOLD simulation performed by Calvo, Steiner, and Freytag (2016), and the computations were carried out by Prof. S. P. Rajaguru (private communication) using IIA's HPC (Indian Institute of Astrophysics' High-Performance Computing) cluster Nova.

It should be emphasized that we use only a small segment of the high-resolution solar granulation image for the work presented in this article, and the segment size, which is basically the field of view, is set by the other simulation parameters (See Section 5.2.4.1).

5.2.2 The Atmospheric Model

We model the phase perturbations induced by the atmosphere through a two dimensional phase-screen generated using the Kolmogorov model of turbulence (Rengaswamy and Bayanna, 2004; Padinhatteeri, Sridharan, and Sankarasubramanian, 2010; Unni. C et al., 2021). The phase-screen is characterised by the Fried's parameter r_0. A large phase-screen of size 163.84 × 163.84 m^2 is simulated with a pixel sampling of 2 cm. Assuming frozen-field approximation, the phase-screen is blown past the telescope aperture and several thousands of segments of the phase-screen with size equal to the size of the aperture are used.

In our simulations, we generated phase screens with r_0 varying discretely between 6 cm and 21 cm (at λ = 430.5 nm) with a step size of 1 cm, to account for the wide range of the daytime seeing conditions.

5.2.3 The Instrument Model

5.2.3.1 The Telescope

We used an un-obscured 2 dimensional pupil function $W(\mathbf{x})$ described by

$$W(\mathbf{x}) = \begin{cases} 1, |\mathbf{x}| \leq D/2 \\ 0, |\mathbf{x}| > D/2 \end{cases} \tag{5.2}$$

to model the telescope, where $\mathbf{x}$ represents the spatial coordinates at the pupil and D is the aperture size. Several distinct values of pupil diameters were used starting from 30 cm to 200 cm, the values were chosen to represent the aperture size of the solar telescopes available in India and elsewhere in the world.

5.2.3.2 Modelling AO corrections

We implemented the AO correction in an idealistic way. We decomposed the instantaneous phase-perturbations over the pupil into a given number, N_Z, of Zernike Polynomials (Noll, 1976) using a least-square solution method (Stewart, 1993). A model phase front (phase perturbations over the pupil) was then synthesized from the Zernike coefficients obtained from the least square method and subtracted from the initial perturbed phase-front to obtain the residual phase perturbations after "AO correction". As we sampled the phase screen with a sampling of 2 cm, and made a pixel-wise correction, it is an ideal correction up to 2 cm. Perturbations on spatial scales less than 2 cm are neither generated nor compensated in our approach. The number of Zernike polynomials used to model a given phase perturbation increased in steps of two radial orders at a time (2, 9, 20, 35, and so on) until the variance of the residual phase perturbations over the pupil becomes less than 1 radian^2 (Equation 1.14). This criterion essentially enables us to terminate the simulation at a particular r_0' (that could be any value between 6 and 21) for a given D.

5.2.4 Simulation Flow

We assume unit amplitude perturbations and obtain the instantaneous PSF as the modulus squared Fourier transform of the pupil-plane phase distribution (product of the ideal pupil function $W(\mathbf{x})$ and the phase perturbations $\phi(\mathbf{x})$ represented by a single segment of the phase screen of a given r_0) expressed in complex exponential form $W(\mathbf{x})\exp[j\phi(\mathbf{x})W(\mathbf{x})]$. We obtain the instantaneous transfer function as the inverse Fourier transform of the area-normalized instantaneous PSF. We model the instantaneous image as the convolution of the object intensity distribution with the instantaneous PSF. In practice, the convolution is achieved through an inverse Fourier transform of the product of the Fourier transform of the object intensity distribution and the instantaneous transfer function.

The instantaneous images are averaged over 1000 realizations of the atmospheric phase perturbations and an average image is obtained. The process is repeated 10 times so that we can obtain an average rms contrast and the variations associated with it. We found the variations in rms contrast to be much smaller than a significant fraction of the actual contrast. So, they were not visible when plotted as error bars. The process is repeated for AO-corrected images as well to get the corresponding values. Finally, we added the photon noise to the images. However, we found that rms granulation contrast is immune to this photon noise.

Thus, the main free or input parameters in our simulation are the telescope diameter D, the atmospheric coherence diameter r_0, and the number of compensated Zernike terms N_Z. The metric we use to characterize the average image (with and without AO correction, as the case may be) is the rms granulation contrasts C_{rms}. In addition, we also use traditional metrics like the residual mean square phase variance over the pupil after AO correction and the Strehl ratio of an average stellar PSF. Figure 5.2 shows the snapshots from the various components in the flow of the simulation. The top left and right panels indicate the object (simulated solar granulation) and the diffraction-limited image intensity distributions, respectively. The second row of panels indicates the pupil-plane phase distributions. The images on the bottom panels indicate instantaneous and long exposure images (third and fourth rows), respectively, without (left) and with (right) AO correction.

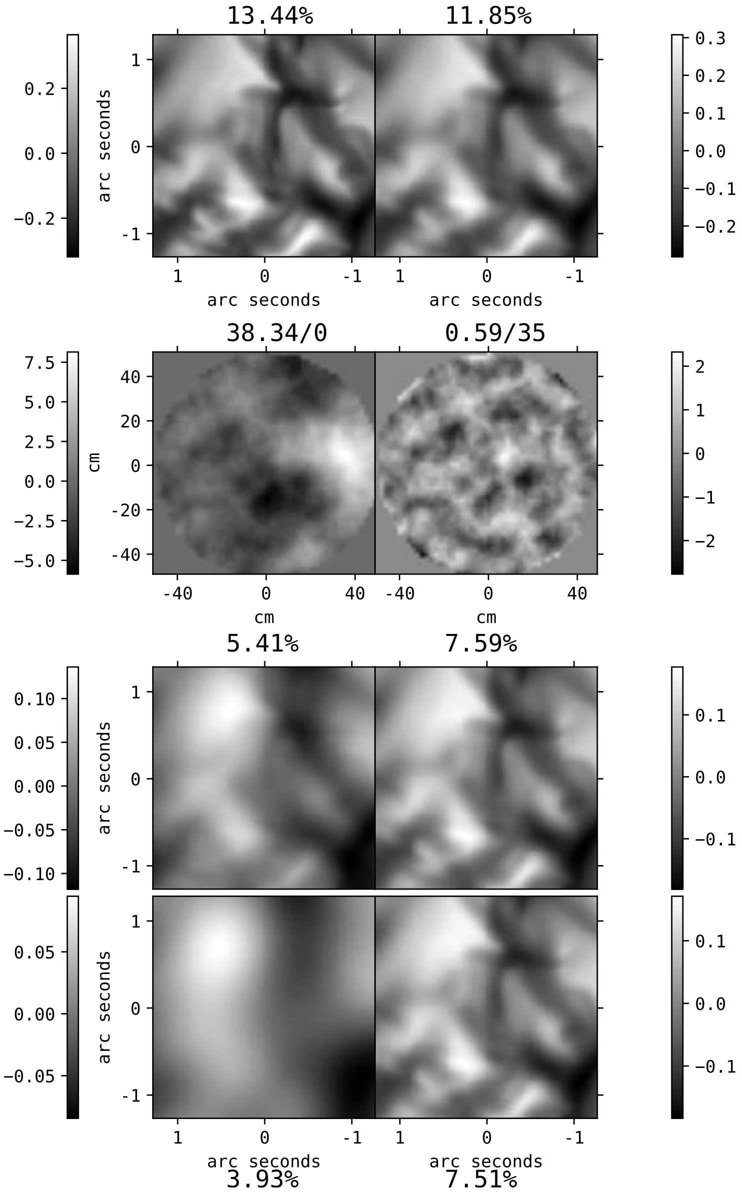

Figure 5.2: Top panels indicate the object (left) and the diffraction-limited (right) image intensity distributions. Panels on the second row indicate the residual phase distributions without (left) and with (right) AO correction. The mean square residual phase variance/number of Zernike terms for which the correction is done are indicated on the top. Panels on the third row indicate instantaneous images without (left) and with AO correction (right). Panels on the last row show the long exposure images without (left) and with AO correction (right). The quantities expressed in percentage are the rms contrast values for the respective images.

5.2.4.1 Field of view and Wavelength Dependency

As we perform the Fourier transform using Fast Fourier Transform routines that keep the number of pixels the same in either domain, we constrain the simulation window size to be at least twice that of the aperture size, with the aperture centered on the window so that the transfer function is not truncated. As our simulations involved different aperture sizes, we chose a window size of 256 × 256 pixels so that apertures of up to 128 pixels could be simulated. This leaves us with the feasibility of performing simulations up to 2.56 m diameter aperture, for a 2 cm pixel sampling. However, we have performed simulations only up to $D = 2$ m. As a result of the Fourier transformation relation between the pupil plane and the image plane, the field of view (in the image plane), determined by the pupil-plane pixel sampling, is $[\lambda/0.02]^2 \approx 4.4'' \times 4.4''$ arcsec^2 at 430.5 nm. As the atmospherically induced pupil-plane phase perturbations are independent of the wavelength, λ becomes an independent parameter in our simulations. However, for the purpose of choosing the field of view, we have chosen the wavelength to be 430.5 nm. This also means that the r_0 values used in our simulations correspond to 430.5 nm.

5.3 Validation

We checked the veracity of our simulation procedure and the results for cases in which they could be obtained with analytical expressions, in two distinct ways. First, from theory, we know the exact analytical expressions for average seeing-limited long-exposure and tilt-corrected short-exposure transfer functions (Equations 1.9 and 1.15, respectively). We could reproduce these and compare them with the corresponding transfer functions we obtained using our simulations.

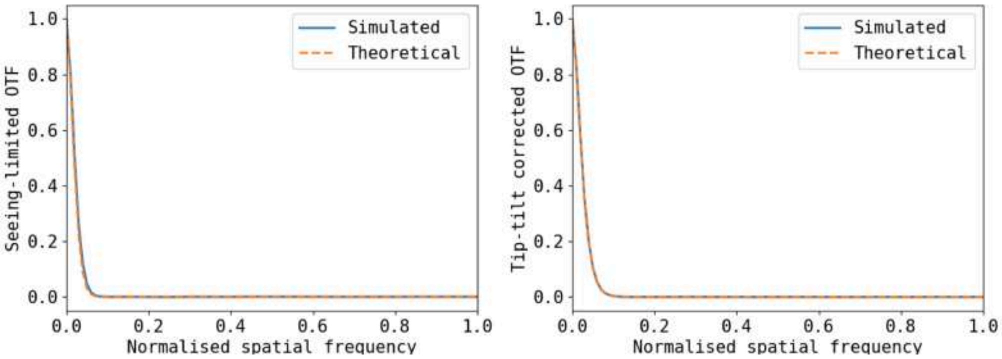

Figure 5.3: Plots of the long-exposure OTF for seeing-limited (left figure) and tip-tilt corrected (right figure) cases. The blue solid curves are from the simulation and the orange dashed curves are from the theoretical expressions.

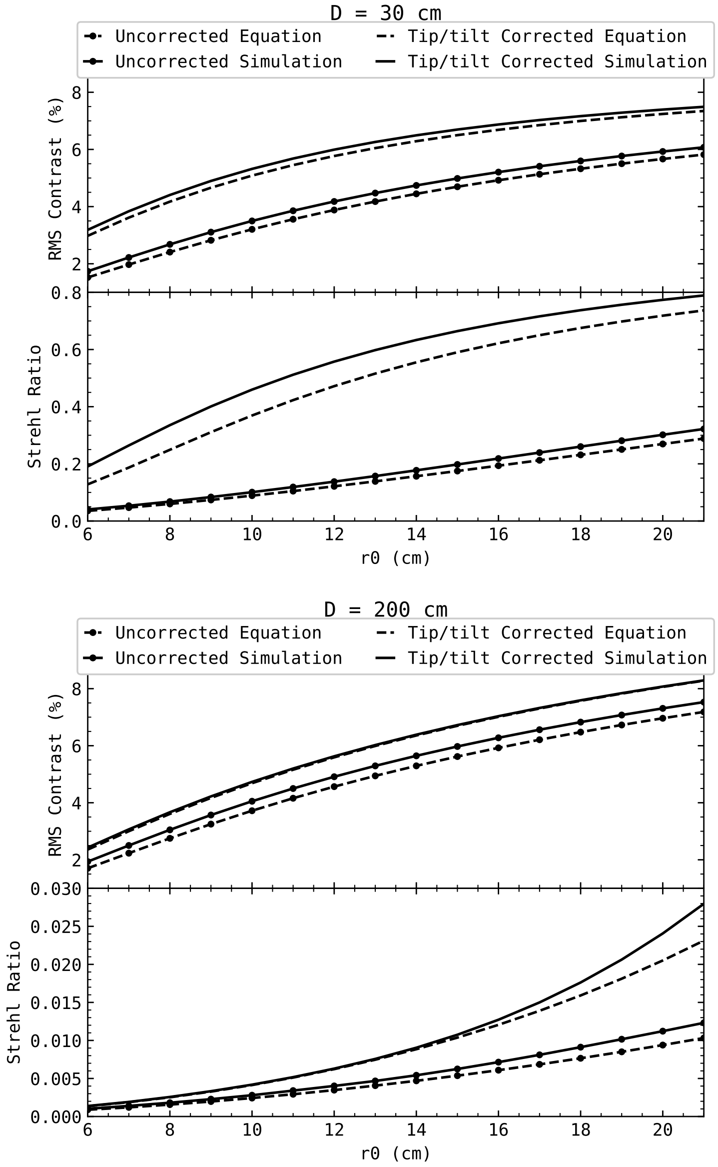

Figure 5.4: Rms Contrast and Strehl ratio as a function of r_0 for two values of the diameter (30 and 200 cm). The circular marked and unmarked curves are for the uncorrected (seeing-limited) and tip-tilt corrected (image stabilized) values, respectively. The values obtained from the analytical expressions of the transfer function are shown by the dashed curves, and those from the simulation are shown by the solid curves.

Figure 5.3 shows the long exposure OTF for the seeing-limited and tip-tilt corrected cases in the left and right plots respectively. The solid blue curves are obtained using the simulations and the dashed orange curves are from the analytical expressions. For these simulations the diameter of the telescope was assumed to be 200 cm with an r_0 of 10 cm. We can see a good match between the curves obtained using the analytical expression and those from the simulations.

Further, we estimated the Strehl ratio as the ratio of the volume under the transfer functions to that of the ideal diffraction-limited transfer functions both for uncorrected (seeing-limited) and tip/tilt corrected cases. We know that for a large telescope ($D \gg r_0$), under seeing-limited imaging conditions, the Strehl ratio can be approximated as $(r_0/D)^2$. We found that our simulated Strehl values were in good match with the theoretical values. The bottom panels of Figure 5.4 show the Strehl ratios derived from the analytical expressions for the transfer functions and the simulations for two telescope diameter values. We see that (a) the values are close to what is to be expected, and (b) the Strehl values derived from the simulation are always slightly higher than that predicted by the theory. We already know that the theoretical expressions for average short exposure transfer functions are overestimated at high spatial frequencies as they are derived under the assumption that there is no correlation between the tilt and high order wavefront perturbations (J. Y. Wang, 1977; Lutomirski, Woodie, and Buser, 1977).

The top panels of Figure 5.4 show the rms granulation contrast estimated as a function of r_0 with the simulated long and short exposure transfer functions for two representative cases of diameters (30 cm and 200 cm). The corresponding values estimated using the analytical expressions of long and short exposure transfer functions are overplotted. We find that the rms contrast estimated from our simulations closely follows that expected from the analytical expressions of the transfer functions.

Further, we decomposed the atmospheric phase perturbations over the pupil into a finite number of Zernike polynomials and found that the residual phase variance after compensating for a certain number of Zernike terms is always slightly less than the corresponding theoretical value predicted by Noll (1976) (Equation 1.14).

This validates our simulation procedure and allows us to estimate the rms contrast for high-order phase compensated images where there are no analytical expressions available.

5.4 Results

5.4.1 Seeing-limited Imaging

Figure 5.5 shows the rms contrast as a function of r_0 for different telescope sizes under seeing-limited imaging. We find that it varies between 1.8 and 7.6%. It increases with r_0 as expected. It has a slight dependence on the telescope diameter as well; the larger the diameter, the higher the rms contrast, for a given r_0.

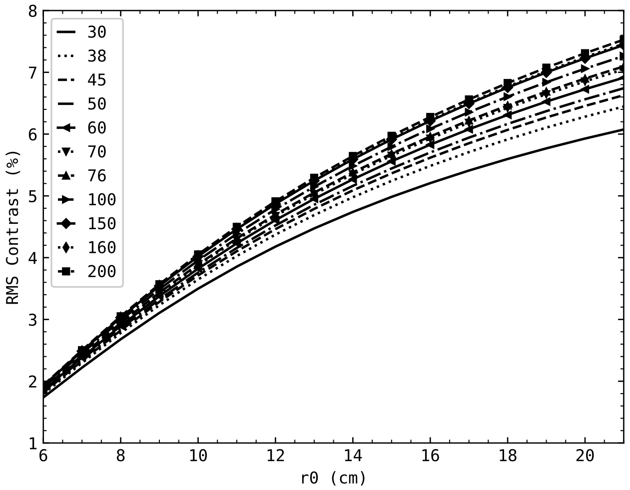

Figure 5.5: Rms contrast vs Fried's parameter r_0 under seeing-limited imaging conditions where the markers represent the values of diameter (in cm) as shown in the legend.

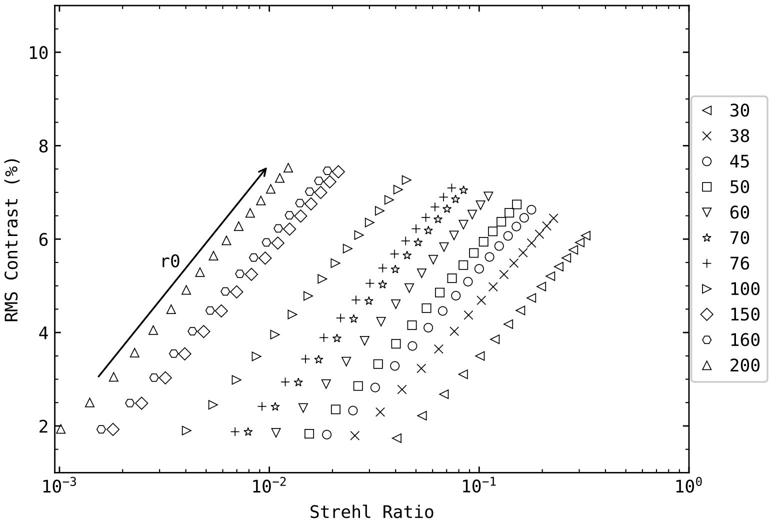

Figure 5.6: Rms contrast vs Strehl ratio under seeing-limited imaging conditions. The markers correspond to different telescope diameters (in cm), as shown in the legend, and the direction of increasing r_0 is along the arrow ranging from 6 to 21 cm in steps of unity.

Figure 5.6 shows a semi-logarithmic plot of rms contrast as a function of Strehl ratio. The

Strehl ratio spans over three orders of magnitude as D/r_0 changes from 1 to 33. However, the rms contrast changes by less than an order of magnitude for the same range of D/r_0. This is perhaps due to the intrinsically low contrast nature of the solar granulation. This plot helps us to specify the contrast of the solar granulation as metric for solar telescopes against the traditional Strehl ratio (which cannot be measured) for seeing-limited imaging. Conversely, it could also be used to estimate the efficiency of the telescope under seeing-limited imaging conditions (by comparing the observed contrast with the theoretical upper limit presented here).

5.4.2 Stabilized Imaging

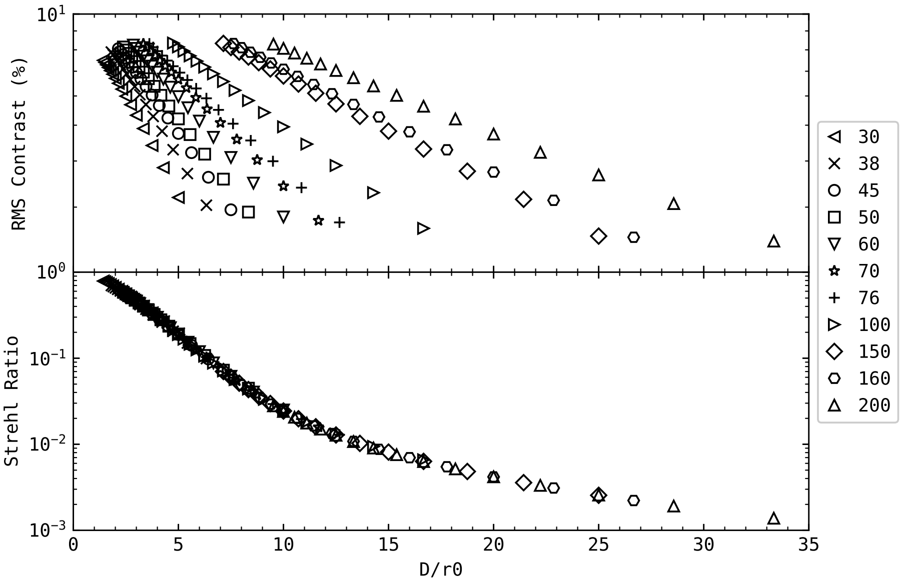

Figure 5.7: Rms contrast and Strehl ratio vs D/r_0 for stabilized imaging case. The markers represent different telescope diameters (in cm) as shown in the legend.

The first order adaptive optics compensation is to stabilize the image by arresting or mitigating its random motion at kHz rate. It is equivalent to removing the 2D tilt in the atmospherically induced phase perturbations. The top and bottom panels of Figure 5.7 indicate the rms contrast and Strehl ratio after compensating for the fast varying wavefront tilt as a function of D/r_0. We observe that:

a) The Strehl ratio is a monotonically decreasing function of D/r_0. It rapidly decreases when $D/r_0 \leq 10$ but decreases relatively slowly when $D/r_0 > 10$.

b) The rms contrast is a non-monotonic function. It is highly dependent on the actual telescope diameter. The rate of enhancement of rms contrast with r_0 (seeing) is more rapid for small and intermediate-size telescopes than for large telescopes.

5.4.3 Imaging with AO correction

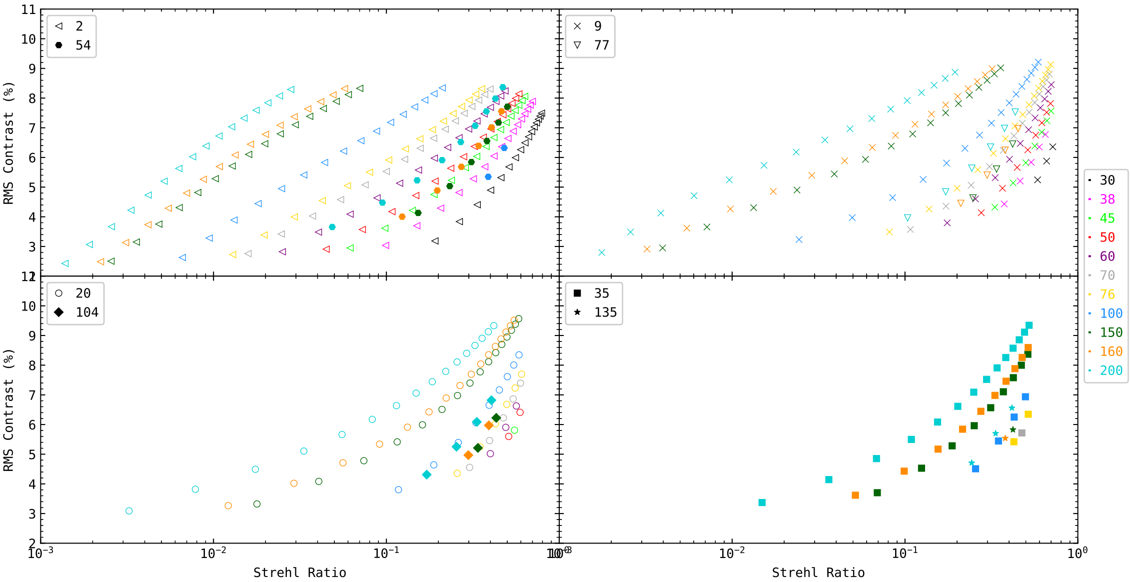

Figure 5.8: Rms contrast vs Strehl ratio for different telescope diameters and r_0 after AO correction. Each marker represents a unique value of N_Z (shown on top left corner of the respective plots) and each colour represents a unique value of telescope diameter (shown on the right of the plots).

The four panels of Figure 5.8 show semi-logarithmic plots of rms contrast versus the Strehl ratio after AO correction. We note that the linear-log relation that existed before AO correction no longer exists. From the figure legends, we can identify N_z and D as the marker shape and color respectively. For example, cyan corresponds to a 200 cm telescope and triangles and squares correspond to 2 and 35 terms corrected, respectively. r_0 can be found by tracing the plots along a given D and N_Z. For example, the cyan triangle curve in the top left panel is made up of 16 points with the lowest data point corresponding to r_0 of 6 cm and the highest data point corresponding to r_0 of 21 cm. So, for each successive point, the value of Fried's parameter increases in steps of unity. However, when we trace the cyan squares curve on the bottom right panel, we see that the maximum value of r_0 is only 19 cm. This is because we terminated the simulations for the cases where the phase variance was lesser than 1 radian^2 (Section 5.2.3.2). The "missing" r_0 = 20 and 21 cm points imply that the phase variance for that D and r_0 in the previous value of N_Z (= 19) was less than 1 radian^2. The two red circles on the bottom left panel implies that for a 50 cm telescope, the mean square phase variance reduces to less than 1 radian^2 after correcting just 20 terms at r_0 = 7 cm; this yields corresponding Strehl and rms contrast as 0.6 and 6.5% respectively at r_0 = 7 cm. A 2 m class telescope will require compensation of up to 135 terms to bring the phase variance below 1 radian^2 at r_0 = 8 cm (blue stars on the bottom right panel). Other data points can be interpreted in a similar way.

In general, for small telescopes, both the Strehl ratio and the rms contrast increase (clustering near top right corner of the plots) with AO correction. However, for large telescopes, the increase is rather slow. Here again, this plot is quite useful to specify the granulation contrast as a metric after AO correction as against the traditional Strehl ratio.

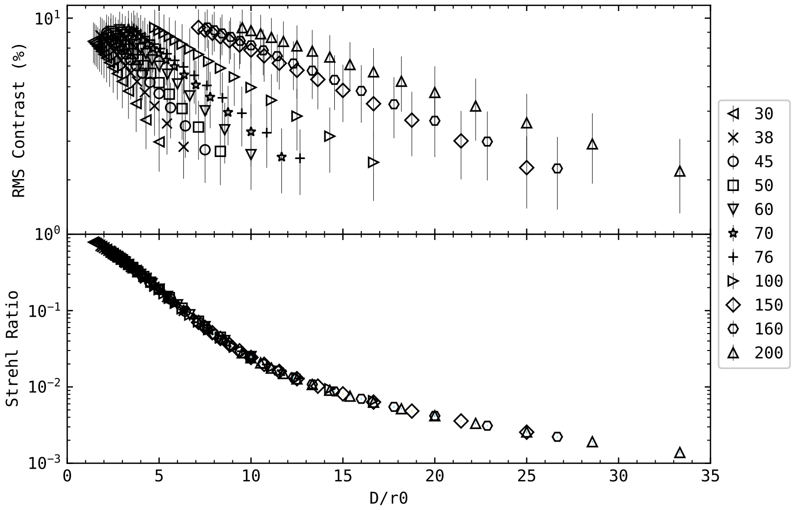

Figure 5.9: Rms contrast and Strehl ratio vs D/r_0 for stabilized imaging case similar to Figure 5.7 with the error bars representing the spread in values expected with change in scene.

5.4.4 Scene Dependency

The rms granulation contrast is a function of the solar granulation scene that is being observed. At large enough fields-of-view, this variation will not be high. We find a change in the intrinsic contrast with a change in region since we are using high-resolution images covering a very small field of view. So, we have repeated the entire simulation for 10 different solar regions following the method described in Section 5.2.4 and obtained the mean and standard deviation of rms granulation contrast.

Figure 5.9 is similar to Figure 5.7 showing the variation of rms contrast and Strehl ratio with D/r_0 for various telescope diameters. It can be seen from the top panel that the rms contrast can vary by up to 1 % above and below the mean value. However, the Strehl is independent of scene (it depends only the transfer function of the telescope). Similarly, Figures 5.8 and 5.10 are comparable but for the difference due to error bars arising from scene dependency.

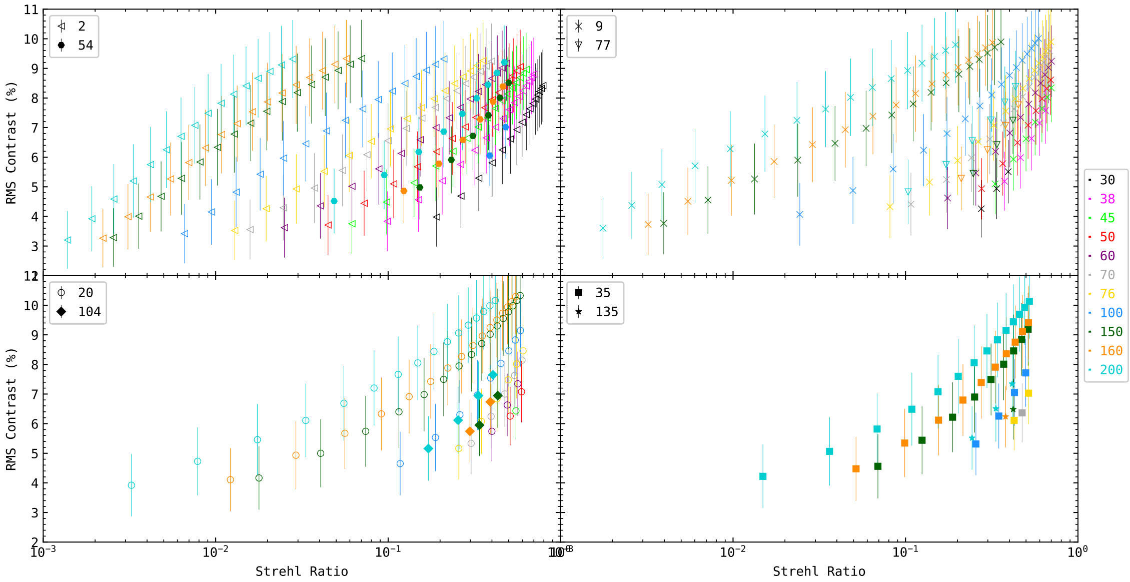

Figure 5.10: Rms contrast vs Strehl ratio similar to Figure 5.8 with the error bars corresponding to the deviation from mean value that can be expected when the scene of observation is changed.

5.4.5 Wavelength Dependency

As we already know the atmospheric path-length perturbations are achromatic. However, the wavelength dependency enters our simulations through the specifications of the Fried's parameter r_0. Although we have used the shortest wavelength $\lambda = 430.5$ nm, our results for a longer wavelength can be easily obtained by changing the input r_0 according to its wavelength dependency of $\lambda^{1.2}$. We have verified this through simulations as shown in Table 5.1. It can be seen that at long wavelengths, Fried's parameter is high, and therefore, the contrast is high (even though the intrinsic contrast of the granulation is lower at longer wavelengths).

Table 5.1: Comparison of the rms contrast and Strehl ratios for a 200 cm telescope when the simulations were run for two different wavelengths (λ = 430.5 nm and 860 nm). If we consider an r_0 of 7 cm at 430.5 nm, this corresponds to an r_0 of 16 cm at 860 nm.

No.	N_z	**λ = 430.5 nm, r_0 = 7 cm**		**λ = 860 nm, r_0 = 16 cm**	
		Rms Contrast %	**Strehl Ratio**	**Rms Contrast %**	**Strehl Ratio**
1	0	2.502	0.0013	4.252	0.0071
2	2	3.066	0.0019	5.180	0.0127
3	9	3.486	0.0025	5.964	0.0826
4	20	3.819	0.0078	6.673	0.2563
5	35	4.144	0.0362	7.415	0.4219

5.4.6 Limitations of the Simulations

The results of our simulations, particularly those with AO corrections, correspond to ideal conditions. We have ignored the finite size of the wavefront sensor and corrector elements. We have also ignored the finite temporal delay that occurs in real systems. Thus, our results are only indicative of an upper limit on the contrast and the Strehl ratios. In what follows (Section 5.4.7), we compare the Strehl ratio and rms contrast obtained through our simulations with that obtained with real solar adaptive optics systems and thus derive an efficiency parameter. We then propose to use this efficiency parameter, along with the upper limits obtained through our idealistic simulations, to specify the expected Strehl ratio and, hence, the rms granulation contrast measured by future solar telescopes. A caveat in this argument is that a certain degree of efficiency in the domain of the Strehl ratio need not translate to the same degree of efficiency in the rms contrast, owing to the non-linear relationship between the Strehl ratio and rms contrast after AO correction. Scharmer, Löfdahl, van Werkhoven, et al. (2010) have reported an apparent efficiency factor of 54% in the rms solar granulation contrast after a low order ($\approx$ 30 modes) AO correction for a 1 m telescope (factor 1.85 mentioned in Figure 5). It implies that for a larger telescope, a similar efficiency might be achieved with a high order AO correction. It is clear that more data is required to get a better idea of if and how these parameters will affect efficiency. Nevertheless, we can assume at least 50% efficiency in the rms contrast and use our results as a lower bound on the contrast to be expected.

Another limitation of our simulations is that we have assumed Kolmogorov-type turbulence. In reality, the outer scale length could be finite, and this would lead to a slightly better resolution (Tokovinin, 2002; Martinez et al., 2010). It is also known that the residual variances after compensation of a few low-order Zernike terms are lower than that predicted by the Kolmogorov turbulence even when the outer scale is 10 times larger than the aperture diameter (Winker, 1991). Thus, real systems could be better than what is predicted based on Kolmogorov turbulence. In the same vein, metrics like the Strehl ratio and rms contrast could also be higher and better respectively.

5.4.7 Efficiency of Real AO Systems

We could glean the Strehl ratio obtained with three practical solar AO systems. The first system was that of the 70 cm Vaccum Tower Telescope (VTT) (Berkefeld et al. (2012)). Here, the residual variance of the corrected modes, uncorrected modes, and wavefront sensor (WFS) errors are added to determine the Strehl (Table 5.2 - rows 1 to 6).

Table 5.2: Comparison of our simulated with practical Strehl values reported by solar observatories. The 70 cm VTT, 76 cm DST, and 100 cm NVST had published Strehl values of their AO systems (for the method of calculation, see text). Simulations were carried out for these telescopes with appropriate r_0 and N_z and compared to the published values to derive an efficiency factor. Here, 'Dia' refers to the telescope diameter.

No.	**Dia**	N_z	**Our Simulated**		**Practical**		**Efficiency**
			r_0	**Strehl**	r_0	**Strehl**	$\frac{\textbf{Our Simulated}}{\textbf{Practical}}$
	(cm)		**(cm)**		**(cm)**		
1	70	27	9	0.622088	8.8	0.275	0.442
2	70	27	11	0.711601	11	0.3	0.421
3	70	27	13	0.772764	12.5	0.37	0.478
4	70	27	15	0.816114	15	0.42	0.515
5	70	27	17	0.847887	17	0.45	0.531
6	70	27	19	0.871858	19	0.46	0.528
7	76	80	6	0.662532	5.4	0.46	0.694
8	76	80	17	0.92989	16.5	0.88	0.946
9	76	15	25	0.847131	25	0.8	0.944
10	76	20	9	0.497198	8.6	0.4	0.804
11	100	65	7	0.536508	7	0.55-0.65	1.025 - 1.216
12	100	65	8	0.607205	8	0.6-0.7	0.988 - 1.153
13	100	65	9	0.663494	9	0.68-0.72	1.025 - 1.085
14	100	65	10	0.708692	10	0.75	1.058
15	100	65	11	0.745375	11	0.77	1.033

The second system was the 76 cm Dunn Solar Telescope (DST). The Strehl values were estimated using three different methods. In the first method, a quasi-long-exposure point spread function was estimated using the wavefront error (Marino and T. Rimmele, 2010). The corresponding optical transfer function was expressed as the product of three transfer functions and estimated appropriately. Finally, the Strehl ratio was estimated from the optical transfer function. These values are listed in Table 5.2 rows 7 and 8. The efficiency here seems to be high (compared to the German VTT case), especially for the larger r_0 case. One possible explanation for this is the saturation of Strehl values with an increase in N_z. For r_0 = 17 cm, it was found through our simulations that correcting for 35 terms itself will result in a Strehl of 0.86. So we are not considering such cases of extremely good seeing in calculating the efficiency. This is because we are attempting to fit the error budget of the AO system into a single efficiency parameter with the assumption that the fitting error is the major contributor. For moderate seeing cases, our method works well and yields results that are comparable with practical efficiency values. Under very good seeing conditions, it would be better to carefully model the behaviors of the various components of each AO system (temporal bandwidth of the AO system, etc...). However, that is beyond the scope of our current work as our aim with these simulations was to arrive at the theoretical upper limits of rms contrast and Strehl ratio for most existing and planned solar telescopes. Nevertheless, our efficiency parameter can be a useful tool in determining the performance of solar AO systems to the first degree for poor to moderate seeing conditions. Simulations that emulate the performance of any specific AO system and have a comprehensive error budget can be the next step to better understand the system performance.

In the second method, the Strehl (Table 5.2 - row 10) was determined by extracting the wavefront error information after processing the AO corrected image using phase diversity method (T. R. Rimmele, 2000). Here again, the apparent high efficiency could be attributed to the combination of AO correction and image post-processing, and thus, we exclude this case as well. Also, the values are taken from a figure in the paper. The figure only displays the best 20 out of every 100 frames. This could be another reason for high Strehl. In the third method, the residual errors from SHWFS were used to determine the Strehl (Table 5.2 - row 9). Here again, as stated in T. R. Rimmele (2000), the Strehl ratios are overestimated as the contribution of higher order modes (not detected by the SHWFS) is not taken into account.

The third system that was considered was the AO system of the 1 m New Vacuum Solar Telescope (NVST) at the Fuxian Solar Observatory in China (C. Rao et al., 2016). They added the residual error of low-order corrected modes, high-order uncorrected modes, and aliasing errors to estimate the total wavefront error. Following this, they used the expression from R. R. Parenti and Sasiela (1994) to estimate the short exposure Strehl ratio (see table 5.2 rows 11 - 15). The values predicted by our simulations are lower than the values reported by them. Understandably, it is not a fair comparison because we estimate Strehl ratios from long-exposure images.

In summary, we find that the efficiency obtained from the VTT is likely to be unbiased, and thus, we can possibly conclude that the efficiency of practical solar AO systems is likely to be in the range of 40 to 55%.

Chapter 6

Conclusions

> *"I'm comfortable with the unknown – that's the point of science. There are places out there, billions of places out there, that we know nothing about. And the fact that we know nothing about them excites me, and I want to go out and find out about them. And that's what science is. So I think if you're not comfortable with the unknown, then it's difficult to be a scientist... I don't need an answer. I don't need answers to everything. I want to have answers to find."*
>
> *Brian Cox*

6.1 Summary

With the construction of ever increasingly large-aperture telescopes, AO has become essential at all ground-based observatories. Due to the heating of the ground by the radiation from the Sun, AO in the daytime is of paramount importance if the full potential of these large telescopes is to be realised.

Therefore, the main focus of this thesis was to contribute to the solar AO program at IIA which ultimately aims to demonstrate AO/MCAO on KTT and generate expertise in the field. The first step for demonstrating MCAO is the identification of the strongest layer of turbulence above the observatory. This was done with two near-simultaneous experiments at KO which helped us measure the C_N^2 profile for the first time in the observatory's 125 year history. Following this, we have also established a new method to estimate the isoplanatic angle during the daytime from seeing-limited images. This thesis also covers the first SCAO and MCAO systems that were designed for KTT. Finally, we have used Python simulations to estimate the rms granulation contrast as a metric for quantifying the performance of solar telescopes and AO systems. A more detailed chapter-wise summary is given below.

6.1.1 Chapter 2

We have used the S-DIMM+ method and a balloon-borne array of temperature sensors to measure the high-altitude and near-Earth turbulence, respectively, at Kodaikanal Observatory. While validating the performance of the former method for our system parameters through extensive simulations, we have tested the primary assumptions in the principle of this method. We have also experimentally established that even a single small telescope can be used to measure the turbulence strength up to a height of 5 - 6 km. This helped us identify a strong layer of turbulence about 3 km above the telescope site. When designing the experiment, we opted to record the lenslet array data at two wavelengths. One at 540 nm and other at H-α. The former was chosen as the white-light contrast of solar images is highest near 540 nm. H-α was chosen to enable observations of bright facular points (Rengaswamy, 2001). Our results also show that the estimation of C_N^2 is independent of the solar scene or wavelength of observation. This is consistent with the fact the atmosphere phase perturbations are achromatic.

The balloon-measurements for near-Earth turbulence have been successful and have a reasonable match to the profile predicted by Hufnagel (modified for daytime). The results from the balloon-measurements were also consistent with earlier studies of seeing (Rengaswamy, 2016). We have opted for a very simple set-up that has only one electronics set-up for all 7 sensors. A set-up with a different electronics for each sensor would allow simultaneous reading of the sensor data but would also be bulkier, more expensive and more complex to calibrate. The trade-off here is for a simpler and more compact set-up with some time delay between the different sensor readings. Since the maximum delay between the data recorded by two sensors (70 ms) is much smaller than the duration over which the data are averaged (almost 1 min), we do not believe that it will significantly affect our results.

We have used two different methods to estimate the C_N^2 profile for the first time at Kodaikanal Observatory in its 125 years of operation. Furthermore, from Figures 2.18 (a), 2.16 and 2.17, we can see that the order of magnitude of the C_N^2 profile values from the two experiments also match. These experiments can be repeated, in principle, at any other site to understand the turbulence strength profile there.

6.1.2 Chapter 3

We have extended the PSM algorithm to estimate the isoplanatic angle during the day-time using long-exposure seeing-limited images of the Sun. For the data recorded using the 20 cm H-α telescope at Merak in April and June 2018, we found the isoplanatic angle (for long-exposure seeing-limited) to be around 15 - 20 $''$.

6.1.3 Chapter 4

We have designed and set-up an SCAO system in the laboratory. Some preliminary work on the control software including the reading of the data from the WFS camera, the code for image motion estimation (and optional parabolic interpolation) using two different algorithms (see Appendix A) have been completed. An alternate SCAO set-up that can overcome the limitations of the existing hardware has also been designed. Finally, an MCAO system that uses the results from the first turbulence profiling campaign has also been designed.

6.1.4 Chapter 5

We have estimated, through extensive computer simulations, the rms contrast of the solar granulation to be expected from a large ground-based telescope without and with AO correction. Our simulations indicate 4% rms granulation contrast at r_0 = 10 cm (at λ = 430.5 nm) and 0.3% Strehl ratio for a 2 m class telescope under seeing-limited imaging. The rms contrast increases to 4.5% and the Strehl to 0.4% after image stabilization. A high order AO system with compensation equivalent to that of about 100 Zernike modes will be required to achieve a Strehl ratio of about 40% and a rms granulation contrast of 7.5% under similar atmospheric conditions. We have compared our results with the existing solar AO systems and derived a possible efficiency of about 40 to 55% for Strehl ratios.

Although this efficiency could not be directly translated and used for obtaining observable rms granulation contrast, a similar value could be used to obtain the rms contrast to be expected from real systems in conjunction with the contrast predicted by our idealistic simulations for providing a lower bound (minimum value). Thus, our results could be quite helpful, to specify the image quality requirements for future large telescopes.

6.2 Novelty of thesis

The novel aspects of this thesis are:

- **Turbulence profiling:** The results from the two experiments (S-DIMM+ and balloon-measurements) carried out to measure the C_N^2 profile during the daytime are the first to measure the daytime vertical distribution of turbulence strength in the country. Both instruments were fully designed and developed in-house. The simulation code in Python, which includes the generation of multi-layer atmospheric turbulence, to understand and validate the performance of the S-DIMM+ instrument and the inversion code that estimates the turbulence strength profile from a series of SHWFS frames were developed from scratch by us. The code to analyse the data from the temperature sensors used in the balloon-measurements were also developed by us.

- **Isoplanatic angle measurements:** We are the first to propose and implement a technique to estimate the isoplanatic angle during the daytime using long-exposure seeing-limited images. It can be applied to solar images recorded using any ground-based telescope. Since most observatories have small solar telescopes that are used to monitor solar activity routinely, the large volume of data from them can be exploited to study and understand the evolution of turbulence (in terms of the r_0 and isoplanatic angle) over long timescales.

- **SCAO/MCAO designs for KTT:** We have designed the first SCAO and MCAO systems for KTT. The MCAO design is the first solar MCAO design from the country.

- **Image quality specification study:** We developed our simulation code in Python for the image quality study. This study of using rms granulation contrast as a metric to quantify the performance of solar telescopes and AO systems is the first comprehensive study that includes most existing (and some planned) ground-based solar telescopes. We have also reported the contrasts that one must obtain under ideal diffraction-limited or seeing-limited conditions. This is particularly useful when specifying the desired performance to vendors that supply the telescopes.

6.3 Future Work

Turbulence profiling

The C_N^2 profiles estimated from the S-DIMM+ and balloon-measurements were from three days of data obtained in January 2024. Further measurements can be carried out to understand the evolution of turbulence as a function of diurnal and seasonal variations. A larger dataset will also help us achieve a statistically significant result. The S-DIMM+ method can be repeated with a wide-field WFS; this will allow us to increase the sensitivity of the instrument beyond 6 km. However, F. Roddier (1981) suggests that the C_N^2 profiles beyond 4 km above the mean sea-level must be constant at different locations as the effect of local orographic disturbances is lost. If this is true, the measurements we have made are sufficient and we do not need to have knowledge of the C_N^2 profile at higher heights.

One problem we encountered with the balloon-measurements was the slating of the balloon due to wind. We have ignored the effect of this in the present analysis. This causes an error in the height measurement. If a drone is used in the place of the balloon, this effect can be alleviated. The balloon-measurements can also be used to identify the height of future ground-based solar telescopes like the National Large Solar Telescope (NLST) (Singh, 2008).

Isoplanatic angle measurements

The method of estimating the isoplanatic angle using long-exposure solar images can be repeated for the data obtained at any observatory. The results can also be compared to θ_0 estimates from other techniques like S-DIMM+ or balloon-measurements (combined with Equation 1.8). There is also scope to extend this method to obtain an analytical estimate of the C_N^2 profile during the daytime. This is briefly discussed in Appendix E.

SCAO/MCAO designs

The first SCAO set-up for KTT has been set-up in the lab and the code for the WFS have been completed. Once the DM performance is characterised and the control code for it have been developed, the system can be tested on-sky. The same control code can then be used for the MCAO loop as well as the current plan is to allow the two loops to run independently.

While developing the code for the WFS for SCAO (a) we identified that we are currently limited by the speed of the WFS camera. This was the motivation for SCAO (b) design. In the future, when the AO system is deployed at the telescope, both SCAO (a) and (b) configurations can be made available for use based the seeing conditions. SCAO (a) offers coarser correction due to sparser sampling of the pupil and can be used at times of poor seeing. SCAO (b) can offer better correction and can be used at times of better seeing. We also anticipate the scattering of light inside KTT to make initial alignments of the AO system tricky.

Image quality specification

The performance characterization simulations can be repeated for von Karman type of turbulence to see the effect(s) it can have on the contrast estimates, if any. Due to computational constraint we have not performed the simulations for DKIST or EST. The performance evaluation of these systems can also be carried out. Once the SCAO system for KTT has been tested on-sky, its performance can also be characterized using the results from our image quality simulations.

Appendix A

Image motion estimation algorithms

One of the crucial steps in solar AO systems is to estimate the image motion between two images. It can be the image motion in the correlation camera which will be used to control the tip-tilt mirror or the image motion between various sub-aperture images in the SHWFS. In the absence of any wavefront perturbations, all the lenslets produce identical images. However due to the perturbations introduced by the atmosphere, the images are shifted with respect to each other. In stellar AO systems that work based on SHWFS, the image shift can be found using a simple centroiding algorithm to find the center of the PSF produced by each lenslet. When we have an extended object like the Sun, different algorithms must be used. There are many algorithms for estimating the image shifts (Löfdahl, 2010) for extended sources.

We have explored two of them. The first one is called Sum of Absolute Differences (SAD) and it works in the image domain. Let image 1 and image 2 be the two images between which the image motion must be estimated. Both images are of size N×N.

Steps for estimating image motion using SAD:

- The central M×M (where $M < N$) of image 1 cropped and considered for analysis.
- The sum of the pixel-to-pixel difference between the selected M×M region of image 1 and an M×M region of image 2 is estimated.
- The previous step is repeated until all possible M×M regions of image 2 are covered by moving the selected M×M region of image 1 across. The sum is noted at each position.
- The position of the least sum corresponds to the shift of image 1 with respect to image 2.

The maximum shift that can be measured by the SAD algorithm is determined by the size of the cropped region and is $\pm(\frac{N}{2} - \frac{M}{2})$ pixels (assuming that the central M×M region of one of the images is cropped for analysis). However, computationally this method is more intensive as it involves shifting the M×M region of image 1 to $(\frac{N}{2} - \frac{M}{2})\times(\frac{N}{2} - \frac{M}{2})$ unique positions, computing the element-by-element difference and the sum at each position. A possible solution to reduce the computational load is to minimise the locations to which the M×M region is shifted. One technique would be to first estimate a coarse value of image shift (by first identifying only quadrant to which image is shifted which requires only 4 computations) and then obtain a finer estimate within the quadrant. Alternatively, equations 2.1 and 2.2 can be used to estimate the expected image motion for the system and site parameters. This can be converted to the pixel range over which image motion values are likely to fall. Then, a threshold can be set such that computations at all $(\frac{N}{2} - \frac{M}{2}) \times (\frac{N}{2} - \frac{M}{2})$ need not be calculated. The trade-off in this technique is the possibility of underestimating the shift at instances of very poor seeing.

The second method we considered is called Fourier Cross Correlation (FCC) and it works in the Fourier domain. Steps for estimating image motion using FCC:

- The Fourier transforms of the two images are found as FT1 and FT2.
- Using the properties of the Fourier transform, it can be shown that a shift in the image domain manifests as a phase term in the Fourier domain. Then, the product of FT1 and the complex conjugate of FT2 is computed.
- The inverse Fourier transform of the product produces a peak corresponding to the shift of image 1 with respect to image 2.

In the FCC method the maximum shift that can be estimated is $\pm\frac{N}{2}$ pixels. Computationally, it can be faster than the SAD algorithm, particularly for larger images.

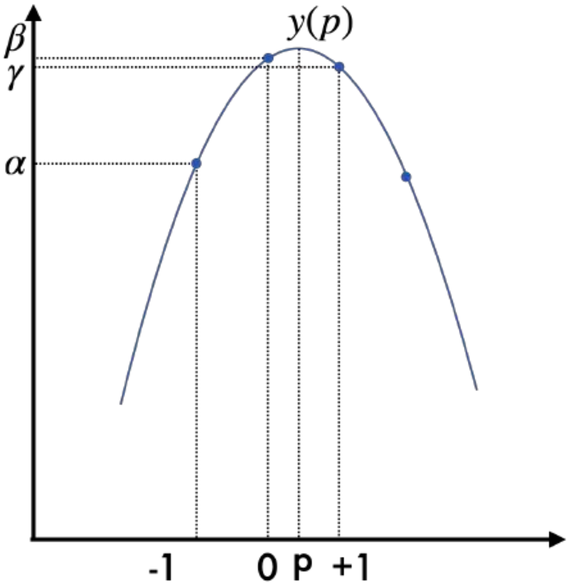

Figure A.1: Representative parabolic curve fitted to data to be used for interpolation which allows image shift measurements with sub-pixel accuracy.

The accuracy of SAD and FCC method is 1 pixel. It can be further improved by opting for interpolation algorithms. It must be kept in mind that in SAD the interpolation is around the minimum and in FCC it is around the maximum. We have combined FCC with an interpolation algorithm that fits a parabola to the data points. Consider Figure A.1. The blue parabolic curve represents the function on which the interpolation is to be done. The blue circular markers represent the data points. Let the maximum value that we estimate from the FCC method be β and the position be marked as zero. Similarly the values of the points just before and after the maximum are α and γ, respectively. The pixels are assigned -1 and +1. The true maximum value is $y(p)$ and the corresponding coordinate is p. The general form of a parabola can be written as:

$$y(x) \overset{\Delta}{=} a(x-p)^2 + b \tag{A.1}$$

Substituting x as -1, 0, +1 and p and $y(x)$ as α, β, γ, and $y(p)$ in equation A.1 respectively, four equations are formed. They can be reduced to the expression:

$$p = \frac{1}{2}\left[\frac{\alpha-\gamma}{\alpha-2\beta+\gamma}\right] \tag{A.2}$$

This example is shown in one dimension. It can be applied equivalently to the other direction as well. It allows to estimate the pixel shift with one-tenth of a pixel accuracy.

Appendix B

Fried's integral for image motion

The equation given by Fried (1975) for image motion is:

$$I(S,\psi) = \left(\frac{16}{\pi}\right)^2 \int_0^{2\pi} d\theta \int_0^1 du\, u \left\{ \frac{1}{8} cos^{-1} u + \left(1-u^2\right)^{1/2} \left[\left(u^3/12 - 5u/24\right) + \left(u^3/3 - u/3\right) cos^2\theta\right] \right\} \left\{ \left[S^2 + 2Sucos(\theta+\psi) + u^2\right]^{5/6} + \left[S^2 - 2Sucos(\theta+\psi) + u^2\right]^{5/6} - 2u^{5/3} \right\}, \tag{B.1}$$

where S is the normalised separation between the sub-apertures ($S = s/D$, where s is the separation between the sub-apertures and D is the diameter of the sub-apertures). ψ is the angle between the line connecting the sub-apertures and the line along which image motion is being estimated. For example, for longitudinal and transverse cases, $\psi = 0$ and 90°, respectively. θ is the angle between u and the x-axis (which is at an angle ψ from the line joining the sub-aperture centers).

It was noted by Scharmer and van Werkhoven (2010) that the values derived for the longitudinal and transverse image motions (given in Table 1 of Fried (1975)) when the ratio of the sub-aperture separation (s) to their diameters (D) was greater than 10 were not accurate. We verified this by estimating the image motion values given by the equation I using simulations in Python and comparing it with the values from Table 1 in Fried (1975).

Figure B.1 shows the percentage error in Fried's calculations as a function of s/D. The error is estimated as the difference of the value calculated by us through simulations and the value by Fried normalised by the value calculated by Fried. The values given in Fried (1975) are consistently underestimated with the error reaching almost 10% when s/D is close to 10 (also reported in Scharmer and van Werkhoven (2010)). We have used a step size of 0.001 for u and of 0.01 for θ in our numerical integration simulations. We fixed these as the sampling values while generating the F_x and F_y (Equations 2.10 and 2.11) matrices for the inversions.

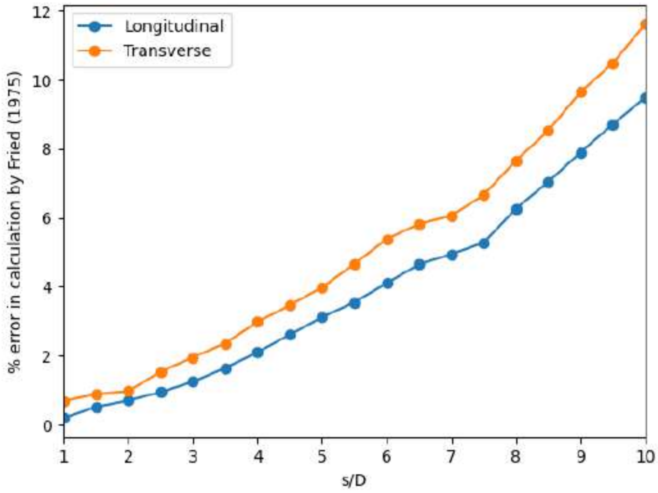

Figure B.1: The percentage error in the calculations of Fried for longitudinal (blue curve) and transverse (orange curve) image motion measurements as a function of the sub-aperture separation normalised to the sub-aperture diameter (s/D).

Figure B.2 shows the longitudinal covariance matrix (F_x) obtained with our system parameters at 0 km height. The left matrix is obtained using Equation 2.10. The right matrix is obtained by using Sarazin and Rodiier's approximation of image motion (Equation 2.1) instead of using Fried's equation (Equation B.1). The difference between the two is shown in Figure B.4 left map.

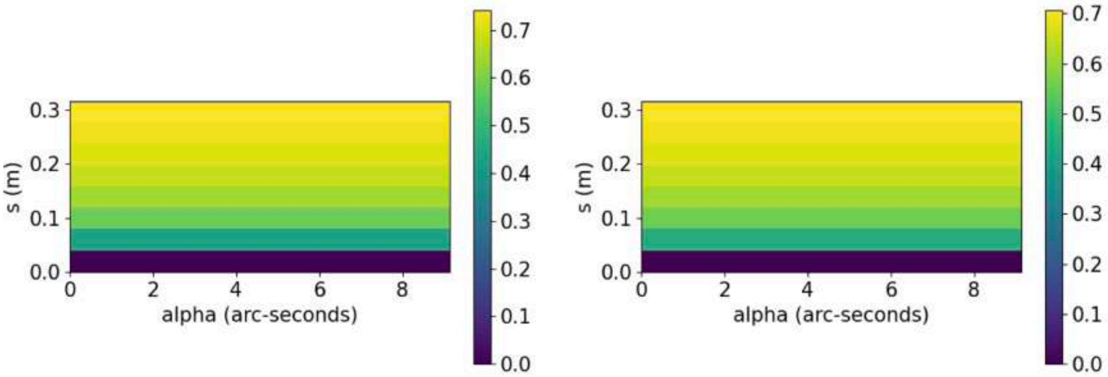

Figure B.2: Maps of the longitudinal covariance matrices at 0 km height with our system parameters. The left map was estimated by using Fried's equation for image motion and the right map used Sarazin and Roddier's equation for image motion.

Similarly, the plots of the longitudinal covariance matrices for our system parameters but at 6 km layer generated using the two equations are shown in Figure B.3. The difference in the two matrices is more apparent in this case. The difference map is shown in Figure B.4 (right). For the 6 km case, we can see that the difference in the values computed from the two methods is comparable to the values of F_x. Therefore, while we can use Sarazin and Roddier's approximations at lower heights, they do not hold good at larger heights. Even though Fried's intergal is more computationally intensive, we have opted for that in our calculations.

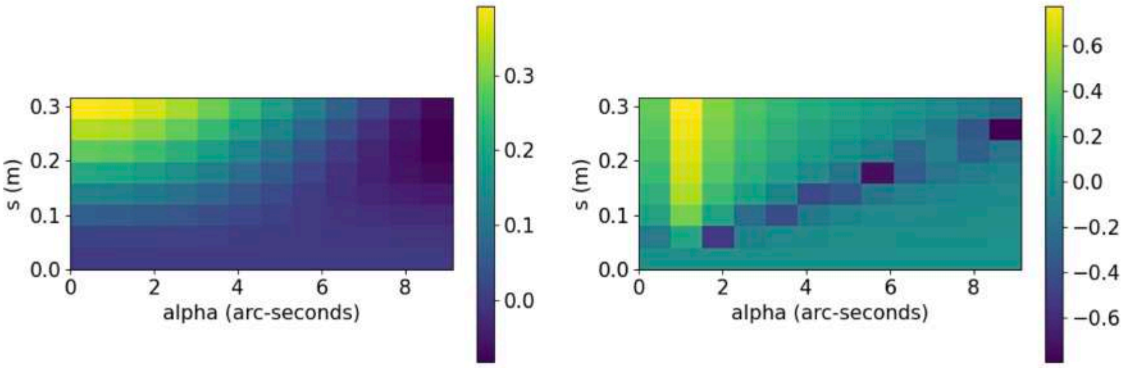

Figure B.3: Same as Figure B.2 but at 6 km height.

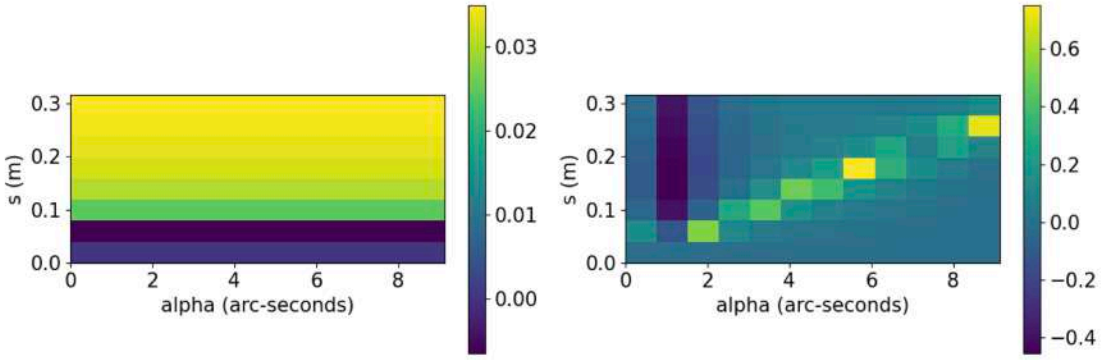

Figure B.4: Difference map of F_x obtained with Fried's equation and Sarazin's equation at 0 km height (left) and at 6 km height (right).

Appendix C

Temperature structure function measured using balloon-measurements

The temperature structure function ($D_T(r)$) is a measure of the difference in temperature fluctuations between two points that are spatially separated. It is important as it is a direct measure of the atmospheric properties at our site. It is given by (F. Roddier, 1981):

$$D_T(r) = \langle |T_1(x) - T_2(x+r)|^2 \rangle, \tag{C.1}$$

where x is the spatial co-ordinate, T_1 and T_2 are the fluctuations in temperatures at two points separated by a distance r. From our experiment, we can estimate $D_T(r)$ as the ensemble average of the modulus squared of the difference in temperature fluctuations between two sensors. Ideally, we need to measure the temperature of both the sensors at the same time and then estimate the difference. However, since we opted for a simpler setup with a single ADC, the data is recorded by each sensor sequentially. This means that there is a finite time delay between the temperature recorded from each sensor. The minimum difference is 10 ms and the maximum is 70 ms. We believe that the fluctuations in the temperatures within this time interval are minimal/negligible.

The $D_T(r)$ estimated using the data taken on 17th afternoon (when the weather conditions were very good) are shown in Figures C.1 and C.2. At each height, the $D_T(r)$ was estimated for the different baseline separations. The values of the height at which the curves were estimated are shown as legends that are inset within the respective plots. If a particular baseline separation had redundant combinations of sensors, the values from them were averaged. We were unable to observe any clear trend in the $D_T(r)$ curves with height. We do notice a sudden peak in value when the separation between the sensors is 40 cm in almost all the curves. The cause for this is not known at this point.

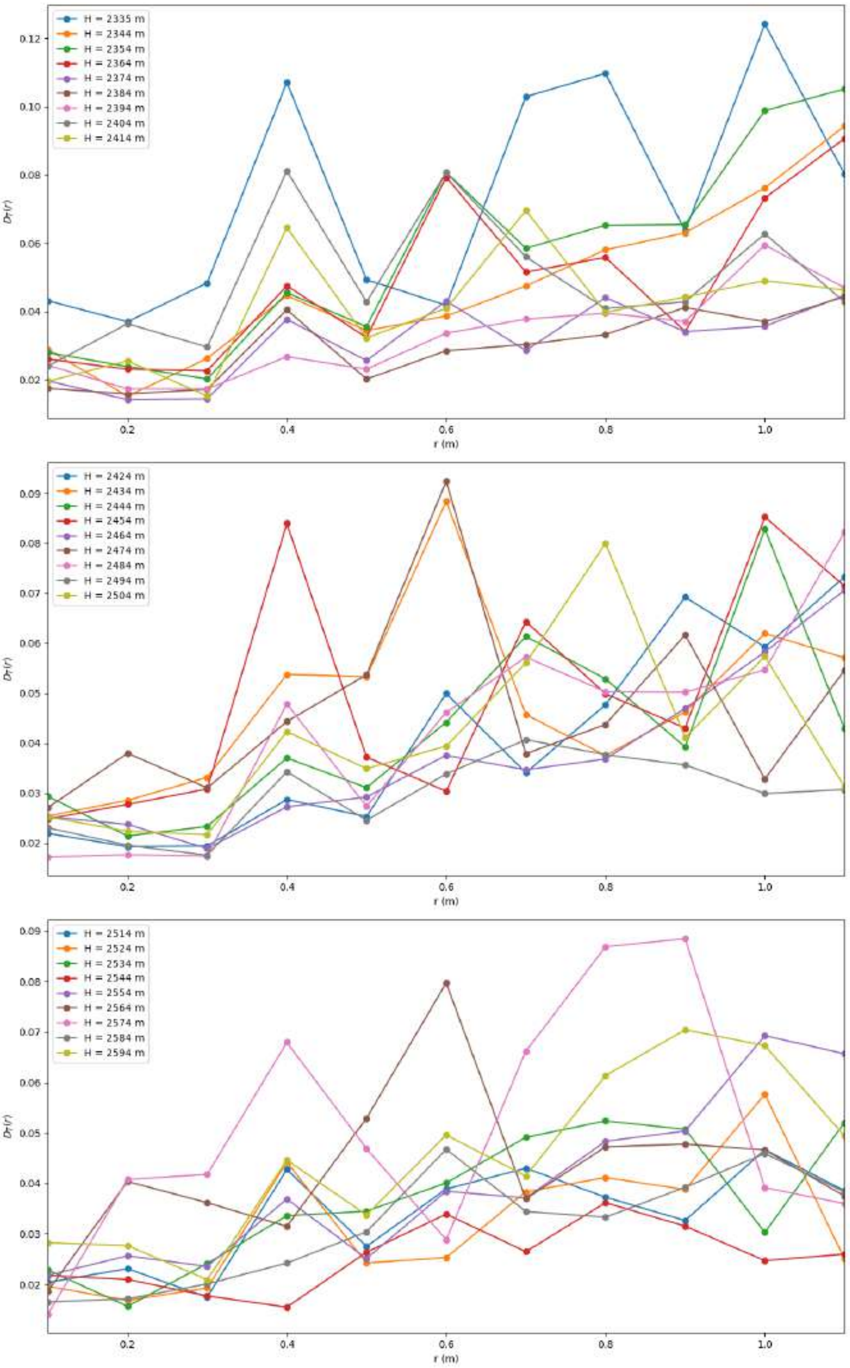

Figure C.1: The temperature structure function ($D_T(r)$) as a function of separation between sensors at different heights.

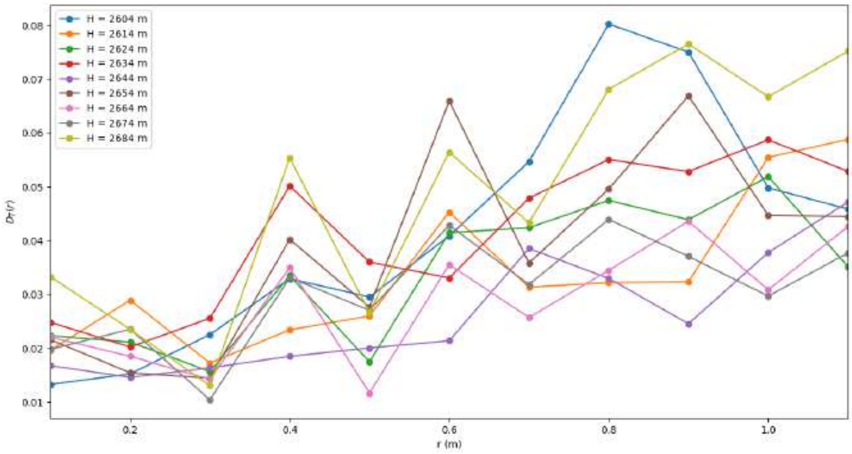

Figure C.2: The temperature structure function ($D_T(r)$) as a function of separation between sensors at different heights.

Furthermore, we have assumed a Kolmogorov type of turbulence when estimating the value of $C_T^2(r)$ (Equation 2.3). Therefore, we assumed that the structure function is proportional to the separation (r) raised to 2/3. To verify this, we fitted $D_T(r) = kr^{\mathrm{pwr}}$ and found the actual power term from the data. The results are shown in Figure C.3. The three curves are from the three data sets. The mean and standard deviations of the fitted “pwr” values are inset within the plots. We see that only for data set 3, the fitted power values match the expected 2/3 within error bars. Further experimentation is needed to properly understand the deviation from Kolmogorov theory.

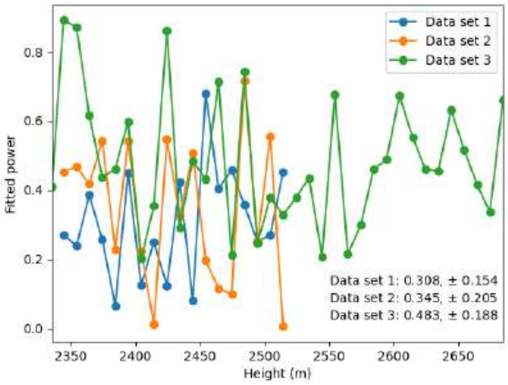

Figure C.3: A curve was fit for $D_T(r) = kr^{\mathrm{pwr}}$, where k is the constant of proportionality and ‘pwr’ represents the power of the separation. The fitted values of ‘pwr’ for the three data sets are shown as a function of the height at which the $D_T(r)$ was estimated.

Appendix D

Fitting the modified Hufnagel model to balloon-measurements

As described in Section 2.6.1, we initially fitted the results from the balloon-measurements to the full turbulence model as described by Equations 1.6 and 1.7. The results are shown and discussed in this appendix. The results from the data sets 1, 2, and 3 are shown in Tables D.1, D.2 and D.3, respectively.

Table D.1: Results from balloon-measurements for data set 1. The measured data was fitted to the modified Hufnagel model (Equations 1.6 and 1.7). The results of the fit for different combinations of wind velocity ratios and boundary scale height (first and second columns, respectively) are shown below. The fitted values of A and A_B are shown in the third and fourth columns, respectively. The r_0 (at 500 nm) estimated from the modified Hufnagel model fit at the same sampling as measurements and at finer sampling are given in the last two columns. r_0 estimated using measured profile from data set 1 was 38.79 cm (at 500 nm).

$\frac{V_w}{V_w}$	h_0 **(m)**	A	A_B	r_0 **(cm) - from fit 10 m sampling**	r_0 **(cm) - from fit 20 cm sampling**
0.3	100	1.56e+03	6.33e-15	44.51	4.28
3	100	1.55e+03	6.55e-15	44.51	4.28
0.3	180	1.43e+03	8.99e-15	44.45	4.27
3	180	1.41e+03	9.17e-15	44.46	4.27

Similar to the fits done in Section 2.6.1, different values of wind velocity ratios $\left(\frac{V_w}{V_w}\right)$ and boundary layer heights (h_0) were assumed. The assumed values of $\frac{V_w}{V_w}$ and h_0 are the first two columns of all three tables. A and A_B are the parameters of the fit and are the third and fourth columns, respectively, of each table. We can see that the fitted values of A and A_B do not change significantly with a change in the assumed velocity ratio and boundary height values. We first estimated the r_0 as the integral of the fitted C_N^2 profile at the same sampling at which measurements were done. This is shown in the fifth column of each table. The r_0 estimated as the integral of the actual estimated C_N^2 profile are given in the captions of table.

Finally, we estimated the r_0 value by interpolating the fitted model with a 20 cm sampling of the C_N^2 profile. The results are shown in the 6th column of each table. The r_0 estimates are consistent with the values estimated from a previous study (Rengaswamy, 2016). Also, by comparing the last column of Table 2.4 with the last column of Table D.1, there is less than 0.5 cm difference in the r_0 values calculated from the two fits. This shows that the contribution from the daytime component (Equation 1.7) is more significant than the Hufnagel model (Equation 1.6) at these heights. The trend is consistent across all three data sets. This can be observed by comparing Table 2.5 with Table D.2 or Table 2.6 with Table D.3.

Table D.2: Results from balloon-measurements for data set 2. The column headers are the same as Table D.1. r_0 estimated using measured profile from data set 2 was 38.21 cm (at 500 nm).

$\frac{V_w}{\overline{V_w}}$	h_0 **(m)**	A	A_B	r_0 **(cm) - from fit 10 m sampling**	r_0 **(cm) - from fit 20 cm sampling**
0.3	100	1.65e+03	3.47e-16	46.88	4.49
3	100	1.64e+03	5.56e-16	46.89	4.49
0.3	180	1.63e+03	9.25e-16	46.85	4.49
3	180	1.61e+03	1.20e-15	46.86	4.49

Table D.3: Results from balloon-measurements for data set 3. The column headers are the same as Table D.1. r_0 estimated using measured profile from data set 3 was 28.49 cm (at 500 nm).

$\frac{V_w}{\overline{V_w}}$	h_0 **(m)**	A	A_B	r_0 **(cm) - from fit 10 m sampling**	r_0 **(cm) - from fit 20 cm sampling**
0.3	100	1.70e+03	6.09e-15	28.91	2.77
3	100	1.69e+03	6.43e-15	28.91	2.78
0.3	180	1.65e+03	5.95e-15	28.91	2.77
3	180	1.63e+03	6.35e-15	28.91	2.77

Appendix E

Constraining the analytical form of $C_N^2(h)$ profile

The values of r_0 measured in section 3.3 can be used to generate phase screens described by the Kolmogorov theory of atmospheric turbulence. The phase screens can then be decomposed into Zernike polynomials and the coefficients of different polynomials can be determined. By correlating the coefficients of a particular polynomial from two different phase screens, the relation between the wavefronts passing through different regions of the atmosphere can be estimated.

If ϕ_1 and ϕ_2 are two phase screens, their Zernike decomposition is

$$\phi_1 = \sum_i a_{i1} Z_i \text{ and } \phi 2 = \sum_i a_{i2} Z_i\,, \tag{E.1}$$

where a_{i1} and a_{i2} are the i^{th} coefficients of the first and second phase screens, respectively and Z_i is the i^{th} Zernike polynomial. The correlation of the coefficients is

$$C_{ii}^{12} = \frac{\langle a_{i1} a_{i2} \rangle}{\sqrt{\langle a_{i1} \rangle}\sqrt{\langle a_{i2} \rangle}}\,. \tag{E.2}$$

Chassat (1989) established analytical expressions for the angular correlation of Zernike polynomials assuming a model of the turbulence strength profile to determine the expressions for the correlation given by

$$C_{nn}(\alpha) = \left(\frac{D}{r_0}\right)^{5/3} \frac{\int_0^L dh C_N^2(h) \sigma_n(\frac{\alpha h}{R})}{\int_0^L dh C_N^2(h)}\,. \tag{E.3}$$

Refer to Chassat (1989) for the definition and derivation of $\sigma_n(\frac{\alpha h}{R})$.

Equations E.2 and E.3 both describe the correlation of the coefficients. The former is for each coefficient, and the latter is the average of all coefficients of given radial order. We can estimate the correlation values for each polynomial coefficient using Equation E.2 as detailed above (generating phase screens using the r_0 values from the extended PSM and decomposing them). Then, the correlation values of all the coefficients of a specific order can be averaged and compared to the theoretical estimate from Equation E.3. One of the terms of Equation E.3 is $C_N^2(h)$. We can assume a model profile, say Hufnagel model (Equation 1.6). The parameters of the Hufnagel model (A, A_B, wind velocity ratio, etc) can be varied such that the best fit between the measured correlation and theoretical correlation is obtained. This is a potential method to constrain the C_N^2 profile at a site analytically.

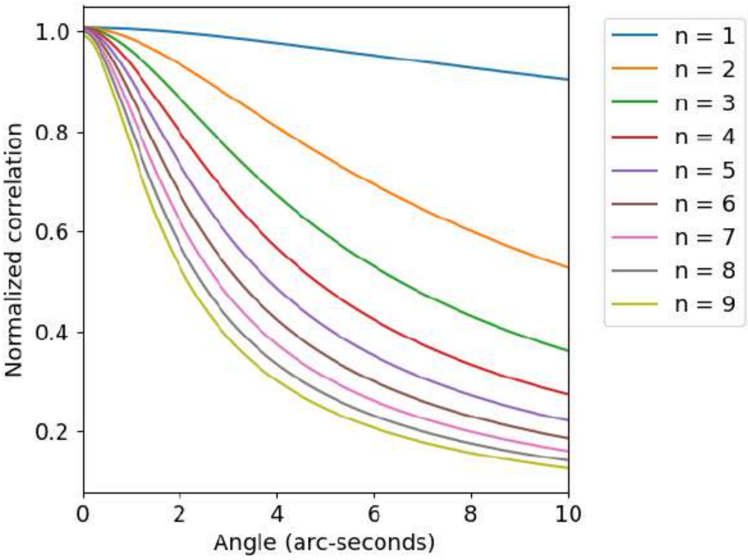

Figure E.1: Plot of normalised correlation coefficients of various Zernike polynomials as a function of angle (in arc-seconds). Each curve is for one radial order of polynomials as shown in the legend.

Figure E.1 shows the correlation curves as a function of angle (in arc-seconds) generated using Chassat's equations. A Hufnagel model has been assumed. The correlation values are normalized such that correlation at zero angle is unity. Each curve corresponds to a radial order of Zernike polynomials as shown in the legend. We can see that the lower order terms have better correlation even at larger angles. This implies that the lower order perturbations are likely to be better correlated even in wavefronts coming from larger angles away.

Appendix F

Alternate IQM: Median Filter Gradient Similarity

As stated in Section 5.1, there are some IQMs that do not need a reference image. One such metric is the Median Filter Gradient Similarity (MFGS) proposed by Deng et al. (2015) to identify the best frames in a series of frames for post-processing. In this method, the gradients of the instantaneous images whose quality is to be determined and that of their filtered versions are compared to determine the MFGS parameter. Once the images are generated using the simulations as described in section 5.2, the MFGS metric can be estimated using the following steps:

- Let the image whose quality is to be assessed be the raw image (R). It is passed through a median filter to obtain the processed image (P).
- The gradient operator is applied to the two images, R and P, to get the gradient of the images as G(R) and G(P), where G, the gradient operator, is defined as ([-1, 1]).
- The gradient values, G_R and G_P, are then found as the sum of the absolute values of the gradients of the raw and processed images, respectively.
- Then the MFGS value is estimated using the equation:

$$\text{MFGS} = \frac{2G_R G_P}{(G_R^2 + G_P^2)} \tag{F.1}$$

MFGS varies between zero and unity, and it was shown that a larger value corresponds to better-seeing conditions (Deng et al., 2015).

Figure F.2 shows the simulated long-exposure seeing-limited images under different seeing conditions. The r_0 (in cm) used for simulating each image, along with the measured rms granulation contrast and MFGS, are given to the left of each image. We can see that the rms granulation contrast values are increasing with r_0 as expected. But, the MFGS values are constant. This is because MFGS is primarily used as a metric to identify the best image from a series of short-exposure images (for example, Denker, Dineva, et al. (2018)). The selected image can then be post-processed using techniques like speckle masking to further improve the image quality. To further illustrate this point, we estimated both the metrics for four bursts (of 200 frames each) of short-exposure images taken at KTT. This is shown in Figure F.1. The four colors represent the four bursts of data. The values from instantaneous images are shown with circular markers and those from long-exposure images using crosses. Again, we see that the MFGS values for long-exposure images are constant.

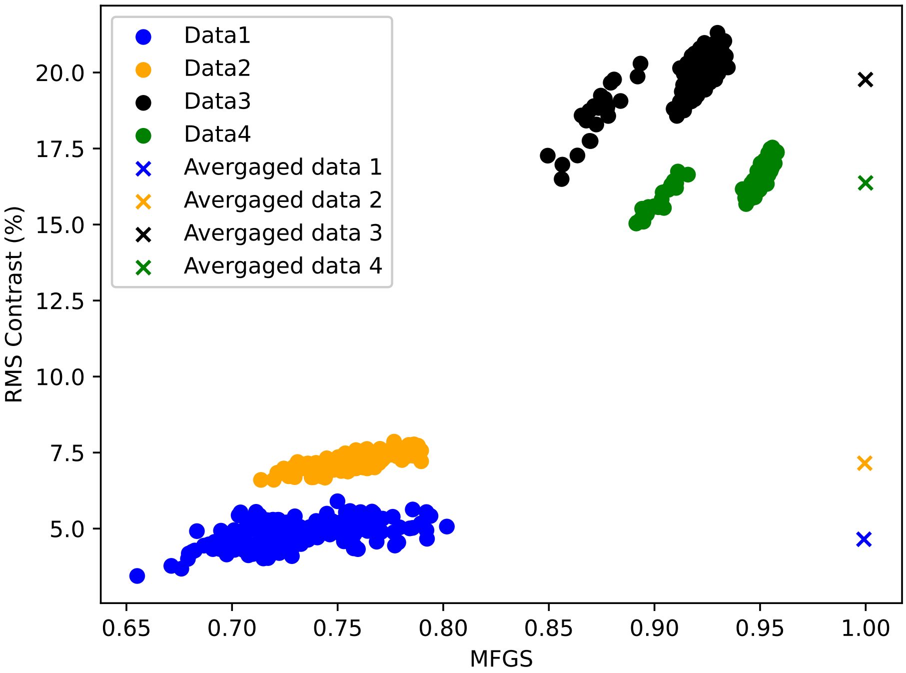

Figure F.1: RMS Contrast plotted against MFGS for 4 bursts of data obtained at the Kodaikanal Tunnel telescope. Averaged data is obtained by adding all the images in a given frame.

Therefore, while MFGS is useful for application on a series of short-exposure images and is also superior to rms granulation contrast due to its relative independence on the scene, it cannot be used for our application as we are determining the rms granulation contrast of solar images which have exposure times several times larger than the daytime atmospheric coherence time. The assumption we have made is that without AO, the exposure time is short enough not to be affected by telescope errors, and with AO, the errors will be corrected by the tip-tilt system. In other words, we wanted to arrive at a metric equivalent to that of the Strehl ratio, which is defined only for long-exposure images.

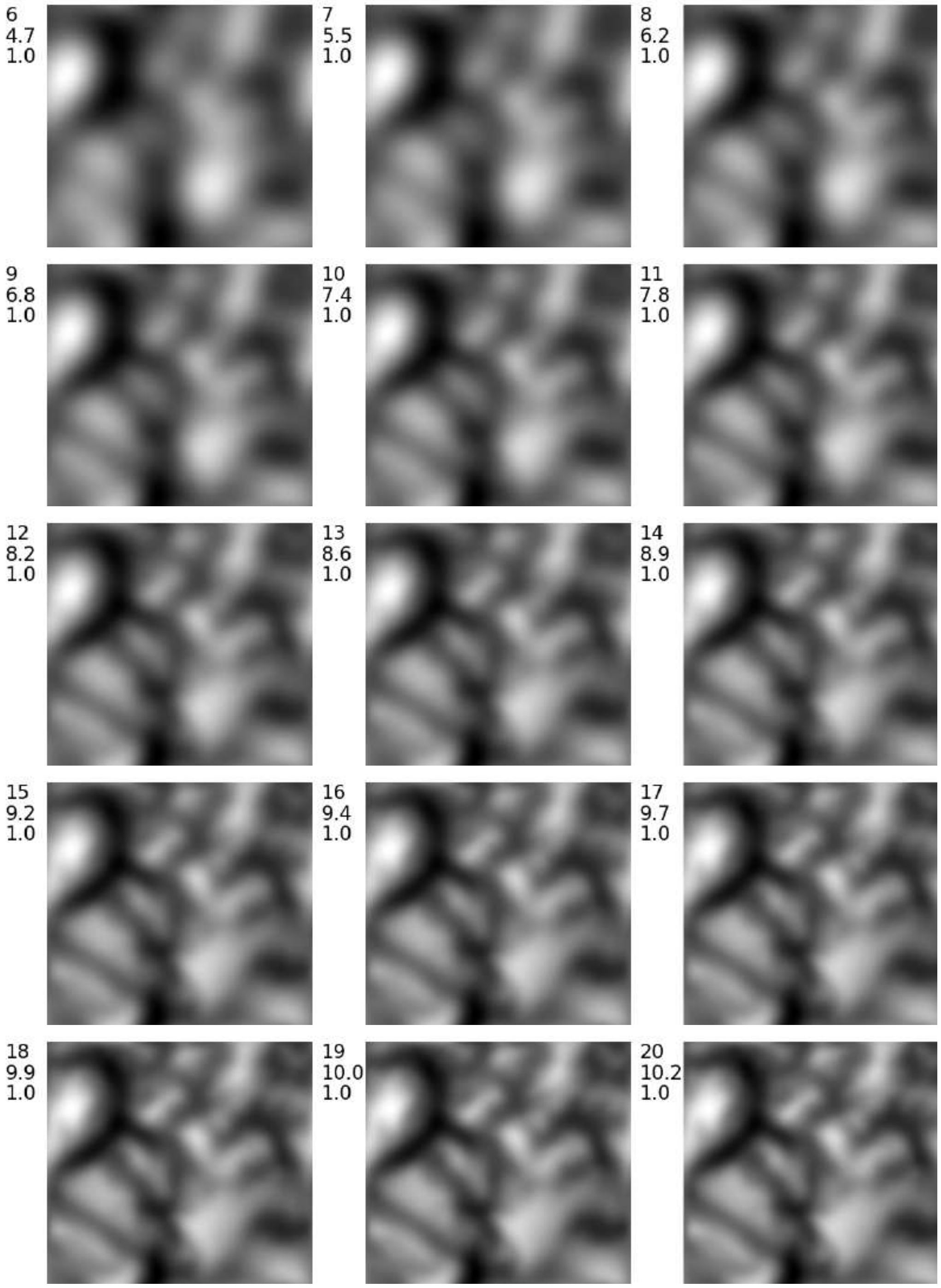

Figure F.2: Simulated long exposure seeing-limited images under different seeing conditions. To the left of each image, the r_0 (in cm), rms granulation contrast (%), and MFGS values for the image are given (in that order from top to bottom).

Bibliography

Abahamid, A. et al. (Mar. 2004). “Optical turbulence modeling in the boundary layer and free atmosphere using instrumented meteorological balloons”. In: *A&A* 416, pp. 1193–1200. DOI: `10.1051/0004-6361:20031390`.

Abdurrahman, F. N. et al. (Sept. 2018). “Improved Image Quality over 10′ Fields with the ´Imaka Ground-layer Adaptive Optics Experiment”. In: *The Astronomical Journal* 156.3, 100, p. 100. DOI: `10.3847/1538-3881/aad1f2`. arXiv: `1807.03885 [astro-ph.IM]`.

Acton, D. S. and R. B. Dunn (Aug. 1993). “Solar imaging at National Solar Observatory using a segmented adaptive optics system”. In: *Active and Adaptive Optical Components and Systems II*. Ed. by Mark A. Ealey. Vol. 1920. Society of Photo-Optical Instrumentation Engineers (SPIE) Conference Series, pp. 348–352. DOI: `10.1117/12.152680`.

Angel, J. R. P. et al. (Dec. 1994). “A Search for Planets of Nearby Stars by Direct Imaging from the Ground”. In: *American Astronomical Society Meeting Abstracts*. Vol. 185. American Astronomical Society Meeting Abstracts, 42.05, p. 42.05.

Aston, F. W. (1920). “LIX. The mass-spectra of chemical elements”. In: *The London, Edinburgh, and Dublin Philosophical Magazine and Journal of Science* 39.233, pp. 611–625. DOI: `10.1080/14786440508636074`. eprint: `https://doi.org/10.1080/14786440508636074`. URL: `https://doi.org/10.1080/14786440508636074`.

Azouit, M. and J. Vernin (May 2005). “Optical Turbulence Profiling with Balloons Relevant to Astronomy and Atmospheric Physics”. In: *PASP* 117.831, pp. 536–543. DOI: `10.1086/429785`.

Babcock, H. W. (Oct. 1953). “The Possibility of Compensating Astronomical Seeing”. In: *PASP* 65.386, p. 229. DOI: `10.1086/126606`.

Bappu, M. K. V. (Jan. 1967). “Solar Physics at Kodaikanal”. In: *Solar Physics* 1.1, pp. 151–156. DOI: `10.1007/BF00150312`.

Baranec, C., M. Lloyd-Hart, N. M. Milton, T. Stalcup, M. Snyder, and R. Angel (June 2006). “Tomographic reconstruction of stellar wavefronts from multiple laser guide stars”. In: *Advances in Adaptive Optics II*. Ed. by Brent L. Ellerbroek and Domenico Bonaccini Calia. Vol. 6272. Society of Photo-Optical Instrumentation Engineers (SPIE) Conference Series, 627203, p. 627203. DOI: `10.1117/12.672529`.

Baranec, C., M. Lloyd-Hart, N. M. Milton, T. Stalcup, M. Snyder, V. Vaitheeswaran, et al. (Sept. 2007). “Astronomical imaging using ground-layer adaptive optics”. In: *Astronomical Adaptive Optics Systems and Applications III*. Ed. by R. K. Tyson and M. Lloyd-Hart. Vol. 6691. Society of Photo-Optical Instrumentation Engineers (SPIE) Conference Series, 66910N, 66910N. DOI: `10.1117/12.732609`.

Barletti, R. et al. (Dec. 1976). “Mean vertical profile of atmospheric turbulence relevant for astronomical seeing”. In: *Journal of the Optical Society of America (1917-1983)* 66.12, p. 1380.

Bayanna, A. R., B. Kumar, et al. (June 2008). “Development of a low-order Adaptive Optics system at Udaipur Solar Observatory”. In: *Journal of Astrophysics and Astronomy* 29.1-2, pp. 353–357. DOI: `10.1007/s12036-008-0046-6`.

Bayanna, A. R., R. E. Louis, et al. (Mar. 2015). “Membrane-based deformable mirror: intrinsic aberrations and alignment issues”. In: *Applied Optics* 54.7, p. 1727. DOI: `10.1364/AO.54.001727`. arXiv: `1502.04424 [physics.optics]`.

Beckers, J. M. (Oct. 1988). “Increasing the Size of the Isoplanatic Patch with Multiconjugate Adaptive Optics”. In: *Very Large Telescopes and their Instrumentation, Vol. 2*. Ed. by M. -H. Ulrich. Vol. 30. European Southern Observatory Conference and Workshop Proceedings, p. 693.

— (Jan. 1993a). “Adaptive Optics for Astronomy: Principles, Performance, and Applications”. In: *Annual reviews in astronomy and astrophysics* 31, pp. 13–62. DOI: `10.1146/annurev.aa.31.090193.000305`.

— (June 1993b). “On the Relation Between Scintillation and Seeing Observations of Extended Objects”. In: *Solar Phys.* 145.2, pp. 399–402. DOI: `10.1007/BF00690665`.

— (Sept. 1999). “The Determination of Seeing, Isoplanatic Patch Size and Coherence Time by Solar Shadow Band Ranging”. In: *Third Advances in Solar Physics Euroconference: Magnetic Fields and Oscillations*. Ed. by B. Schmieder, A. Hofmann, and J. Staude. Vol. 184. Astronomical Society of the Pacific Conference Series, pp. 309–313.

— (Jan. 2001). “A Seeing Monitor for Solar and Other Extended Object Observations”. In: *Experimental Astronomy* 12.1, pp. 1–20.

Berger, T. E. et al. (Oct. 2007). “What are 'Faculae'?” In: *New Solar Physics with Solar-B Mission*. Ed. by K. Shibata, S. Nagata, and T. Sakurai. Vol. 369. Astronomical Society of the Pacific Conference Series, p. 103.

Berkefeld, T. and D. Soltau (June 2010). “EST Adaptive optics performance estimations”. In: *Astronomische Nachrichten* 331.6, p. 640. DOI: `10.1002/asna.201011391`.

Berkefeld, T., D. Soltau, D. Schmidt, et al. (Sept. 2010). “Adaptive optics development at the German solar telescopes”. In: *Applied Optics* 49.31, G155. DOI: 10.1364/AO.49.00G155.

Berkefeld, T., D. Soltau, and O. von der Lühe (Feb. 2002). “Multiconjugate adaptive optics at the Vacuum Tower Telescope, Tenerife”. In: *Optics in Atmospheric Propagation and Adaptive Systems IV*. Ed. by Anton Kohnle, John D. Gonglewski, and Thomas J. Schmugge. Vol. 4538. Society of Photo-Optical Instrumentation Engineers (SPIE) Conference Series, pp. 119–127. DOI: 10.1117/12.454398.

— (Feb. 2003). “Multi-conjugate Adaptive Optics at the Vacuum Tower Telescope, Tenerife”. In: *Adaptive Optical System Technologies II*. Ed. by Peter L. Wizinowich and Domenico Bonaccini. Vol. 4839. Society of Photo-Optical Instrumentation Engineers (SPIE) Conference Series, pp. 544–553. DOI: 10.1117/12.459799.

— (Aug. 2005). “Results of the multi-conjugate adaptive optics system at the German solar telescope, Tenerife”. In: *Astronomical Adaptive Optics Systems and Applications II*. Ed. by Robert K. Tyson and Michael Lloyd-Hart. Vol. 5903. Society of Photo-Optical Instrumentation Engineers (SPIE) Conference Series, pp. 219–226. DOI: 10.1117/12.619132.

— (June 2006). “Multi-conjugate solar adaptive optics with the VTT and GREGOR”. In: *Advances in Adaptive Optics II*. Ed. by Brent L. Ellerbroek and Domenico Bonaccini Calia. Vol. 6272. Society of Photo-Optical Instrumentation Engineers (SPIE) Conference Series, 627205, p. 627205. DOI: 10.1117/12.671718.

Berkefeld, Th. et al. (Nov. 2012). “The GREGOR adaptive optics system”. In: *Astronomische Nachrichten* 333.9, p. 863. DOI: 10.1002/asna.201211739.

Bertram, T. et al. (June 2023). “METIS SCAO – implementing AO for ELT”. In: *Adaptive Optics for Extremely Large Telescopes (AO4ELT7)*, 23, p. 23. DOI: 10.13009/AO4ELT7-2023-024.

Bethe, H. A. and C. L. Critchfield (Aug. 1938). “The Formation of Deuterons by Proton Combination”. In: *Physical Review* 54 (4), pp. 248–254. DOI: 10.1103/PhysRev.54.248. URL: https://link.aps.org/doi/10.1103/PhysRev.54.248.

Beuzit, J. -L. et al. (Sept. 2006). “SPHERE: A ’Planet Finder’ Instrument for the VLT”. In: *The Messenger* 125, p. 29.

Boccas, M. et al. (June 2006). “Laser guide star upgrade of Altair at Gemini North”. In: *Advances in Adaptive Optics II*. Ed. by Brent L. Ellerbroek and Domenico Bonaccini Calia. Vol. 6272. Society of Photo-Optical Instrumentation Engineers (SPIE) Conference Series, 62723L, p. 62723L. DOI: 10.1117/12.670842.

Bonaccini, D. et al. (Dec. 1999). “Laser Guide Star Facility for the ESO VLT.” In: *The Messenger* 98, pp. 8–14.

Bonaccini Calia, D. et al. (June 2006). “First light of the ESO Laser Guide Star Facility”. In: *Advances in Adaptive Optics II*. Ed. by Brent L. Ellerbroek and Domenico Bonaccini Calia. Vol. 6272. Society of Photo-Optical Instrumentation Engineers (SPIE) Conference Series, 627207, p. 627207. DOI: `10.1117/12.674484`.

Bouchez, A. et al. (June 2023). “Giant Magellan Telescope Adaptive Optics Overview”. In: *Adaptive Optics for Extremely Large Telescopes (AO4ELT7)*, 115, p. 115. DOI: `10.13009/AO4ELT7-2023-117`.

Boyer, C., B. Ellerbroek, et al. (Jan. 2010). “The TMT Laser Guide Star Facility”. In: *Adaptative Optics for Extremely Large Telescopes*, 04004, p. 04004. DOI: `10.1051/ao4elt/201004004`.

Boyer, C., L. Wang, et al. (June 2023). “TMT AO Facility Status Report”. In: *Adaptive Optics for Extremely Large Telescopes (AO4ELT7)*, 120, p. 120. DOI: `10.13009/AO4ELT7-2023-122`.

Brandt, P. N. (May 1969). “Frequency Spectra of Solar Image Motion”. In: *Solar Physics* 7.2, pp. 187–203. DOI: `10.1007/BF00224897`.

— (July 1970). “Measurement of Solar Image Motion and Blurring”. In: *Solar Physics* 13.1, pp. 243–246. DOI: `10.1007/BF00963959`.

Bufton, J. L. et al. (Sept. 1972). “Measurements of Turbulence Profiles in the Troposphere”. In: *Journal of the Optical Society of America (1917-1983)* 62.9, p. 1068.

Busoni, L. et al. (June 2023). “MORFEO enters final design phase”. In: *Adaptive Optics for Extremely Large Telescopes (AO4ELT7)*, 129, p. 129. DOI: `10.13009/AO4ELT7-2023-046`. arXiv: `2310.09005 [astro-ph.IM]`.

Calvo, F., O. Steiner, and B. Freytag (Nov. 2016). “Non-magnetic photospheric bright points in 3D simulations of the solar atmosphere”. In: *Astronomy and Astrophysics* 596, A43, A43. DOI: `10.1051/0004-6361/201628649`. arXiv: `1612.04278 [astro-ph.SR]`.

Cao, W. et al. (June 2010). “Scientific instrumentation for the 1.6 m New Solar Telescope in Big Bear”. In: *Astronomische Nachrichten* 331.6, p. 636. DOI: `10.1002/asna.201011390`.

Chassat, F. (Feb. 1989). “Calcul du domaine d’isoplanétisme d’un système d’optique adaptative fonctionnant à travers la turbulence atmosphérique.” In: *Journal of Optics* 20.1, pp. 13–23. DOI: `10.1088/0150-536X/20/1/002`.

Clerke, A. M. (1893). *A Popular History of Astronomy During the Nineteenth Century (3rd Edition)*. A & C Black.

Conan, R. et al. (Dec. 2013). “The Giant Magellan Telescope Laser Tomography Adaptive Optics System”. In: *Proceedings of the Third AO4ELT Conference*. Ed. by Simone Esposito and Luca Fini, 4, p. 4. DOI: `10.12839/AO4ELT3.12521`.

Costille, A. et al. (Jan. 2010). “Experimental results of tomographic reconstruction on ONERA laboratory MCAO bench”. In: *Adaptative Optics for Extremely Large Telescopes*, 08004, p. 08004. DOI: `10.1051/ao4elt/201008004`.

Crane, J. et al. (July 2018). “NFIRAOS adaptive optics for the Thirty Meter Telescope”. In: *Adaptive Optics Systems VI*. Ed. by Laird M. Close, Laura Schreiber, and Dirk Schmidt. Vol. 10703. Society of Photo-Optical Instrumentation Engineers (SPIE) Conference Series, 107033V, p. 107033V. DOI: `10.1117/12.2314341`.

D’Orgeville, C., A. Bouchez, et al. (Dec. 2013). “GMT Laser Guide Star Facility”. In: *Proceedings of the Third AO4ELT Conference*. Ed. by Simone Esposito and Luca Fini, 14, p. 14. DOI: `10.12839/AO4ELT3.13119`.

D’Orgeville, C. and G. J. Fetzer (July 2016). “Four generations of sodium guide star lasers for adaptive optics in astronomy and space situational awareness”. In: *Adaptive Optics Systems V*. Ed. by Enrico Marchetti, Laird M. Close, and Jean-Pierre Véran. Vol. 9909. Society of Photo-Optical Instrumentation Engineers (SPIE) Conference Series, 99090R, 99090R. DOI: `10.1117/12.2234298`.

Davies, R. and M. Kasper (Sept. 2012). “Adaptive Optics for Astronomy”. In: *Annu. Rev. in Astron. & Astrophys.* 50, pp. 305–351. DOI: `10.1146/annurev-astro-081811-125447`. arXiv: `1201.5741 [astro-ph.IM]`.

de Jong, T. and W. H. van Soldt (Mar. 1989). “The earliest known solar eclipse record redated”. In: *Nature* 338.6212, pp. 238–240. DOI: `10.1038/338238a0`.

Deng, H. et al. (May 2015). “Objective Image-Quality Assessment for High-Resolution Photospheric Images by Median Filter-Gradient Similarity”. In: *Solar Physics* 290.5, pp. 1479–1489. DOI: `10.1007/s11207-015-0676-1`.

Denker, C., E. Dineva, et al. (Mar. 2018). “Image Quality in High-resolution and High-cadence Solar Imaging”. In: *Solar Physics* 293.3, 44, p. 44. DOI: `10.1007/s11207-018-1261-1`. arXiv: `1802.00760 [astro-ph.SR]`.

Denker, C., S. Restaino, and R. Radick (Dec. 1993). “A Comparison of Two Wavefront Sensors”. In: *Real Time and Post Facto Solar Image Correction*. Ed. by Richard R. Radick, p. 86.

Dicke, R. H. (June 1975). “Phase-contrast detection of telescope seeing errors and their correction.” In: *Astrophysical Journal* 198, pp. 605–615. DOI: `10.1086/153639`.

Didkovsky, L. V., C. Denker, et al. (Jan. 2003). “High-order adaptive optical system for Big Bear Solar Observatory”. In: *Astronomische Nachrichten* 324.4, pp. 297–298. DOI: `10.1002/asna.200310099`.

Didkovsky, L. V., A. Dolgushyn, et al. (Feb. 2003). “High-order adaptive optical system for Big Bear Solar Observatory”. In: *Innovative Telescopes and Instrumentation for Solar Astrophysics*. Ed. by Stephen L. Keil and Sergey V. Avakyan. Vol. 4853. Society of Photo-Optical Instrumentation Engineers (SPIE) Conference Series, pp. 630–639. DOI: 10.1117/12.471341.

Diolaiti, E. (Dec. 2013). “Overview of the E-ELT MCAO module project”. In: *Proceedings of the Third AO4ELT Conference*. Ed. by Simone Esposito and Luca Fini, 88, p. 88. DOI: 10.12839/AO4ELT3.13380.

Dunn, R. B. (Aug. 1990). “NSO/SP adaptive optics program.” In: *Adaptive optics and optical structures*. Ed. by Joachim J. Schulte-In-den-Baeumen and Robert K. Tyson. Vol. 1271. Society of Photo-Optical Instrumentation Engineers (SPIE) Conference Series, pp. 216–231. DOI: 10.1117/12.20409.

Dunn, R. B., G. Streander, and O. V. D. Lühe (Aug. 1989). “Adaptive optical system at Sac Peak: a progress update”. In: *High spatial resolution solar observations*. Ed. by Oskar von der Lühe, p. 53.

Eddington, A. S. (1920). “The Internal Constitution of the Stars”. In: *The Scientific Monthly* 11.4, pp. 297–303. ISSN: 00963771. URL: http://www.jstor.org/stable/6491 (visited on 08/27/2024).

Ellerbroek, B. L. (Feb. 1994). “First-order performance evaluation of adaptive-optics systems for atmospheric-turbulence compensation in extended-field-of-view astronomical telescopes.” In: *Journal of the Optical Society of America A* 11.2, pp. 783–805. DOI: 10.1364/JOSAA.11.000783.

Ellerbroek, B. L. and D. W. Tyler (Feb. 1998). “Adaptive Optics Sky Coverage Calculations for the Gemini-North Telescope”. In: *Publications of the Astronomical Society of the Pacific* 110.744, pp. 165–185. DOI: 10.1086/316120.

Esposito, S. (Sept. 1998). “Techniques to solve the tilt indetermination problem: methods, limitations, and errors”. In: *Adaptive Optical System Technologies*. Ed. by Domenico Bonaccini and Robert K. Tyson. Vol. 3353. Society of Photo-Optical Instrumentation Engineers (SPIE) Conference Series, pp. 468–476. DOI: 10.1117/12.321682.

Farley, O. et al. (2017). “Deformable mirror configuration in MCAO: is propagation a fundamental limit on visible wavelength correction?” In: *AO4ELT5 Proceedings*. URL: http://research.iac.es/congreso/AO4ELT5//media/proceedings/proceeding-091.pdf.

Femenía-Castella, B. et al. (Aug. 2022). “Adaptive Optics at the European Solar Telescope: status and future developments”. In: *Adaptive Optics Systems VIII*. Ed. by Laura Schreiber, Dirk Schmidt, and Elise Vernet. Vol. 12185. Society of Photo-Optical Instrumentation Engineers (SPIE) Conference Series, 121851Z, 121851Z. DOI: 10.1117/12.2629516.

Flicker, R. C. (Nov. 2001). “Sequence of phase correction in multiconjugate adaptive optics”. In: *Optics Letters* 26.22, pp. 1743–1745. DOI: 10.1364/OL.26.001743. URL: https://opg.optica.org/ol/abstract.cfm?URI=ol-26-22-1743.

Foy, R. and A. Labeyrie (Nov. 1985). “Feasibility of adaptive telescope with laser probe”. In: *Astronomy and Astrophysics* 152.2, pp. L29–L31.

Fraunhofer, J. (1817). “Brechungs-und Farbenzerstreuungs-Vermögens verschiedener Glasarten”. In: *Denkschriften der Königlichen Akademie der Wissenschaften zu München für 1814 und 1815* 5.

Freytag, B. et al. (Feb. 2012). “Simulations of stellar convection with CO5BOLD”. In: *Journal of Computational Physics* 231.3, pp. 919–959. DOI: `10.1016/j.jcp.2011.09.026`. arXiv: `1110.6844 [astro-ph.SR]`.

Fried, D. L. (Nov. 1965). “Statistics of a Geometric Representation of Wavefront Distortion”. In: *Journal of the Optical Society of America (1917-1983)* 55.11, pp. 1427–1431. DOI: `10.1364/JOSA.55.001427`.

— (Oct. 1966). “Optical Resolution Through a Randomly Inhomogeneous Medium for Very Long and Very Short Exposures”. In: *Journal of the Optical Society of America (1917-1983)* 56.10, p. 1372.

— (Jan. 1975). “Differential angle of arrival - Theory, evaluation, and measurement feasibility”. In: *Radio Science* 10, pp. 71–76. DOI: `10.1029/RS010i001p00071`.

Fröhlich, C. (Jan. 2002). “Total solar irradiance variations since 1978”. In: *Advances in Space Research* 29.10, pp. 1409–1416. DOI: `10.1016/S0273-1177(02)00203-X`.

Fusco, T. et al. (July 2010). “Adaptive optics systems for HARMONI: a visible and near-infrared integral field spectrograph for the E-ELT”. In: *Adaptive Optics Systems II*. Ed. by Brent L. Ellerbroek et al. Vol. 7736. Society of Photo-Optical Instrumentation Engineers (SPIE) Conference Series, 773633, p. 773633. DOI: `10.1117/12.857507`.

Galicher, R. and J. Mazoyer (Jan. 2024). “Imaging exoplanets with coronagraphic instruments”. In: *Comptes Rendus Physique* 24.S2, 133, p. 133. DOI: `10.5802/crphys.133`. arXiv: `2302.10833 [astro-ph.EP]`.

Gaug, M. and M. Doro (Nov. 2018). “Impact of Laser Guide Star facilities on neighbouring telescopes: the case of GTC, TMT, VLT, and ELT lasers and the Cherenkov Telescope Array”. In: *Monthly Notices of the Royal Astronomical Society* 481.1, pp. 727–748. DOI: `10.1093/mnras/sty2188`. arXiv: `1808.03820 [astro-ph.IM]`.

Gelly, B. et al. (July 2016). “New life for the THEMIS solar telescope”. In: *Ground-based and Airborne Telescopes VI*. Ed. by Helen J. Hall, Roberto Gilmozzi, and Heather K. Marshall. Vol. 9906. Society of Photo-Optical Instrumentation Engineers (SPIE) Conference Series, 99065A, 99065A. DOI: `10.1117/12.2232455`.

Guyon, O. (Sept. 2018). “Extreme Adaptive Optics”. In: *Annual reviews in astronomy and astrophysics* 56, pp. 315–355. DOI: `10.1146/annurev-astro-081817-052000`.

Hale, G. E. (Nov. 1908). “On the Probable Existence of a Magnetic Field in Sun-Spots”. In: *Astrophyisical Journal* 28, p. 315. DOI: `10.1086/141602`.

Hardy, J. W. (Sept. 1980). *Solar imaging experiment*. Final Report, Feb. 1979 - Jun. 1980 Itek Corp., Lexington, MA. Optical Systems Div.

Hart, M. et al. (Jan. 2008). "Ground-Layer Adaptive Optics with Multiple Laser Guide Stars". In: *Advanced Maui Optical and Space Surveillance Technologies Conference*. Ed. by C. Paxson et al., E17, E17.

Heath, T. (1913). *Aristarchus of Samos, the ancient Copernicus*. Oxford, Clarendon Press.

Herbst, T. M. et al. (July 2018). "Commissioning multi-conjugate adaptive optics with LINC-NIRVANA on LBT". In: *Adaptive Optics Systems VI*. Ed. by Laird M. Close, Laura Schreiber, and Dirk Schmidt. Vol. 10703. Society of Photo-Optical Instrumentation Engineers (SPIE) Conference Series, 107030B, 107030B. DOI: 10.1117/12.2313421.

Herschel, W. (Jan. 1800). "Investigation of the Powers of the Prismatic Colours to Heat and Illuminate Objects; With Remarks, That Prove the Different Refrangibility of Radiant Heat. To Which is Added, an Inquiry into the Method of Viewing the Sun Advantageously, with Telescopes of Large Apertures and High Magnifying Powers. By William Herschel, LL. D. F. R. S." In: *Philosophical Transactions of the Royal Society of London Series I* 90, pp. 255–283.

Hickson, P. and K. Lanzetta (Dec. 2004). "Measuring Atmospheric Turbulence with a Lunar Scintillometer Array". In: *PASP* 116.826, pp. 1143–1152. DOI: 10.1086/427046.

Hill, F., R. Radick, and M. Collados (Apr. 2004). "Deriving $C_N^2(h)$ from a Scintillometer Array". In: *Project Documentation* 0014 Revision A.

Hinz, P. et al. (Sept. 2012). "TIGER: a high contrast infrared imager for the Giant Magellan Telescope". In: *Ground-based and Airborne Instrumentation for Astronomy IV*. Ed. by Ian S. McLean, Suzanne K. Ramsay, and Hideki Takami. Vol. 8446. Society of Photo-Optical Instrumentation Engineers (SPIE) Conference Series, 84461P, 84461P. DOI: 10.1117/12.926751.

Hubin, N. et al. (Jan. 2006). "Adaptive optics for Extremely Large Telescopes". In: *The Scientific Requirements for Extremely Large Telescopes*. Ed. by P. Whitelock, M. Dennefeld, and B. Leibundgut. Vol. 232. IAU Symposium, pp. 60–85. DOI: 10.1017/S1743921306000287.

Hufnagel, R. E. (1974). *The Infrared Handbook*. Washington, D. C. Chap. 6.

Johansson, E. et al. (July 2018). "The DKIST low order wavefront sensor". In: *Adaptive Optics Systems VI*. Ed. by Laird M. Close, Laura Schreiber, and Dirk Schmidt. Vol. 10703. Society of Photo-Optical Instrumentation Engineers (SPIE) Conference Series, 107035P, 107035P. DOI: 10.1117/12.2313745.

Johnson, L. C., K. Cummings, et al. (July 2016). "Status of the DKIST system for solar adaptive optics". In: *Adaptive Optics Systems V*. Ed. by Enrico Marchetti, Laird M.

Close, and Jean-Pierre Véran. Vol. 9909. Society of Photo-Optical Instrumentation Engineers (SPIE) Conference Series, 99090Y, 99090Y. DOI: `10.1117/12.2233528`.

Johnson, L. C., E. Johansson, et al. (Dec. 2020). "First light with adaptive optics: the performance of the DKIST high-order adaptive optics". In: *Adaptive Optics Systems VII*. Ed. by Laura Schreiber, Dirk Schmidt, and Elise Vernet. Vol. 11448. Society of Photo-Optical Instrumentation Engineers (SPIE) Conference Series, 114480T, 114480T. DOI: `10.1117/12.2563427`.

Jovanovic, N. et al. (Sept. 2015). "The Subaru Coronagraphic Extreme Adaptive Optics System: Enabling High-Contrast Imaging on Solar-System Scales". In: *Publications of the astronomical society of Pacific* 127.955, p. 890. DOI: `10.1086/682989`. arXiv: `1507.00017 [astro-ph.IM]`.

Kasper, M., C. Verinaud, and D. Mawet (Dec. 2013). "Roadmap for PCS, the Planetary Camera and Spectrograph for the E-ELT". In: *Proceedings of the Third AO4ELT Conference*. Ed. by Simone Esposito and Luca Fini, 8, p. 8. DOI: `10.12839/AO4ELT3.12804`.

Kawate, T. et al. (Sept. 2011). "Seeing measurements using the solar limb - I. Comparison of evaluation methods for the Differential Image Motion Monitor". In: *MNRAS* 416.3, pp. 2154–2162. DOI: `10.1111/j.1365-2966.2011.19192.x`.

Keller, C. U., C. Plymate, and S. M. Ammons (Feb. 2003). "Low-cost solar adaptive optics in the infrared". In: *Innovative Telescopes and Instrumentation for Solar Astrophysics*. Ed. by Stephen L. Keil and Sergey V. Avakyan. Vol. 4853. Society of Photo-Optical Instrumentation Engineers (SPIE) Conference Series, pp. 351–359. DOI: `10.1117/12.460370`.

Kellerer, A. et al. (June 2012). "Profiles of the daytime atmospheric turbulence above Big Bear solar observatory". In: *A&A* 542, A2, A2. DOI: `10.1051/0004-6361/201218844`.

Kiepenheuer, K. O. (Jan. 1964). "Solar Site Testing". In: *Le choix des sites d'observatoires astronomiques (site testing)*. Ed. by Jean Rosch. Vol. 19, p. 193.

Kolmogorov, A. (Jan. 1941). "The Local Structure of Turbulence in Incompressible Viscous Fluid for Very Large Reynolds' Numbers". In: *Akademiia Nauk SSSR Doklady* 30, pp. 301–305.

Kragh, H. (Nov. 2016). "The source of solar energy, ca. 1840-1910: From meteoric hypothesis to radioactive speculations". In: *European Physical Journal H* 41.4. DOI: `10.1140/epjh/e2016-70045-7`. arXiv: `1609.02834 [physics.hist-ph]`.

Krüger, A. (1979). *Introduction to Solar Radio Astronomy and Radio Physics*. 1st ed. Vol. 16. Geophysics and Astrophysics Monographs 16. Springer Netherlands. DOI: `10.1007/978-94-009-9402-7`.

Kupke, R., F. J. Roddier, and D. Mickey (May 1994). “Curvature-based wavefront sensor for use on extended patterns”. In: *Adaptive Optics in Astronomy*. Ed. by Mark A. Ealey and Fritz Merkle. Vol. 2201. Society of Photo-Optical Instrumentation Engineers (SPIE) Conference Series, pp. 519–527. DOI: 10.1117/12.176087.

Lakshminarayanan, V. and A. Fleck (Apr. 2011). “Zernike polynomials: a guide”. In: *Journal of Modern Optics* 58.7, pp. 545–561. DOI: 10.1080/09500340.2011.554896.

Langlois, M. et al. (Oct. 2004). “Solar multiconjugate adaptive optics at the Dunn Solar Telescope: preliminary results”. In: *Advancements in Adaptive Optics*. Ed. by Domenico Bonaccini Calia, Brent L. Ellerbroek, and Roberto Ragazzoni. Vol. 5490. Society of Photo-Optical Instrumentation Engineers (SPIE) Conference Series, pp. 59–66. DOI: 10.1117/12.548929.

Le Mignant, D. et al. (June 2006). “LGS AO operations at the W.M. Keck Observatory”. In: *Observatory Operations: Strategies, Processes, and Systems*. Ed. by David R. Silva and Rodger E. Doxsey. Vol. 6270. Society of Photo-Optical Instrumentation Engineers (SPIE) Conference Series, 62700C, p. 62700C. DOI: 10.1117/12.671837.

Lide, DR and HPR Frederikse (1996). *CRC handbook of chemistry and physics, 1995-1996 : A ready-reference book of chemical and physical data*. Boca Raton, Fl: CRC Press.

Linnik, V. P. (Oct. 1957). “On the Possibility of Reducing the Influence of Atmospheric Seeing on the Image Quality of Stars”. In: *Optika i Spektroskopiya* 3 (4), pp. 401–402.

Liu, Z. and J. M. Beckers (Jan. 2001). “Comparative Solar Seeing and Scintillation Studies at the Fuxian Lake Solar Station”. In: *Solar Phys.* 198.1, pp. 197–209. DOI: 10.1023/A:1005262911134.

Löfdahl, M. G. (Dec. 2010). “Evaluation of image-shift measurement algorithms for solar Shack-Hartmann wavefront sensors”. In: *A&A* 524, A90, A90. DOI: 10.1051/0004-6361/201015331. arXiv: 1009.3401 [astro-ph.IM].

Löfdahl, M. G., M. J. van Noort, and C. Denker (Jan. 2007). “Solar image restoration”. In: *Modern solar facilities - advanced solar science*. Ed. by Franz Kneer, Klaus G. Puschmann, and Axel D. Wittmann, p. 119.

Lutomirski, R. F., W. L. Woodie, and R. G. Buser (Mar. 1977). “Turbulence-degraded beam quality: Improvement obtained with a tilt-correcting aperture”. In: *Applied Optics* 16.3, pp. 665–673. DOI: 10.1364/AO.16.000665.

Macintosh, B., J. Graham, et al. (June 2006). “The Gemini Planet Imager”. In: *Advances in Adaptive Optics II*. Ed. by Brent L. Ellerbroek and Domenico Bonaccini Calia. Vol. 6272. Society of Photo-Optical Instrumentation Engineers (SPIE) Conference Series, 62720L, p. 62720L. DOI: 10.1117/12.672430.

Macintosh, B., M. Troy, et al. (June 2006). “Extreme adaptive optics for the Thirty Meter Telescope”. In: *Advances in Adaptive Optics II*. Ed. by Brent L. Ellerbroek and Domenico Bonaccini Calia. Vol. 6272. Society of Photo-Optical Instrumentation Engineers (SPIE) Conference Series, 62720N, 62720N. DOI: 10.1117/12.672032.

Madec, P. -Y. et al. (July 2018). “Adaptive Optics Facility: from an amazing present to a brilliant future...” In: *Adaptive Optics Systems VI*. Ed. by Laird M. Close, Laura Schreiber, and Dirk Schmidt. Vol. 10703. Society of Photo-Optical Instrumentation Engineers (SPIE) Conference Series, 1070302, p. 1070302. DOI: 10.1117/12.2312428.

Marchetti, E., R. Brast, B. Delabre, R. Donaldson, E. Fedrigo, C. Frank, N. Hubin, J. Kolb, J-L. Lizon, M. Marchesi, S. Oberti, R. Reiss, J. Santos, et al. (Sept. 2007). “On-sky Testing of the Multi-Conjugate Adaptive Optics Demonstrator”. In: *The Messenger* 129, pp. 8–13.

Marchetti, E., R. Brast, B. Delabre, R. Donaldson, E. Fedrigo, C. Frank, N. Hubin, J. Kolb, J-L. Lizon, M. Marchesi, S. Oberti, R. Reiss, C. Soenke, et al. (July 2008). “MAD on sky results in star oriented mode”. In: *Adaptive Optics Systems*. Ed. by Norbert Hubin, Claire E. Max, and Peter L. Wizinowich. Vol. 7015. Society of Photo-Optical Instrumentation Engineers (SPIE) Conference Series, 70150F, 70150F. DOI: 10.1117/12.787240.

Marino, J., E. Carlisle, and D. Schmidt (July 2016). “Simulation of DKIST solar adaptive optics system”. In: *Adaptive Optics Systems V*. Ed. by Enrico Marchetti, Laird M. Close, and Jean-Pierre Véran. Vol. 9909. Society of Photo-Optical Instrumentation Engineers (SPIE) Conference Series, 99097C, p. 99097C. DOI: 10.1117/12.2232060.

Marino, J. and T. Rimmele (Nov. 2010). “Estimation and application of the solar adaptive optics corrected long-exposure point spread function”. In: *Applied Optics* 49.31, G95. DOI: 10.1364/AO.49.000G95.

Marois, C. et al. (Dec. 2010). “Images of a fourth planet orbiting HR 8799”. In: *Nature* 468.7327, pp. 1080–1083. DOI: 10.1038/nature09684. arXiv: 1011.4918 [astro-ph.EP].

Martinez, P. et al. (Sept. 2010). “On the Difference between Seeing and Image Quality: When the Turbulence Outer Scale Enters the Game”. In: *The Messenger* 141, pp. 5–8.

Mathur, Harsh et al. (Jan. 2023). “An Image Auto Guider System for Kodaikanal Tower Tunnel Telescope”. In: *Journal of Astronomical Instrumentation* 12.2, 2350003-222, pp. 2350003–222. DOI: 10.1142/S2251171723500034.

Mayer, J. R. (1863). “XXXIV. On celestial dynamics”. In: *The London, Edinburgh, and Dublin Philosophical Magazine and Journal of Science* 25.168, pp. 241–248. DOI:

10.1080/14786446308643453. eprint: https://doi.org/10.1080/14786446308643453. URL: https://doi.org/10.1080/14786446308643453.

McHugh, J. P., G. Y. Jumper, and M. Chun (Dec. 2008). “Balloon Thermosonde Measurements over Mauna Kea and Comparison with Seeing Measurements”. In: *PASP* 120.874, p. 1318. DOI: 10.1086/595871.

Merkle, F. et al. (Dec. 1989). “Successful tests of adaptive optics.” In: *The Messenger* 58, pp. 1–4.

Miura, N. et al. (July 2008). “Solar adaptive optics system at the Hida Observatory”. In: *Adaptive Optics Systems*. Ed. by Norbert Hubin, Claire E. Max, and Peter L. Wizinowich. Vol. 7015. Society of Photo-Optical Instrumentation Engineers (SPIE) Conference Series, 70156U, 70156U. DOI: 10.1117/12.788308.

Montilla, I. et al. (July 2016). “Solar adaptive optics: specificities, lessons learned, and open alternatives”. In: *Adaptive Optics Systems V*. Ed. by Enrico Marchetti, Laird M. Close, and Jean-Pierre Véran. Vol. 9909. Society of Photo-Optical Instrumentation Engineers (SPIE) Conference Series, 99091H, 99091H. DOI: 10.1117/12.2233652.

Moretto, G. et al. (Oct. 2004). “Optical set-up and design for solar multiconjugate adaptive optics at Dunn Solar Telescope/NSO”. In: *Advancements in Adaptive Optics*. Ed. by Domenico Bonaccini Calia, Brent L. Ellerbroek, and Roberto Ragazzoni. Vol. 5490. Society of Photo-Optical Instrumentation Engineers (SPIE) Conference Series, pp. 905–912. DOI: 10.1117/12.548894.

Morzinski, K. M. et al. (July 2014). “MagAO: Status and on-sky performance of the Magellan adaptive optics system”. In: *Adaptive Optics Systems IV*. Ed. by Enrico Marchetti, Laird M. Close, and Jean-Pierre Vran. Vol. 9148. Society of Photo-Optical Instrumentation Engineers (SPIE) Conference Series, 914804, p. 914804. DOI: 10.1117/12.2057048. arXiv: 1407.5098 [astro-ph.IM].

Nakahata, M. (Dec. 2022). “History of solar neutrino observations”. In: *Progress of Theoretical and Experimental Physics* 2022.12, 12B103, 12B103. DOI: 10.1093/ptep/ptac039. arXiv: 2202.12421 [hep-ex].

Nakajima, T. (Apr. 1994). “Planet Detectability by an Adaptive Optics Stellar Coronagraph”. In: *Astrophysical Journal* 425, p. 348. DOI: 10.1086/173990.

Nayak, A. et al. (Feb. 2013). “High-Altitude Ballooning Program at the Indian Institute of Astrophysics”. In: *arXiv e-prints*, arXiv:1302.0981, arXiv:1302.0981. DOI: 10.48550/arXiv.1302.0981. arXiv: 1302.0981 [astro-ph.IM].

Needham, J. (1959). *Science and Civilisation in China, Volume 3: Mathematics and the Sciences of the Heavens and the Earth*. Science and Civilisation in China volume 3. Cambridge University Press.

Neichel, B. and F. Rigaut (Feb. 2012). “First light for the Gemini Multi-Conjugate Adaptive Optics System”. In: *SPIE Newsroom*. DOI: 10.1117/2.1201201.004101.

Neichel, B., F. Rigaut, et al. (Jan. 2013). “First On-sky Results with GeMS, the Gemini Multi-conjugate AO System”. In: *American Astronomical Society Meeting Abstracts #221*. Vol. 221. American Astronomical Society Meeting Abstracts, 439.06, p. 439.06.

Newton, R. R. (May 1974). “Two Uses of Ancient Astronomy”. In: *Philosophical Transactions of the Royal Society of London Series A* 276.1257, pp. 99–116. DOI: `10.1098/rsta.1974.0012`.

Nijenhuis, J., W. Jonker, and F. Kamphues (Sept. 2022). “Development of a laser projection system for the ELT”. In: *Advances in Optical and Mechanical Technologies for Telescopes and Instrumentation*. Vol. 12188. Society of Photo-Optical Instrumentation Engineers (SPIE) Conference Series, 1218837, p. 1218837. DOI: `10.1117/12.2630101`.

Noll, R. J. (Mar. 1976). “Zernike polynomials and atmospheric turbulence.” In: *Journal of the Optical Society of America (1917-1983)* 66, pp. 207–211.

Olivier, S. S. and C. E. Max (1994). “Laser Guide Star Adaptive Optics: Present and Future”. In: *Symposium - International Astronomical Union* 158, pp. 283–292. DOI: `10.1017/S0074180900107739`.

Olivier, S. S., C. E. Max, et al. (Apr. 1993). “Tip-Tilt Compensation: Resolution Limits for Ground-based Telescopes Using Laser Guide Star Adaptive Optics”. In: *Astrophysical Journal* 407, p. 428. DOI: `10.1086/172525`.

Orban de Xivry, G. et al. (Oct. 2015). “First Results of the Ground Layer Adaptive Optics System ARGOS”. In: *Adaptive Optics for Extremely Large Telescopes IV (AO4ELT4)*, E72.

Padinhatteeri, S., R. Sridharan, and K. Sankarasubramanian (Sept. 2010). “Seeing-Induced Errors in Solar Doppler Velocity Measurements”. In: *Solar Physics* 266.1, pp. 195–207. DOI: `10.1007/s11207-010-9597-1`. arXiv: `1009.2966 [astro-ph.SR]`.

Parenti, R. R. and R. J. Sasiela (Jan. 1994). “Laser guide-star systems for astronomical applications.” In: *Journal of the Optical Society of America A* 11.1, pp. 288–309. DOI: `10.1364/JOSAA.11.000288`.

Parenti, S. (Mar. 2014). “Solar Prominences: Observations”. In: *Living Reviews in Solar Physics* 11.1, 1, p. 1. DOI: `10.12942/lrsp-2014-1`.

Perrin, J. (Jan. 1919). “Matière et lumière”. In: *Annales de Physique* 9.11, pp. 5–108. DOI: `10.1051/anphys/191909110005`.

Popowicz, A. et al. (Dec. 2017). “Review of Image Quality Measures for Solar Imaging”. In: *Solar Physics* 292.12, 187, p. 187. DOI: `10.1007/s11207-017-1211-3`. arXiv: `1709.09458 [astro-ph.IM]`.

Quintero Noda, C. et al. (Oct. 2022). “The European Solar Telescope”. In: *Astronomy and astrophysics* 666, A21, A21. DOI: `10.1051/0004-6361/202243867`. arXiv: `2207.10905 [astro-ph.SR]`.

Ragazzoni, R., Y. Almomany, et al. (July 2008). "Layer oriented: science with MAD and beyond". In: *Adaptive Optics Systems*. Ed. by Norbert Hubin, Claire E. Max, and Peter L. Wizinowich. Vol. 7015. Society of Photo-Optical Instrumentation Engineers (SPIE) Conference Series, 70150I, p. 70150I. DOI: `10.1117/12.790412`.

Ragazzoni, R., E. Marchetti, and G. Valente (Jan. 2000). "Adaptive-optics corrections available for the whole sky". In: *Nature* 403.6765, pp. 54–56. DOI: `10.1038/47425`.

Ran, X., L. Zhang, and C. Rao (Mar. 2024). "AC-SLODAR: measuring daytime normalized optical turbulence intensity distribution based on slope autocorrelation". In: *MNRAS* 528.3, pp. 3981–3991. DOI: `10.1093/mnras/stae202`.

Rao, C-H. et al. (Feb. 2016). "First generation solar adaptive optics system for 1-m New Vacuum Solar Telescope at Fuxian Solar Observatory". In: *Research in Astronomy and Astrophysics* 16.2, 23, p. 23. DOI: `10.1088/1674-4527/16/2/023`.

Rao, C. et al. (Dec. 2016). "Instrument Description and Performance Evaluation of a High-Order Adaptive Optics System for the 1 m New Vacuum Solar Telescope at Fuxian Solar Observatory". In: *The Astrophysical Journal* 833.2, 210, p. 210. DOI: `10.3847/1538-4357/833/2/210`.

Ravindra, B. et al. (Oct. 2018). "Installation of solar chromospheric telescope at the Indian Astronomical Observatory, Merak". In: *Journal of Astrophysics and Astronomy* 39.5, 60, p. 60. DOI: `10.1007/s12036-018-9554-1`.

Ren, D. et al. (Sept. 2015). "Multiple-Aperture-Based Solar Seeing Profiler". In: *PASP* 127.955, p. 870. DOI: `10.1086/682746`.

Rengaswamy, S. (2001). "Techniques for achieving higher spatial resolution". PhD thesis. Indian Institute of Astrophysics.

— (2016). "Image Quality Monitoring Experiments at Kodaikanal Tunel Telescope". In: *IIA Annual Report 30*.

Rengaswamy, S., R. K. Banyal, et al. (2020). "Astronomical Adaptive Optics at the Indian Institute of Astrophysics". In: *Progress in Optomechatronics*. Ed. by Indrani Bhattacharya et al. Singapore: Springer Singapore, pp. 1–11. ISBN: 978-981-15-6467-3.

Rengaswamy, S. and A. R. Bayanna (Feb. 2004). "Low-order adaptive optics for the meter aperture solar telescope of Udaipur Solar Observatory". In: *Telescopes and Instrumentation for Solar Astrophysics*. Ed. by Silvano Fineschi and Mark A. Gummin. Vol. 5171. Society of Photo-Optical Instrumentation Engineers (SPIE) Conference Series, pp. 219–230. DOI: `10.1117/12.509230`.

Rengaswamy, S., B. Ravindra, and K. Prabhu (Jan. 2019). "Measurement of Astronomical Seeing Using Long Exposure Solar Images". In: *Solar Physics* 294.1, 5, p. 5. DOI: `10.1007/s11207-019-1393-y`.

Restaino, S. R. (Dec. 1992). "Wave-front sensing and image deconvolution of solar data". In: *Applied optics* 31.35, pp. 7442–7449. DOI: `10.1364/AO.31.007442`.

Rigaut, F. (Jan. 2002). "Ground Conjugate Wide Field Adaptive Optics for the ELTs". In: *European Southern Observatory Conference and Workshop Proceedings*. Ed. by E. Vernet et al. Vol. 58. European Southern Observatory Conference and Workshop Proceedings, p. 11.

Rigaut, F. and B. Neichel (Sept. 2018). "Multiconjugate Adaptive Optics for Astronomy". In: *Annual Review of Astronomy and Astrophysics* 56, pp. 277–314. DOI: `10.1146/annurev-astro-091916-055320`.

Rimmele, T., S. Hegwer, et al. (Jan. 2010). "Solar Multi-Conjugate Adaptive Optics at the Dunn Solar Telescope". In: *Adaptative Optics for Extremely Large Telescopes*, 08002, p. 08002. DOI: `10.1051/ao4elt/201008002`.

Rimmele, T., K. Richards, et al. (June 2006). "Progress with solar multi-conjugate adaptive optics at NSO". In: *Advances in Adaptive Optics II*. Ed. by Brent L. Ellerbroek and Domenico Bonaccini Calia. Vol. 6272. Society of Photo-Optical Instrumentation Engineers (SPIE) Conference Series, 627206, p. 627206. DOI: `10.1117/12.671603`.

Rimmele, T. R. (July 2000). "Solar adaptive optics". In: *Adaptive Optical Systems Technology*. Ed. by Peter L. Wizinowich. Vol. 4007. Society of Photo-Optical Instrumentation Engineers (SPIE) Conference Series, pp. 218–231. DOI: `10.1117/12.390301`.

— (Oct. 2004). "Recent advances in solar adaptive optics". In: *Advancements in Adaptive Optics*. Ed. by Domenico Bonaccini Calia, Brent L. Ellerbroek, and Roberto Ragazzoni. Vol. 5490. Society of Photo-Optical Instrumentation Engineers (SPIE) Conference Series, pp. 34–46. DOI: `10.1117/12.551764`.

Rimmele, T. R. and R. R. Radick (1996). "Experimental Comparison of Two Approaches for Solar Wavefront Sensing". In: *Adaptive Optics*. Optica Publishing Group, AThC.6. DOI: `10.1364/ADOP.1996.AThC.6`. URL: `https://opg.optica.org/abstract.cfm?URI=ADOP-1996-AThC.6`.

— (Sept. 1998). "Solar adaptive optics at the National Solar Observatory". In: *Adaptive Optical System Technologies*. Ed. by Domenico Bonaccini and Robert K. Tyson. Vol. 3353. Society of Photo-Optical Instrumentation Engineers (SPIE) Conference Series, pp. 72–81. DOI: `10.1117/12.321734`.

Rimmele, T. R., M. Warner, et al. (Dec. 2020). "The Daniel K. Inouye Solar Telescope - Observatory Overview". In: *Solar Physics* 295.12, 172, p. 172. DOI: `10.1007/s11207-020-01736-7`.

Rimmele, T. R., F. Woeger, et al. (July 2010). "Solar multiconjugate adaptive optics at the Dunn Solar Telescope". In: *Adaptive Optics Systems II*. Ed. by Brent L. Ellerbroek et al. Vol. 7736. Society of Photo-Optical Instrumentation Engineers (SPIE) Conference Series, 773631, p. 773631. DOI: `10.1117/12.857485`.

Roadcap, J. R. and P. Tracy (Apr. 2009). "A preliminary comparison of daylit and night C_n^2 profiles measured by thermosonde". In: *Radio Science* 44.2, RS2011, RS2011. DOI: 10.1029/2008RS003921.

Roddier, F. (Jan. 1981). "The effects of atmospheric turbulence in optical astronomy". In: *Progess in Optics* 19, pp. 281–376. DOI: 10.1016/S0079-6638(08)70204-X.

Romer, A. (1964). *The Discovery of Radioactivity and Transmutation*. Vol. 2. Classics of Science Volume 2. Dover Publications.

Safonova, M. et al. (Jan. 2016). "An overview of high-altitude balloon experiments at the Indian Institute of Astrophysics." In: *Astronomical and Astrophysical Transactions* 29.3, pp. 397–426. DOI: 10.48550/arXiv.1506.01538. arXiv: 1506.01538 [astro-ph.IM].

Saito, Y. et al. (July 2010). "The performance of the laser guide star system for the Subaru Telescope". In: *Adaptive Optics Systems II*. Ed. by Brent L. Ellerbroek et al. Vol. 7736. Society of Photo-Optical Instrumentation Engineers (SPIE) Conference Series, 773653, p. 773653. DOI: 10.1117/12.856484.

Sankarasubramanian, K. and T. Rimmele (June 2008). "High resolution observations using adaptive optics: Achievements and future needs". In: *Journal of Astrophysics and Astronomy* 29.1-2, pp. 329–337. DOI: 10.1007/s12036-008-0043-9. arXiv: 0801.3125 [astro-ph].

Sarazin, M. and F. Roddier (Jan. 1990). "The ESO differential image motion monitor". In: *A&A* 227.1, pp. 294–300.

Scharmer, G. B., K. Bjelksjo, et al. (Feb. 2003). "The 1-meter Swedish solar telescope". In: *Innovative Telescopes and Instrumentation for Solar Astrophysics*. Ed. by Stephen L. Keil and Sergey V. Avakyan. Vol. 4853. Society of Photo-Optical Instrumentation Engineers (SPIE) Conference Series, pp. 341–350. DOI: 10.1117/12.460377.

Scharmer, G. B., P. M. Dettori, et al. (Feb. 2003). "Adaptive optics system for the new Swedish solar telescope". In: *Innovative Telescopes and Instrumentation for Solar Astrophysics*. Ed. by Stephen L. Keil and Sergey V. Avakyan. Vol. 4853. Society of Photo-Optical Instrumentation Engineers (SPIE) Conference Series, pp. 370–380. DOI: 10.1117/12.460387.

Scharmer, G. B., M. G. Löfdahl, G. Sliepen, et al. (June 2019). "Is the sky the limit?. Performance of the revamped Swedish 1-m Solar Telescope and its blue- and red-beam reimaging systems". In: *Astronomy and Astrophysics* 626, A55, A55. DOI: 10.1051/0004-6361/201935735. arXiv: 1905.05588 [astro-ph.IM].

Scharmer, G. B., M. G. Löfdahl, T. I. M. van Werkhoven, et al. (Oct. 2010). "High-order aberration compensation with multi-frame blind deconvolution and phase diversity image restoration techniques". In: *Astronomy and Astrophysics* 521, A68, A68. DOI: 10.1051/0004-6361/201014800. arXiv: 1007.1236 [astro-ph.IM].

Scharmer, G. B., M. Shand, et al. (July 2000). “Workstation-based solar/stellar adaptive optics system”. In: *Adaptive Optical Systems Technology*. Ed. by Peter L. Wizinowich. Vol. 4007. Society of Photo-Optical Instrumentation Engineers (SPIE) Conference Series, pp. 239–250. DOI: `10.1117/12.390291`.

Scharmer, G. B., G. Sliepen, et al. (May 2024). “The 85-electrode adaptive optics system of the Swedish 1-m Solar Telescope”. In: *Astronomy and Astrophysics* 685, A32, A32. DOI: `10.1051/0004-6361/201936005`. arXiv: `2311.13690 [astro-ph.IM]`.

Scharmer, G. B. and T. I. M. van Werkhoven (Apr. 2010). “S-DIMM+ height characterization of day-time seeing using solar granulation”. In: *A&A* 513, A25, A25. DOI: `10.1051/0004-6361/200913791`. arXiv: `1002.3151 [astro-ph.IM]`.

Schmidt, D., T. Berkefeld, and F. Heidecke (July 2012). “The 2012 status of the MCAO testbed for the GREGOR solar telescope”. In: *Adaptive Optics Systems III*. Ed. by Brent L. Ellerbroek, Enrico Marchetti, and Jean-Pierre Véran. Vol. 8447. Society of Photo-Optical Instrumentation Engineers (SPIE) Conference Series, 84473J, 84473J. DOI: `10.1117/12.926902`.

Schmidt, D., T. Berkefeld, F. Heidecke, et al. (July 2014). “GREGOR MCAO looking at the Sun”. In: *Adaptive Optics Systems IV*. Ed. by Enrico Marchetti, Laird M. Close, and Jean-Pierre Vran. Vol. 9148. Society of Photo-Optical Instrumentation Engineers (SPIE) Conference Series, 91481T, 91481T. DOI: `10.1117/12.2055154`.

Schmidt, D., N. Gorceix, and P. Goode (Dec. 2020). “On the sequence of deformable mirrors in MCAO: findings from an on-sky, closed-loop experiment”. In: *Adaptive Optics Systems VII*. Ed. by Laura Schreiber, Dirk Schmidt, and Elise Vernet. Vol. 11448. Society of Photo-Optical Instrumentation Engineers (SPIE) Conference Series, 1144842, p. 1144842. DOI: `10.1117/12.2563376`.

Schmidt, D., N. Gorceix, P. R. Goode, et al. (Jan. 2017). “Clear widens the field for observations of the Sun with multi-conjugate adaptive optics”. In: *Astronomy and Astrophysics* 597, L8, p. L8. DOI: `10.1051/0004-6361/201629970`.

Schmidt, D. and II von der Lühe O. (May 2007). “Optical wavefront differentiation: wavefront sensing for solar adaptive optics based on a LCD”. In: *Adaptive Optics for Laser Systems and Other Applications*. Ed. by Gilles Cheriaux, Chris J. Hooker, and Michal Stupka. Vol. 6584. Society of Photo-Optical Instrumentation Engineers (SPIE) Conference Series, 658408, p. 658408. DOI: `10.1117/12.722640`.

Seykora, E. J. (June 1993). “Solar Scintillation and the Monitoring of Solar Seeing”. In: *Solar Phys.* 145.2, pp. 389–397. DOI: `10.1007/BF00690664`.

Shumko, S. et al. (Aug. 2014). “AO-308: the high-order adaptive optics system at Big Bear Solar Observatory”. In: *Adaptive Optics Systems IV*. Ed. by Enrico Marchetti, Laird M. Close, and Jean-Pierre Vran. Vol. 9148. Society of Photo-Optical Instrumentation Engineers (SPIE) Conference Series, 914835, p. 914835. DOI: 10.1117/12.2056731.

Singh, J. (Mar. 2008). “Proposed national large solar telescope”. In: *Journal of Astrophysics and Astronomy* 29.1-2, pp. 345–351. DOI: 10.1007/s12036-008-0045-7.

Socas-Navarro, H. et al. (Nov. 2005). “Solar Site Survey for the Advanced Technology Solar Telescope. I. Analysis of the Seeing Data”. In: *PASP* 117.837, pp. 1296–1305. DOI: 10.1086/496939. arXiv: astro-ph/0508690 [astro-ph].

Sridharan, R., A. R. Bayanna, et al. (Sept. 2005). “An Image Stabilization System for Solar Observations”. In: *Bulletin of the Astronomical Society of India* 33, pp. 414–414.

Sridharan, R., Nirvikar Dashora, and P. Venkatakrishnan (July 2004). “Estimation of Fried’s Parameter from Long-Exposure Solar Images”. In: *Solar Physics* 222.1, pp. 35–41. DOI: 10.1023/B:SOLA.0000036874.76464.4e.

Starck, J. L., E. Pantin, and F. Murtagh (Oct. 2002). “Deconvolution in Astronomy: A Review”. In: *Publications of the Astronomical Society of the Pacific* 114.800, pp. 1051–1069. DOI: 10.1086/342606.

Stephenson, F. R. and D. M. Willis (Dec. 1999). “The earliest drawing of sunspots”. In: *Astronomy and Geophysics* 40.6, p. 21.

Stewart, G. W. (1993). “On the Early History of the Singular Value Decomposition”. In: *SIAM Review* 35. DOI: 10.1137/1035134.

Stix, M. (2002). *The Sun: An Introduction*. 2nd ed. Astronomy and Astrophysics Library. Springer-Verlag Berlin Heidelberg.

Subramanian, S. K. and S. Rengaswamy (May 2023a). “Forward modelling of turbulence strength profile estimation using S-DIMM+”. In: *Society of Photo-Optical Instrumentation Engineers (SPIE) Conference Series*. Ed. by Anita Mahadevan-Jansen, Asima Pradhan, and Sujatha Narayanan Unni. Vol. 12638. Society of Photo-Optical Instrumentation Engineers (SPIE) Conference Series, 1263812, p. 1263812. DOI: 10.1117/12.2671735.

— (June 2023b). “Measurement of isoplanatic angle and turbulence strength profile from H-alpha images of the Sun”. In: *Adaptive Optics for Extremely Large Telescopes (AO4ELT7)*, 22, p. 22. DOI: 10.13009/AO4ELT7-2023-023.

Subramanian, S. K., S. Rengaswamy, et al. (2024). “Daytime turbulence strength profile measurement at Kodaikanal Observatory”. In: *Journal of Astronomical Telescopes, Instruments, and Systems* 10.3, p. 039004. DOI: 10.1117/1.JATIS.10.3.039004. URL: https://doi.org/10.1117/1.JATIS.10.3.039004.

Summers, D. et al. (Feb. 2003). “Implementation of a laser traffic control system supporting laser guide star adaptive optics on Mauna Kea”. In: *Adaptive Optical System Technologies II*. Ed. by Peter L. Wizinowich and Domenico Bonaccini. Vol. 4839. Society of Photo-Optical Instrumentation Engineers (SPIE) Conference Series, pp. 440–451. DOI: 10.1117/12.459062.

Tallon, M. and R. Foy (Aug. 1990). "Adaptive telescope with laser probe: isoplanatism and cone effect." In: *Astronomy and Astrophysics* 235, pp. 549–557.

Tassoul, J-L. and M. Tassoul (2004). *A concise history of solar and stellar physics*. Princeton University Press.

Tatulli, E. and A. N. Ramaprakash (Dec. 2013). "Laser tomography adaptive optics: a performance study". In: *Journal of the Optical Society of America A* 30.12, p. 2482. DOI: 10.1364/JOSAA.30.002482. arXiv: 1310.7362 [astro-ph.IM].

Thomson, W. (1854). "LII. On the mechanical energies of the solar system". In: *The London, Edinburgh, and Dublin Philosophical Magazine and Journal of Science* 8.54, pp. 409–430. DOI: 10.1080/14786445408651955. eprint: https://doi.org/10.1080/14786445408651955. URL: https://doi.org/10.1080/14786445408651955.

Tokovinin, A. (Oct. 2002). "From Differential Image Motion to Seeing". In: *Publications of the Astronomical Society of the Pacific* 114.800, pp. 1156–1166. DOI: 10.1086/342683.

— (Oct. 2004). "Seeing Improvement with Ground-Layer Adaptive Optics". In: *Publications of the astronomical society of pacific* 116.824, pp. 941–951. DOI: 10.1086/424805.

Tokovinin, A., M. Le Louarn, and M. Sarazin (Oct. 2000). "Isoplanatism in a multiconjugate adaptive optics system". In: *Journal of the Optical Society of America A* 17.10, pp. 1819–1827. DOI: 10.1364/JOSAA.17.001819.

Tripathi, D. et al. (Jan. 2023). "The Aditya-L1 mission of ISRO". In: *The Era of Multi-Messenger Solar Physics*. Ed. by Gianna Cauzzi and Alexandra Tritschler. Vol. 372. IAU Symposium, pp. 17–27. DOI: 10.1017/S1743921323001230. arXiv: 2212.13046 [astro-ph.SR].

Trubey, M. et al. (Aug. 2022). "TMT Laser Guide Star Facility preliminary design". In: *Adaptive Optics Systems VIII*. Ed. by Laura Schreiber, Dirk Schmidt, and Elise Vernet. Vol. 12185. Society of Photo-Optical Instrumentation Engineers (SPIE) Conference Series, 121857H, 121857H. DOI: 10.1117/12.2630542.

Unni. C, V. et al. (Apr. 2021). "Seeing Measurements with the Merak Hα Telescope". In: *Solar Physics* 296.4, 65, p. 65. DOI: 10.1007/s11207-021-01807-3.

van Dam, M. A. et al. (June 2023). "Effect of deformable mirror sequence on performance of multiconjugate adaptive optics". In: *Adaptive Optics for Extremely Large Telescopes (AO4ELT7)*, 2, p. 2. DOI: 10.13009/AO4ELT7-2023-002.

van der Lühe, O. et al. (Feb. 2003). "KAOS: Adaptive optics system for the Vacuum Tower Telescope at Teide Observatory". In: *Innovative Telescopes and Instrumentation for Solar Astrophysics*. Ed. by Stephen L. Keil and Sergey V. Avakyan. Vol. 4853. Society of Photo-Optical Instrumentation Engineers (SPIE) Conference Series, pp. 187–193. DOI: 10.1117/12.498659.

van Iersel, M. et al. (Sept. 2019). “Measuring the turbulence profile in the lower atmospheric boundary layer”. In: *Applied Optics* 58.25, p. 6934. DOI: 10.1364/AO.58.006934.

Vaquero, J. M. and M. Vázquez (2009). *The Sun Recorded Through History: Scientific Data Extracted from Historical Documents*. Vol. 361. Springer.

Venkatakrishnan, P. et al. (Aug. 2017). “The Multi Application Solar Telescope”. In: *Current Science* 113.4, p. 686. DOI: 10.18520/cs/v113/i04/686-690.

Vogt, F. P. A. et al. (Apr. 2017). “Detection and Implications of Laser-Induced Raman Scattering at Astronomical Observatories”. In: *Physical Review X* 7.2, 021044, p. 021044. DOI: 10.1103/PhysRevX.7.021044. arXiv: 1706.07050 [astro-ph.IM].

von der Luhe, O. (Dec. 1988). “Wavefront error measurement technique using extended, incoherent light sources”. In: *Optical Engineering* 27, pp. 1078–1087. DOI: 10.1117/12.7978681.

von der Lühe, O. (May 1984). “Estimating Fried’s parameter from a time series of an arbitrary resolved object imaged through atmospheric turbulence.” In: *Journal of the Optical Society of America A* 1, pp. 510–519. DOI: 10.1364/JOSAA.1.000510.

von der Lühe, O., T. Berkefeld, and D. Soltau (Feb. 2002). “Adaptive optics system for a 1.5-m solar telescope”. In: *Optics in Atmospheric Propagation and Adaptive Systems IV*. Ed. by Anton Kohnle, John D. Gonglewski, and Thomas J. Schmugge. Vol. 4538. Society of Photo-Optical Instrumentation Engineers (SPIE) Conference Series, pp. 197–204. DOI: 10.1117/12.454408.

von Weizsacker, C. F. (1937). “Uber elementumwandlungen im innern der sterne”. In: *I (On*.

Waldmann, T. A., T. Berkefeld, and O. von der Lühe (2007). “Measuring Turbulence Height Profiles using Extended Sources and a Wide-Field Hartmann-Shack Wavefront-Sensor”. In: *Adaptive Optics: Analysis and Methods/Computational Optical Sensing and Imaging/Information Photonics/Signal Recovery and Synthesis Topical Meetings on CD-ROM*. Optica Publishing Group, PMA3. DOI: 10.1364/AOPT.2007.PMA3. URL: https://opg.optica.org/abstract.cfm?URI=AOPT-2007-PMA3.

Wang, C. P. (June 1975). “Isoplanicity for imaging through turbulent media”. In: *Optics Communications* 14.2, pp. 200–204. DOI: 10.1016/0030-4018(75)90213-8.

Wang, J. Y. (Mar. 1977). “Optical resolution through a turbulent medium with adaptive phase compensations*”. In: *Journal of the Optical Society of America (1917-1983)* 67.3, p. 383. DOI: 10.1364/JOSA.67.000383.

Wang, Z. et al. (July 2018). “A modified S-DIMM+: applying additional height grids for characterizing daytime seeing profiles”. In: *MNRAS* 478.2, pp. 1459–1467. DOI: `10.1093/mnras/sty1097`.

Waterston, J. J. (Mar. 1860). “On certain Inductions as to the Heat engendered by the possible Fall of a Meteor into the Sun, and on deducing the absolute Temperature of the Solar Surface from Thermometric Observation”. In: *Monthly Notices of the Royal Astronomical Society* 20, pp. 197–202. DOI: `10.1093/mnras/20.5.197`.

Weizsäcker, C. (June 2014). “On Elementary Transmutations in the Interior of Stars: Paper II (1937)”. In: Springer, Cham, pp. 7–29. ISBN: 978-3-319-03667-0. DOI: `10.1007/978-3-319-03668-7_2`.

Wilson, R. W. (Nov. 2002). “SLODAR: measuring optical turbulence altitude with a Shack-Hartmann wavefront sensor”. In: *MNRAS* 337.1, pp. 103–108. DOI: `10.1046/j.1365-8711.2002.05847.x`.

Winker, D. M. (Oct. 1991). “Effect of a finite outer scale on the Zernike decomposition of atmospheric optical turbulence.” In: *Journal of the Optical Society of America A* 8.10, pp. 1568–1573. DOI: `10.1364/JOSAA.8.001568`.

Wizinowich, P. et al. (June 2023). “Keck Adaptive Optics Current and Future Roles as an ELT Pathfinder”. In: *Adaptive Optics for Extremely Large Telescopes (AO4ELT7)*, 8, p. 8. DOI: `10.13009/AO4ELT7-2023-009`.

Wollaston, W. H. (Jan. 1802). “XII. A Method of Examining Refractive and Dispersive Powers, by Prismatic Reflection”. In: *Philosophical Transactions of the Royal Society of London Series I* 92, pp. 365–380. DOI: `10.1098/rstl.1802.0013`.

Wyant, J. C. (Nov. 1975). “Use of an ac heterodyne lateral shear interferometer with real-time wavefront correction systems”. In: *Applied Optics* 14, pp. 2622–2626. DOI: `10.1364/AO.14.002622`.

Yan, J. et al. (July 2022). “Daocheng solar radio telescope: system and first results”. In: *44th COSPAR Scientific Assembly. Held 16-24 July*. Vol. 44, p. 1886.

Zhang, L. et al. (July 2016). “Preliminary result of the solar multi-conjugate adaptive optics for 1m new vacuum solar telescope”. In: *Adaptive Optics Systems V*. Ed. by Enrico Marchetti, Laird M. Close, and Jean-Pierre Véran. Vol. 9909. Society of Photo-Optical Instrumentation Engineers (SPIE) Conference Series, 99092C, p. 99092C. DOI: `10.1117/12.2231955`.

Zirker, J. B. (1995). *Total eclipses of the sun*. Princeton University Press.